University of Alberta

Characterization of Diamond-like Carbon Films Produced by Pulsed Laser Deposition

by

Hideki Minami

A thesis submitted to the Faculty of Graduate Studies and Research in partial fulfillment of the requirements for the degree of Master of Science

Department of Electrical and Computer Engineering

Edmonton, Alberta

Fall, 1999

National Library of Canada
Acquisitions and Bibliographic Services
395 Wellington Street
Ottawa ON K1A 0N4
Canada

Bibliothèque nationale du Canada
Acquisitions et services bibliographiques
395, rue Wellington
Ottawa ON K1A 0N4
Canada

Your file Votre référence

Our file Notre référence

The author has granted a non-exclusive licence allowing the National Library of Canada to reproduce, loan, distribute or sell copies of this thesis in microform, paper or electronic formats.

L'auteur a accordé une licence non exclusive permettant à la Bibliothèque nationale du Canada de reproduire, prêter, distribuer ou vendre des copies de cette thèse sous la forme de microfiche/film, de reproduction sur papier ou sur format électronique.

The author retains ownership of the copyright in this thesis. Neither the thesis nor substantial extracts from it may be printed or otherwise reproduced without the author's permission.

L'auteur conserve la propriété du droit d'auteur qui protège cette thèse. Ni la thèse ni des extraits substantiels de celle-ci ne doivent être imprimés ou autrement reproduits sans son autorisation.

0-612-47071-7

Canada

University of Alberta

Library Release Form

Name of Author: Hideki MINAMI

Title of Thesis: Characterization of Diamond-like Carbon Films Produced by Pulsed Laser Deposition

Degree: Master of Science

Year this Degree Granted: 1999

Permission is hereby granted to the University of Alberta Library to reproduce single copies of this thesis and to lend or sell such copies for private, scholarly, or scientific research purposes only.

The author reserves all other publication and other rights in association with the copyright in the thesis, and except as hereinbefore provided, neither the thesis nor any substantial portion thereof may be printed or otherwise reproduced in any material from whatever without the author's prior written permission.

October 1, 1999

University of Alberta

Faculty of Graduate Studies and Research

The undersigned certify that they have read, and recommend to the Faculty of Graduate Studies and Research for acceptance, a thesis entitled Characterization of Diamond-like Films Produced by Pulsed Laser Deposition submitted by Hideki Minami in partial fulfillment of the requirements for the degree of Master of Science.

R. Fedosejevs

Y. Y. Tsui

R. W. Lawson

F. Hegmann

Abstract

A study was carried out to characterize thin diamond-like carbon films which are deposited from carbon plasma produced by a pulsed laser deposition facility with and without using a magnetic plasma guide field. The use of a curved magnetic guide field ensures a coating made with pure plasma ions and reduced debris content compared to traditional pulsed laser deposition. Measurements of thickness, density, refractive index, and fraction of sp^3 bonding were made using a variety of diagnostics including profilometery, microbalance measurements, spectrophotometery, ellipsometery, scanning electron microscopy and electron energy loss spectroscopy. A Laser Induced Surface Acoustic Wave (LISAW) diagnostic technique was also developed and its application to the characterization of the thin films was investigated. These data are compared with those of carbon films made by standard pulsed laser deposition which employs a mixture of ions, atoms, clusters and neutral particles in the coating process. It was found that films made with magnetic guiding were low in debris population and were slightly better in quality compared to those made without magnetic guiding under similar conditions.

Acknowledgment

I would first like to thank Robert Fedosejevs who gave me an opportunity to study and work for the past two and a half years. I have benefited significantly from his help without which I would never have been able to achieve this work. Also, I have been inspired by his attitude toward science.

I am very grateful to Y.Y. Tsui for supporting me throughout my research and course work with his advice and encouragement. I would like to express my gratefulness to Blair Harwood for his technical support and advice and Dammika Manage for helping me with her strong knowledge of diamond-like carbon.

It is my pleasure to express my thanks to Ray Egerton who gave me access to his electron energy loss spectroscopy facility and provided supplies necessary for the sample preparations, Marek Malac for his doing a significant amount of EELS measurements for me, and Mike Brett for his giving me access to his ellipsometer and spectrophotometers. I would like to thank the people in the machine shop for building excellent apparatus for my research work, and Ben Bathgate for giving me advice regarding amplifiers.

I also would like to express my thanks to Michael Buhr, Geoff Redman, Serguei Roupassov, and Mohammad Mohebbi for their friendship, having discussions with me and helping me with my course work.

Finally, I would like to thank Minako Kambayashi for her support, encouragement and patience, and my father and my mother for their support throughout my studies.

Hideki Minami

Edmonton, Alberta

Table of Contents

I Introduction 1

I.1 Bonding in carbon 1

I.2 Introduction to thin diamond-like carbon films 3

I.3 Principles of pulsed laser deposition of thin films 9

I.3.1 Introduction 9
I.3.2 Previous Results 10

I.4 Development of the Magnetic Guiding of Plasma 16

I.4.1 Motivation 16
I.4.2 Plasma guiding for debris reduction 18
I.4.3 Current Setup for Magnetic Guided Pulsed Laser Deposition Facility 21

II Important Properties of Thin Diamond-Like Film and Diagnostic Measurement Techniques 25

II.1 Mechanical Properties 25

II.1.1 Thickness and density 27
II.1.2 Hardness 33
II.1.3 Stress and Adhesion 34
II.1.4 Elasticity 40

II.2 Optical Properties 42

II.2.1 Index of Refraction 42
II.2.2 Optical Absorption Edge Energy 47

II.3 Electrical Properties 49

II.3.1 Resistivity 49

II.4 Chemical Bonding Structure 51

II.4.1 sp^3/sp^2 ratio 51

III Development of a SAW Detection System for Film Characterization 54

III.1 Introduction 54

III.1.1 Rayleigh wave 54
III.1.2 Dispersion 56
III.1.3 Pulsed Laser Excitation of SAW 62
III.1.4 Energy directionality of SAW generated from a line source 65

III.2 System Development 71

III.2.1 Knife-edge 75
III.2.2 Piezoelectric Film 78
III.2.3 Amplifier 78
III.3 Noise Reduction 80
III.4 Signal Detection 82
III.4.1 Effect of the Contact Pressure of PVDF Film. 82
III.4.2 Effect of Linewidth to the Signal amplitude. 85
III.4.3 Dispersion Effect 89
III.5 Data Analysis 91
III.6 Summary 99

IV Fabrication of DLC Films 101
IV.1 Substrate Preparation 101
IV.2 Setup 102
IV.3 Supportive experiments before coating run 106
IV.3.1 Faraday Cup Measurement 106
IV.3.2 Cariblation of quartz crystal monitor 111
IV.4 Films deposited 114

V Characterization of Diamond Like Films Produced 116
V.1 Thickness Measurement 118
V.2 Density Measurement 120
V.3 Measurement of Index of Refraction 122
V.3.1 Imaginary Part of Index of Refraction(Extinction Coefficient) 122
V.4 Real Part of Index of Refraction(Refractive Index) 131
V.5 Optical Gap Measurement 135
V.6 SAW Measurement 137
V.7 Measurement of sp^3/sp^2 Ratio 144

VI Results and Discussion 157
VI.1 Performance of broadband SAW transducer 160
VI.2 Film properties 157

VII Conclusion 163
VIII References 165

List of Tables

Table 1 Mechanical properties: Comparison of Young modulus, bulk modulus, shear modulus, Poisson ratio, hardness and yield stress [42] 26

Table 2 The results of the laser intensity measurements by using a CCD camera. For calculations, the laser pulse was assumed to have a energy of 100mJ and the time duration of 15ns (FWHM). 110

Table 3 samples fabricated with PLD with various conditions. 115

Table 4 Measured properties and characterization methods 116

Table 5 Measurement techniques applied for each sample. 117

Table 6 Results of density measurements. 121

Table 7 Summary of the optical properties of the carbon film produced on Si(100) substrate by B-field plasma guiding PLD method (sample #23) measured at the different points on the sample as shown in Fig. 68. 134

Table 8 The result of the stress measurements taken for the films produced by normal PLD with different laser intensities. 137

Table 9 Fraction of sp^3 for the samples deposited with different deposition conditions estimated from the plasmon peak position and K-edge absorption peak. 156

Table 10. Summary of the properties for each sample 159

List of Figures

Fig. 1 Schematic representation of sp^3, sp^2 and sp^1 hybridized carbon. π-bonds are shaded and σ-bonds are unshaded [1]. 2

Fig. 2 Ratio of sp^3 to sp^2 hybrid bonds in diamond-like carbon (DLC) made using CVD deposition as a function of hydrogen content [7]. 4

Fig. 3 One type of Chemical Vapor Deposition uses a hot filament. Gases containing carbon and hydrogen are fed into a vacuum chamber and activated via a hot filament. The substrate is heated to a temperature between 700 and 1000°C. Through chemical reactions, both diamond and graphite are deposited on the substrate, but the graphite is etched away by hydrogen [8]. 5

Fig. 4 Single beam sputtering is one method of Physical Vapor Deposition. An ion gun is directed toward a carbon target and carbon atoms are removed and deposited on the substrate [8]. 6

Fig. 5 Schematic diagram of pulsed laser deposition process [9]. 7

Fig. 6 Scratch Hardness (a), and (b) plasma electron temperature as a function of laser pulse energy. Data points shown in (b) are estimates of T_e from X-UV spectra: dashed curve shows dependence anticipated from theory [30]. 13

Fig. 7 Schematic diagrams of laser deposition facilities which involve some supportive techniques to improve the film quality and the growth rate. Substrate heating and ion bonbartment on the substrate are employed [22]. 14

Fig. 8 Schematic diagrams of pulsed laser deposition facilities which involve some supportive techniques to improve the film quality and the growth rate. (a) employs electric discharge and ion acceleration [10]and (b) employs the injection of capacitively stored energy into the ablated plasma plume [24]. 15

Fig. 9 Razor blade scratch test of PLD diamond like carbon film [36]. 17

Fig. 10 Debris Reduction with Long Tube Geometry. Population density of the macro particle whose diameter is more than 1 μm was reduced significantly with 40cm plasma guiding with 3 coils geometry [36]. 20

Fig. 11 Schematic diagram of magnetic plasma guide developed at the University of Alberta. Ionized species are guided by magnetic field generated by the solenoid coil. 23

Fig. 12 Apparatus for Mass Selected Ion Beam deposition by magnetic filter, using a cathode arc source, after McKenzie et al [41]. 24

Fig. 13 Schematic diagram of a stylus instrument and an example of the measurement. A 40nm thick copper film on a silicon substrate is profiled. The grid space represents 500μm per division on the horizontal scale and 40nm per division on the vertical scale. 28

Fig. 14 Plasmon peaks of different forms of carbon measured by EELS [44]. 32

Fig. 15 Schematic diagram of stylus indentation. 33

Fig. 16 Apparatus for observing fringes produced by the variable air gap between a stressed circular and an optical flat [47]. 35

Fig. 17 Method of measuring stress by bending techniques. The displacement is measured by optical means in this case [47] 38

Fig. 18 Plot of the internal stresses of the amorphic diamond films prepared with deliberate alteration of laser intensity. Data are shown for films produced by laser beams having the indicated relative intensities. Nominal amorphic diamond films with 75% sp^3 fraction used in these experiments are produced with the relative laser intensity indicated by I_n which on the order of $10^{12}W/cm^2$ [54]. 38

Fig. 19 Cross section of the amorphic diamond film on a $TiAl_6V_4$ substrate, thinned and then imaged by TEM. An interfacial layer of microcrystals of TiC is evident from the bright points due to the diffractions of electron beam [55]. 39

Fig. 20 Schematic diagram of SAW measurement apparatus [56] 41

Fig. 21 Plot of electrical resistivities, mass densities, and relative laser intensities needed to produce amorphic diamond films with the values of n_i, the imaginary part of the complex index of refraction measured at 6328 Å as shown. Values of ordinates plotted for different properties at the same values of n_i do not necessarily correspond to measurements made on the same physical sample [61]. 43

Fig. 22 Schematic of V-shape ellipsometer. 45

Fig. 23 Selected spectra in the index of refraction n and extinction coefficient k, deduced from spectroscopic ellipsometry measurements of a-C prepared using a filtered beam of C^+ ions from a cathodic arc at substrate biases of -120, -300 and -500V, which lead to sp3 contents of 76, 50 and 20 at. % as determined by EELS [60] 46

Fig. 24 Key properties (atomic fraction of hydrogen(shown as X_H), density, optical gap, and hardness) of a-C:H deposited by rf plasma CVD as functions of rms self-bias voltage, Vb. Films deposited from three hydrocarbon precursors are compared [61] 48

Fig. 25 Schematic of in-line four-point probe. A constant current flow through the film from points 1 to 4 and the voltage across points 2 and 3 is measured [46]. 50

Fig. 26 An example of the Raman spectra of carbon materials made using different techniques. The G peak ($1580cm^{-1}$) and the D peak ($1350cm^{-1}$) are the signatures of the sp^2 and the sp^3, respectively [1]. (Note: the D peak in fact has the different wavenumber from that of the pure diamond peak ($1332cm^{-1}$), but it still can be used as the signature of the sp^3.) 52

Fig. 27 An example of the EELS spectra of carbon materials. From the π peak one can observe how much sp^2 bonding there is in the sample [64,65] 53

Fig. 28 Schematic of the relation between wavelength and penetration depth. When a film is present on a substrate, higher frequencies (i.e. shorter wavelengths) are more likely to be affected by the elastic properties of the film than lower frequencies which penetrate well into the substrate. 57

Fig. 29 Phase velocity of the first three Rayleigh modes; ZnO layer on silicon assuming isotropic parameters [66]. v_T is transverse wave velocity in the substrate material, v_R is the Rayleigh wave velocity in the substrate material, V_T is transverse wave velocity in the layer material and V_R is the Rayleigh wave velocity in the layer material. 60

Fig. 30 Phase and group velocity of a silicon layer on a ZnO substrate with respect to the product of the film thickness h and wavenumber.k, assuming isotropic parameters and layer shear velocity is larger than that of the substrate [66] 61

Fig. 31 Surface wave intensity as a function of laser-spot diameter. There is a pronounced maximum which occurs when $a=V_R\tau$ [here $V_R=2.0*10^3$ m/s, τ=25ns, 2a=0.16mm(+/-10%)]. The insert shows schematically that each radial component contributes to the measured signal Note that there is also a temperature gradient normal to the surface contributing to SAW generation because this type of wave contains longitudinal as well as transverse components [69]..... 64

Fig. 32 Received SAW signals for two different laser-spot diameters: (a) There is a well-defined pulse shape if $a=V_R\tau$ is satisfied: (b) For all other diameters the pulse form becomes increasingly modulated [69]. 64

Fig. 33 Construction used in applying Huygens' principle. 66

Fig. 34 An aperture distribution and its angular spectrum. 69

Fig. 35 Angular distribution of the amplitude of surface acoustic waves with different frequencies generated from a 4mm line source on an aluminum sample. The line radiator is oriented along the vertical direction. 69

Fig. 36 Displacement waveforms produced by the thermoelastic line source in various directions. Last three signals are expanded vertically by a factor of 2 [71]. 70

Fig. 37 Schematic diagram of the newly developed SAW detection system. 73

Fig. 38 A piezoelectric film wrapped around the knife-edge detects the SAW induced by the laser heating/ablation process. The laser line focus is parallel to the knife-edge..... 74

Fig. 39 Picture of the Laser Induced SAW detection system. 74

Fig. 40 Picture of broadband SAW transducer. A slot is made in order to allow the laser pulse to approach close to the knife-edge..... 76

Fig. 41 Schematic of the SAW transducer proposed by Coufal.et al [72]. 77

Fig. 42. Image of the top of the knife-edge. 77

Fig. 43 Noise reduction by the installation of the fast grounding metal strip to the aluminum housing of the broadband SAW transducer. Each SAW signal is the average of 256 waveforms measured on BK7. 81

Fig. 44 Correlation between the waveform and contact pressure. Pictures are sorted in order of increasing contact pressure. The pressure was adjusted by the vertical position of the knife edge mount that is adjusted by 40 turns per inch screw. It was not possible to deduce the exact pressure applied on the PZT film, but it is expected to lie in the μN range. It can be seen that the waveform is distorted from its bipolar shape as the knife-edge is pressed harder. Once the film makes good contact with the sample, the peak amplitude of the signal quickly saturates. 83

Fig. 45 Correlation between spectrum of the signals and contact pressure. Growth of a subpeak possibly due to the ringing noise is observed at about 125MHz. Inset numbers corresponding to those in Fig. 44..... 84

Fig. 46 Relation between vertical translation of the cylindrical lens and peak to peak voltage of the SAW signals (after 50db of amplification)..... 87

Fig. 47 Relation between peak-to-peak amplitude of SAW and linewidth deduced from the measurement shown in Fig. 46. 88

Fig. 48 SAW signals detected on Au film deposited on an Al substrate. As the propagation distance increases, the pulse broadens due to dispersion effects. 90

Fig. 49 Frequency spectrum of the SAW detected at x=xo+2.54mm on gold film on aluminum. 93

*Fig. 50 phase information with +/-2nπ ambiguity for the SAW's detected at X=Xo+2.54mm (plotted with .) and at X=X_o+5.08mm (plotted with *) from a gold film on an aluminum substrate.* 94

Fig. 51 Unwrapped phase information. 95

Fig. 52 Phase velocity dispersion of SAW on a 1000nm thick gold film deposited on an aluminum substrate. 96

Fig. 53 Predicted waveform calculated based on the theoretical dispersion curve for a 1000nm thick gold film on an aluminum substrate. The initial signal for the calculation is the measured signal at X_o. The relative peak positions of the predicted waveforms agree reasonably with those of actual waveforms shown in Fig. 48. 97

Fig. 54 Dispersion calculated for DLC with a single parameter value varied for each plot. The non varying parameters are set to their nominal values listed in the bottom of the figures. The substrate is Si(100) and propagation direction is{100}. 98

Fig. 55 Schematic diagram of the vacuum system used for pulsed laser deposition 104

Fig. 56 Setup for Pulsed Laser Deposition. 105

Fig. 57 An example of the Faraday cup measurement for the YAG laser irradiation onto the graphite tape target. The distance between the detection head of the Faraday cup and the target is 165mm. 108

Fig. 58 Distribution of the signals obtained by Faraday cup measurement at different horizontal positions at the exit of the solenoid coil. R indicates the distance from the center of the solenoid coil and the polarity is taken towards the outer radius of the curved solenoid coil. (Please refer Fig. 11 for the schematic of the setup.) KrF laser with a pulse energy of approximately 120mJ is in-focussed onto the graphite tape target with a 50cm focal lens. The target was at the best focus position and the laser intensity used was 10GW/cm^2. 109

Fig. 59 QCM reading with respect to the lens position. The QCM1 and QCM2 are located at 0 and 40 degrees with respect to the target. 112

Fig. 60 The angular dependence of the deposition rate with respect to the different lens positions. Measurements are taken for KrF and Nd:YAG laser. The distance between the target and the quartz crystal monitor is approximately 7cm and the average pulse energy is about 120mJ and 1000mJ for KrF laser and Nd:YAG laser respectively. The reduction in the deposition rate was observed when the lens position is adjusted to the in-focus position. 113

Fig. 61 Profilometer measurement of a 70nm thick DLC film (sample # 4-(c)). The grid spaces represent 100mm per division on the horizontal scale and 40nm per division on the vertical scale. 119

Fig. 62 Comparison between measured and calculated external transmittance of the UV grade quartz with the thickness of 3/4 inch. The jump in the measured values at 800nm is due to the detector change, and those at 340 and 680nm are due to lamp changes. The spectrum above 800nm was shifted to match that below 800nm to correct for a residual nonlinearity in the infrared detector. 125

Fig. 63 External transmittance of the carbon films deposited with different laser intensities. The film thicknesses for smple #4, 21, and 22 are 70±5nm, 28±10nm, and 28±10nm. A 3/4 inch thick S1UV substrate was used for sample #4 whereas 1mm thick S1UV substrate for samples #21and #22. 126

Fig. 64 Reflectance of the DLC film deposited on the quartz substrate. The amplitude modulation between 200nm and 400 nm is suspected to be due to instrumental error and not due to the Fabry Perot effect since modulation peaks are observed at same wavelength from 70±5nm thick film (Sample #4) and 28±10nm thick film (sample #21 & #22). One can find similar modulation in Fig. 62. The low transmission from sample #4 in the visible range may be due to the attenuation caused by a greater thickness of the sample compared with the others. 127

Fig. 65 Internal transmittance of DLC films. 128

Fig. 66 Calculated absorption coefficient of the DLC films produced with different laser intensities. 129

Fig. 67 Calculated extinction coefficient, n_i, of the film. Values of 0.10±0.1, 0.42±0.1, and 0.3±0.1 were found at the He-Ne wavelength (632.8nm) for the sample #4, 21, and 22, respectively. 130

Fig. 68 Carbon film fabricated on silicon (100) substrate (sample #23) by magnetic guiding with a curved 46±1cm long coil geometry. The sample was illuminated by a diffused white light source in order to show the color shift of the film due to the variation of the film thickness. The length of the black line in the picture is approximately equivalent to 19mm, which is the inner radius of the guiding tube. The center of the tube was located at the lower end of the black line. About 3mm of the left end of the substrate was covered with a mask during the coating run. The substrate was placed about 20±5mm away from the exit of the solenoid. Ellipsometer measurements are taken at three points where indicated with black dots. The distances of the dots from the edge of the sample are 2±0.5mm, 8±0.5mm and 15±0.5mm, respectively. 133

Fig. 69 Tauc plot for the DLC films deposited with the different laser energy flux of 4GW/cm^2 (sample #4-(c) and 22-(e)) and 10GW/cm^2 (sample # 21-(e)). An increase in the optical gap was observed for the lower laser intensity. The accuracy of the optical gap shown in the figure is ±0.2eV. 136

Fig. 70 SAW signals detected on a 70±5nm thick DLC film on a (001) silicon substrate. The approximate distance from the line source to detector for signal (a) was 3±0.5mm. The signal at (b) was detected at a distance of 762±10μm further than that of signal (a). A part of the laser beam was clipped by the metal housing of the SAW transducer when the near field signal was detected, resulted in the smaller peak amplitude compared with that of far field. For the near field signal 32 shots were averaged while for the far field signal 16 shots were averaged. A 15ns KrF laser pulse was used to excite the signals. 141

Fig. 71 Frequency spectrum of the signals shown in Fig. 70. 142

Fig. 72 Dispersion Curve Obtained for the 70±5nm thick DLC deposited on (001) Si substrate from the signal shown in Fig. 71. The generated positive slope of the dispersion curve

indicates that the velocity of Rayleigh wave in the carbon film examined is greater than that of substrate material Si. Large vertical steps in velocity in several frequency regions appeared due to the poor phase information in the frequency regions where S/N ratio is low. 143

Fig. 73 K-edge absorption peak for the carbon films produced with conventional PLD technique with different laser intensities (4.0 and 10.0 GW/cm^2 (sample # 7-(f) and 21-(c), respectively). Reduction of the π-peak was observed for the lower laser intensity. (a) full energy range (b) magnified plot in region of the π-peak. 148

Fig. 74 K-edge absorption peak observed from the sample made with conventional PLD technique (sample #21-(c)) and PLD with magnetic guiding system (sample #18-(a)) at an intensity of 10GW/cm^2. Reduction of the π-peak amplitude was observed for the latter sample. (a) full energy range (b) magnified plot in the region of the π-peak. 149

Fig. 75 The graphite spectrum regenerated from the literture published by Fallon [44], Pregliasco [77], and Zaluzec[78]. Pregliasco's spectrum was employed for the quantitative estimation of sp^3 fraction. 150

Fig. 76 Graphite and non-hydrogeneted amorphous carbon spectrum taken by Pregliasco [77]. Data were deconvoluted for the quantitative analysis. 151

Fig. 77 π-peak fits obtained from the various carbon samples fabricated with different deposition conditions. 152

Fig. 78 π–plasmon peak (5~10eV) and π+σ–plasmon(20~30 eV) peak observed from the carbon films made by PLD with different laser intensities (10 GW/cm^2 (sample #21-(c)) and ~0.7GW/cm^2 (sample #6-(e))). 153

Fig. 79 π–plasmon peak (5~10eV) and π+σ–plasmon(20~30 eV) peak observed from the carbon films made by PLD with magnetic guiding (sample #18-(a)) and without magnetic guiding (sample #21-(c))with the laser intensity of 10GW/cm^2. 154

Fig. 80 Percentage of sp^3 bonding(measured from the C-K 1sp transition) as a function of plasmon energy (position of the π peak from the energy loss spectrum) for different forms of carbon The solid line indicates the general trend for nonhydrogenated carbon films. The presence of hydrogen lowers the film density and plasmon energy (dotted line). The large filled circle at the bottom left represents grain-boundary amorphous carbon [44].* 155

I Introduction

I.1 Bonding in carbon

Carbon is known as the lightest element from group IV of the atomic table which can form various kinds of allotropes namely, diamond, graphite and fullerenes. Carbon contains six electrons with a $[1s^2][2s^22p^2]$ configuration in its ground state. Carbon has four L shell electrons, i.e., two in the 2s orbital and two in the 2p orbital, which take part in bonding to neighbouring atoms. These L shell electrons may be hybridized into three different configurations namely, sp^3, sp^2, sp^1 as shown in Fig. 1 which contribute to the formations of allotropes mentioned above [1].

In tetrahedral sp^3 bonding, all electrons in the L-shell are used to form covalent bonding with the neighboring atoms which is known as σ-bonding. Diamond, which is made of 100% of sp^3 bonding has an extreme hardness and high atomic density due to the strength of the σ-bond and the tetrahedral structure of sp^3 bonding.

In sp^2 bonding three electrons in the L-shell are used to form a lopsided hybridized configuration which will make σ-bonds with the neighboring atoms in a plane and one electron lies in a π orbital normal to the σ-bond plane as shown in Fig. 1. Graphite, which is made of 100% of sp^2 bonding, has strong bonding in the plane made of hexagonal rings formed by strong σ-bonds whereas it has weak π bonding along the perpendicular axis to the plane which allows easy separations of graphite planes. In graphite π-electrons are delocalized and therefore can move readily within a single plane layer but cannot easily move from one layer to another.

In the sp^1 or simply sp configuration as found in acetylene and the carbynes, one s-orbital and two p-orbitals perpendicular to the others are formed as shown in Fig. 1. It is found that number density of the sp^1 configuration is negligible in diamond-like carbon [2].

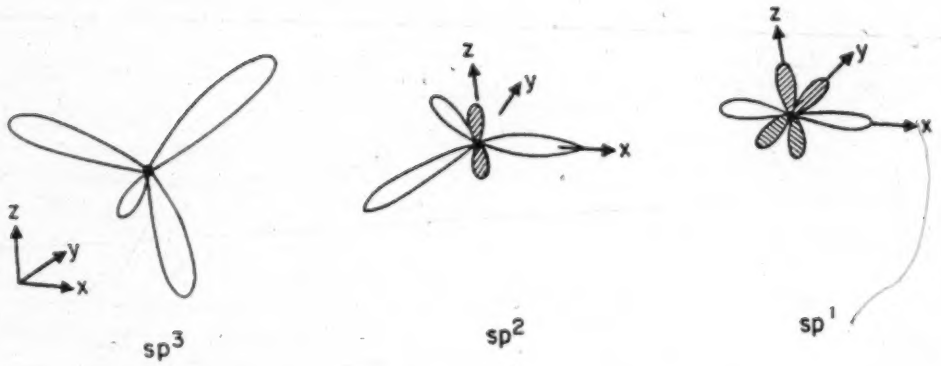

Fig. 1 Schematic representation of sp^3, sp^2 and sp^1 hybridized carbon. π-bonds are shaded and σ-bonds are unshaded [1].

I.2 Introduction to thin diamond-like carbon films

The deposition of thin films onto the surface of materials is a well-known technique for enhancing the surface properties of many materials. A hard material which has both a smooth surface and chemical inertness would be ideal for wear resistive applications. However, in general, hard materials are limited in shape variations, are expensive, and their properties outside of hardness may not be suitable for the purpose of the application. Thin film coating has been exploited to allow a combination of very hard surface properties with other desirable bulk properties. By depositing hard materials onto the surface of the component, one can obtain a material which has both the desired shape and bulk properties together with a hard shell. At present, carbides and nitrides (e.g. TiN, Ti(CN) and WC)[3,4] are dominant surface coating materials in the hard coating industry [5]. However, Diamond-Like Carbon, which is to be described in the following paragraphs, has recently been recognized as a well-suited material for protective coatings.

The term "Diamond-Like Carbon (DLC)" was first introduced by Aisenberg in 1971 to describe the carbon film whose properties are similar to those of diamond [6]. DLC is not a natural material and can only be produced through artificial production methods. It is very sensitive to the various environmental conditions in the coating processes, which implies both difficulty and flexibility in controlling its properties.

Basically, DLC is divided into two categories: amorphous DLC (a-C) and hydrogenated DLC (a-C:H or H-DLC). a-C is composed of chemically bonded small clusters (5-10 nm in diameter) of amorphous diamond and graphite, and is viewed as an amorphous material from a macroscopic viewpoint. a-C contains only very small amounts of hydrogen (< 1 atomic percent) or argon in the lattice as well [7]. The overall

structure has not been confirmed yet. a-C:H is also considered as an amorphous material in the macroscopic viewpoint, but the difference is that it contains a large amount of hydrogen (up to fifty atomic percent). Its structure is basically similar to that of a-C. It is believed that hydrogen plays an essential role in increasing the sp^3 / sp^2 ratio. Although the exact location of the hydrogen atom has not been determined yet, it is presumed that hydrogen terminates the carbon network because of its monovalence feature. An increase of sp^3/ sp^2 ratio has been observed when hydrogen content is increased [7] as shown in Fig. 2.

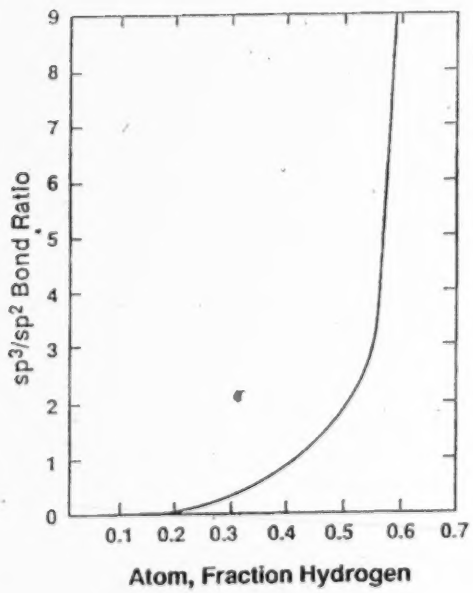

Fig. 2 Ratio of sp^3 to sp^2 hybrid bonds in diamond-like carbon (DLC) made using CVD deposition as a function of hydrogen content [7].

Chemical Vapor Deposition (CVD), Physical Vapor Deposition (PVD), Ion Beam, and Laser Plasma Deposition are basic methods to produce DLC. CVD is the most conventional technique applied in industry. In CVD, a carbide gas such as methane, butane, or acetylene, and hydrogen gas are fed into the vacuum chamber [8] as shown in Fig. 3. In the coating chamber, the heated substrate is exposed to these gases. The gasses in the chamber are activated by thermal (e.g. hot filament or arc discharge), electrical, or electromagnetic (e.g. microwave discharge or radio frequency induced discharge) means. Because the substrate is heated, chemical reaction arises on the surface of the substrate and carbon materials are formed on the substrate. The temperature of the substrate is raised to 700 ~ 1000 °C for producing CVD diamond and lower temperatures down to room temperature for producing DLC. The high substrate temperature required to produce CVD diamond limits the choice of substrates. Since hydrogen is required in this method, a-C:H is the most common carbon material made by CVD.

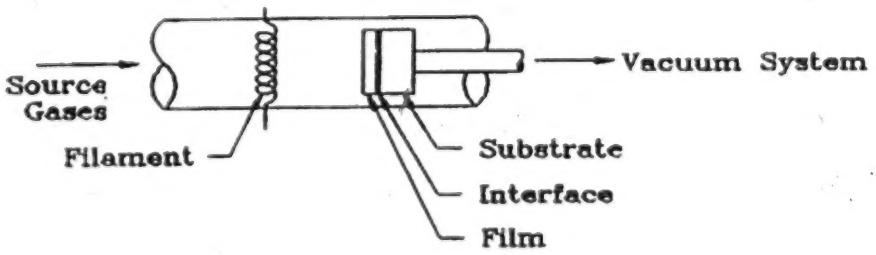

Fig. 3 One type of Chemical Vapor Deposition uses a hot filament. Gases containing carbon and hydrogen are fed into a vacuum chamber and activated via a hot filament. The substrate is heated to a temperature between 700 and 1000°C. Through chemical reactions, both diamond and graphite are deposited on the substrate, but the graphite is etched away by hydrogen [8].

In PVD, the deposition of film materials is carried out through the physical deposition of atoms onto the surface. Sputtering is one of the PVD methods. Fig. 4 shows a schematic diagram of sputtering [8]. In this method an ion beam is used to bombard the carbon target. By physical collision some neutral carbon atoms are "sputtered" to the substrate and form carbon materials. A continuous wave laser or dc arc evaporation may also be used instead of ion beams.

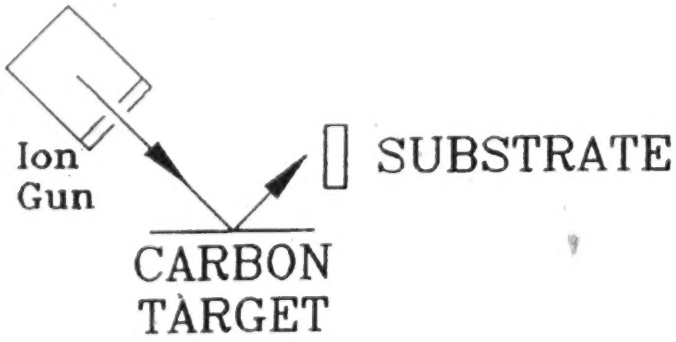

Fig. 4 Single beam sputtering is one method of Physical Vapor Deposition. An ion gun is directed toward a carbon target and carbon atoms are removed and deposited on the substrate [8].

The mechanism of Pulsed Laser Deposition (PLD) is basically similar to that of PVD. Fig. 5 shows schematic diagram of PLD setup [9]. The difference between these methods is that in Pulsed Laser Deposition, a train of high intensity laser pulses is used to irradiate the target. Since the injected power density to the target is high, the carbon target is heated to extremely high temperature and produces a mixture of plasma ions, neutrals, and macro-particles which expands toward the substrate and produces DLC. It has been reported that ion particles with high kinetic energy contribute to the quality of DLC [10]. High quality DLC films have been produced with a low substrate temperature

below 65 °C . Some PLD techniques employ additional electric discharge excitation in the deposition stage mainly in order to promote further ionization of the ablation gas. A generic term "i-C" is used for the DLC with a high sp^3/sp^2 ratio fabricated with highly ionized carbon source [11].

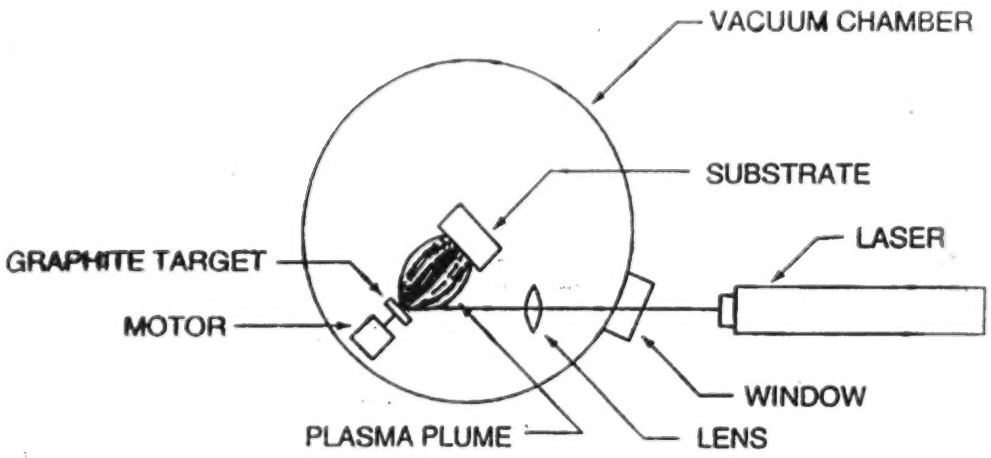

Fig. 5 Schematic diagram of pulsed laser deposition process [9].

High transparency in IR region [7,12], little restriction of geometry and size in coating, and extremely smooth surfaces (although the coefficient of friction is sensitive to humidity) which cannot be observed from CVD diamond, are known as unique characteristics of DLC. DLC coatings have already reached the production stage with applications in wear and erosion protection and in optics, such as DLC coatings for video tapes, high-density magnetic recording disks [13,14,15], watch parts [16], and anti-reflection coating by controlling the index of refraction [17]. However, the lack of high

temperature resistance (280 °C ~ 350 °C) due to the poor adhesion of the film to the substrate and decomposition (especially for a-C:H) and limitations in thickness because of intrinsic stresses using non-laser coating techniques preclude DLC from cutting and grinding-tool applications.

I.3 Principles of pulsed laser deposition of thin films

I.3.1 Introduction

Lasers are known as highly coherent sources of light. Because of this high coherence, one can produce a laser pulse with high power density (typically 10^9 to 10^{12} W/cm^2 with spot sizes of the order of .001~1 mm^2, wavelengths of 0.25 to 10.6 μ m, and temporal pulse duration of 0.1 psec to 1 msec). This is accomplished by compressing the original pulse temporally, using Q switching, gain switching, mode locking and pulse compression techniques and by focusing to small spatial spots [18]. Such high intensities allow for local heating and material processing via surface interactions and also allow for vaporization and ionization of material for application in thin film coatings.

Pulsed laser plasma deposition applies this technique to produce a source of a given desired material, which is to be deposited onto a substrate [19]. Fig. 5 shows a schematic diagram of a pulsed laser deposition apparatus. Laser energy is first absorbed by the target. Since an enormous amount of power is delivered in a short time, the surface of the target becomes a plasma. The plasma expands with a high kinetic energy and forms a so called "plasma plume". In the early stage of the plume expansion, the energy state of the plasma is regarded as isothermal due to the high thermal conductivity of the plasma. When the laser radiation stops, the energy state of the plasma plume becomes adiabatic [20]. During the plasma plume growth the shorter the laser pulse duration, the shorter the isothermal stage and longer the adiabatic stage. The intensity and wavelength of the laser affects properties of the films produced. Various diagnostic measurements such as optical emission and absorption spectroscopy, mass spectrometry and Langmuir plasma

probes have been utilized in order to study the predominant species in the laser induced plasma plume [21]. Various ideas to improve the film quality produced by pulsed laser deposition have been reported and examined including ion bombardment of the film under deposition, ion acceleration by electric field, electric discharge of the ablation gas, and discharge heating of the plasma as introduced in the following section [10,22,23,24]

I.3.2 Previous Results

Many studies on pulsed laser plasma deposition have been reported both experimentally and theoretically [19,25]. While various kinds of thin film devices (such as, GaAs heterojunction semiconductor [26,27], superlattice semiconductor [28], high Tc superlattice superconductor [29]) fabricated with this method have been reported, for the purpose of this report, I will only discuss those related to the production of diamond-like carbon films.

In pulsed laser deposition i-C DLC has been studied more than i-C:H since one of the strong points of this technique is the potential to fabricate films with high sp^3/sp^2 ratio without hydrogenation, which increases the hardness of the film. In this way, only i-C film will be discussed here.

Pulsed laser deposition of diamond like films was first performed by Marquardt et al [30]. They reported that the transition from soft to hard carbon was observed to occur for increase in laser pulse power density over ~5×10^{10} W/cm^2 for 6ns laser pulses at a wavelength of λ=1062nm (Q-switched Nd:YAG laser) as shown in Fig. 6a. Collins et al [31] have subsequently termed this threshold energy density for hard carbon as the Nagel criterion for obtaining good quality DLC films. Some theories such as the shock

synthesis model[32] and the model based upon preferential sputtering of the more weakly bonded carbon atoms[33] support this threshold energy density. It is expected that higher energy carbon ions with plasma electron temperature of ~40eV, which has been produced by the laser pulse power density over $\sim 5\times10^{10}$W/cm^2, lead to this sputtering process. Evidence for a higher plasma temperature and thus ion energy was also reported above this threshold intensity by Marquardt et al as shown in Fig. 6b. The experimental result reported by Sato et al [34] also supported this threshold observation.

Various concepts have been proposed for the further improvement of film quality and the growth rate. Fujimori et al [22] first employed a combination of laser and ion beams as shown in Fig. 7. It is reported that the films deposited by this hybrid technique showed significant rise in electrical resistivity, optical transmittance and hardness as compared to the films prepared without ion bombardment during deposition. Wagel et al reported that significant enhancement of coating rate was obtained by an additional electric grid in the laser-generated plasma plume [23]. Collins improved Wagel's system by employing discharge through the plasma plume as shown in Fig. 8a [10]. A high growth rate in a large deposition area (0.5 μ m/hr in 20 cm^2 with the Nd:YAG laser with a laser pulse intensity of $5*10^{11}$W/cm^2 at a repetition rate of 10Hz) was achieved by their method. The laser energy per pulse was not mentioned in the reference [10], but typically is ~1J/pulse. Subsequently, Krishnaswamy et al [24] reported that microhardness, uniformity and homogeneity in DLC films have been improved by synchronizing laser ablation of the target with the injection of capacitively stored energy (2.3 J at 3 kV) into the ablated plasma plume as shown in Fig. 8b.

An experimental study of interface structure was reported recently [35]. Ultrathin epitaxial DLC films on Si<100> fabricated by L-PVD (Laser-induced Physical Vapor Deposition) technique were characterized by surface techniques and STM (Scanning Tunneling Microscope). The diagnosis of the films revealed that the surface lattice forms hexagonal structure with nearest neighbor distance ranging from 2.52 $\mathring{A}$ to 2.46 $\mathring{A}$. The crystal structure of further growth appeared to be amorphous. The last decade indeed has witnessed substantial progress in deposition techniques and in the characterization of properties of the deposited films as a result of these studies of PLD techniques and hybrid techniques.

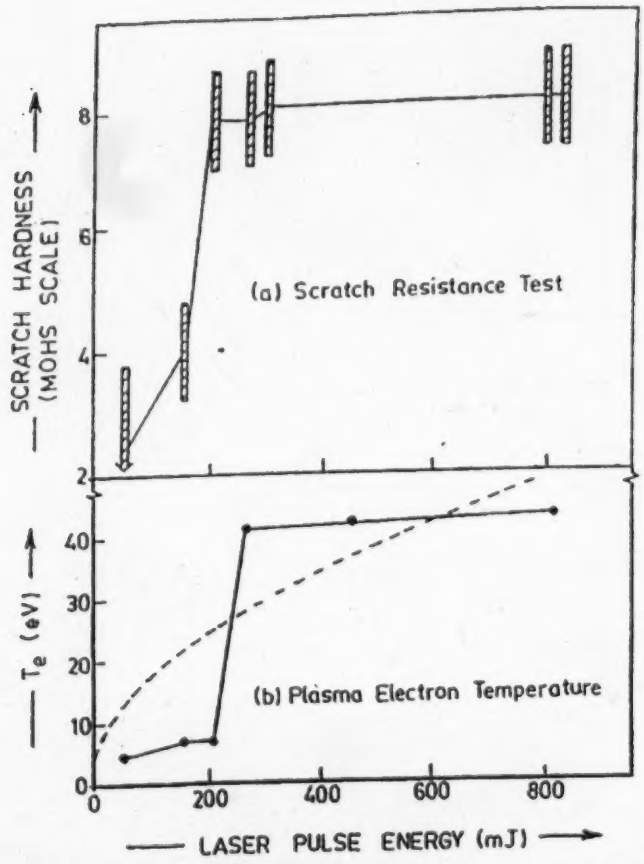

Fig. 6 Scratch Hardness (a), and (b) plasma electron temperature as a function of laser pulse energy. Data points shown in (b) are estimates of T_e from X-UV spectra: dashed curve shows dependence anticipated from theory [30].

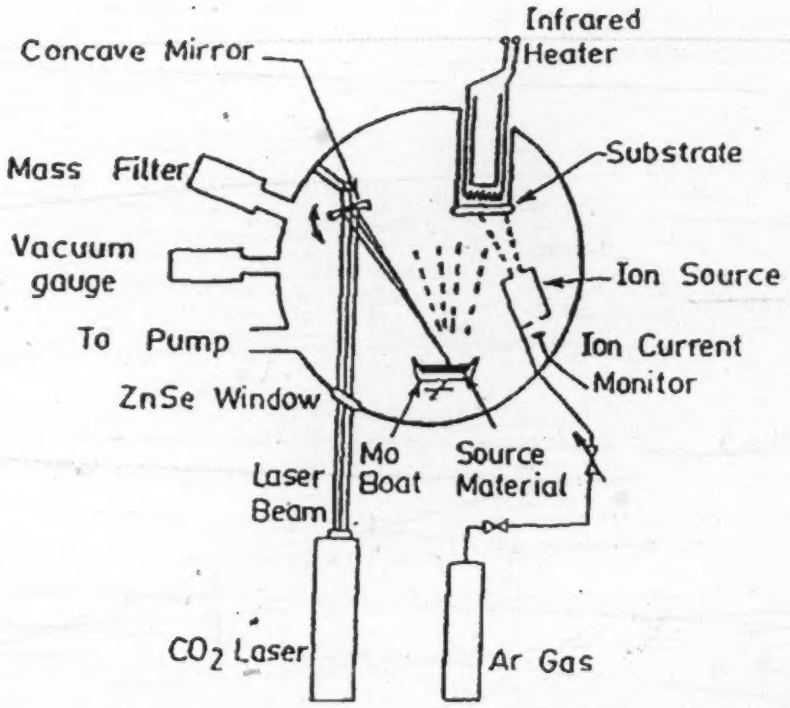

Fig. 7 Schematic diagrams of laser deposition facilities which involve some supportive techniques to improve the film quality and the growth rate. Substrate heating and ion bombartment on the substrate are employed [22].

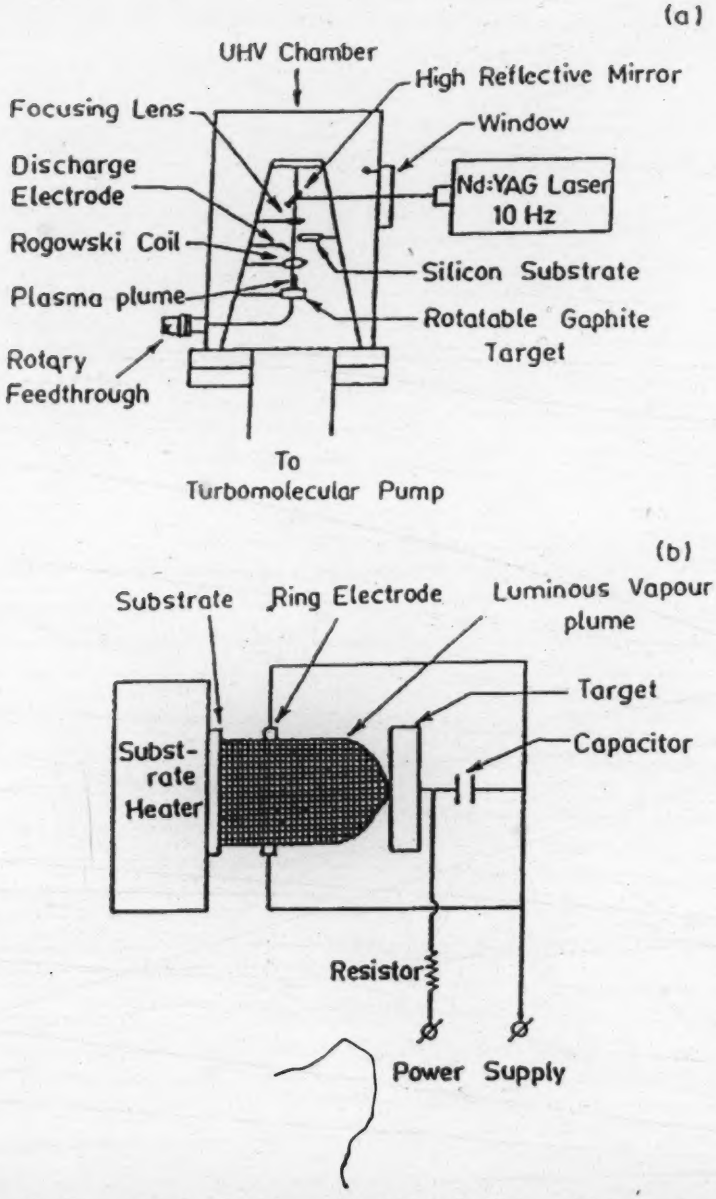

Fig. 8 Schematic diagrams of pulsed laser deposition facilities which involve some supportive techniques to improve the film quality and the growth rate. (a) employs electric discharge and ion acceleration [10]and (b) employs the injection of capacitively stored energy into the ablated plasma plume [24].

I.4 Development of the Magnetic Guiding of Plasma

Our laboratory has been working on the magnetic guiding of the plasma sources from the ablation plume in order to extract a pure coating plasma which may produce different properties of the thin film compared with those produced by conventional pulsed laser deposition. Both theoretical and experimental work has been carried out in order to obtain a better understanding of the plasma properties and efficiency of guiding to the coating substrate [36].

I.4.1 Motivation

PLD with high laser intensity is known as a means for the fabrication of the thin films with good properties for protective coatings. However, one inherent problem for the PLD method with high laser intensity is the generation of nanometer to micron size debris particles from the source material which become embedded in the coating produced. These inclusions deteriorate the performance of the protective coating because they are significantly weaker than the DLC film and act as weak spots for corrosion or mechanical wear.

The wear resistance of a PLD deposited DLC film was examined by scratching the film with a razor blade. Fig. 9 shows SEM pictures of the film surface taken before and after the scratch test. It was found that the region covered with macro-particles scrapes off quite easily. The deterioration of the film spreads out from the damaged region when film was scratched more. This observation suggests that the film damage could be caused by the presence of the macro particles on the film.

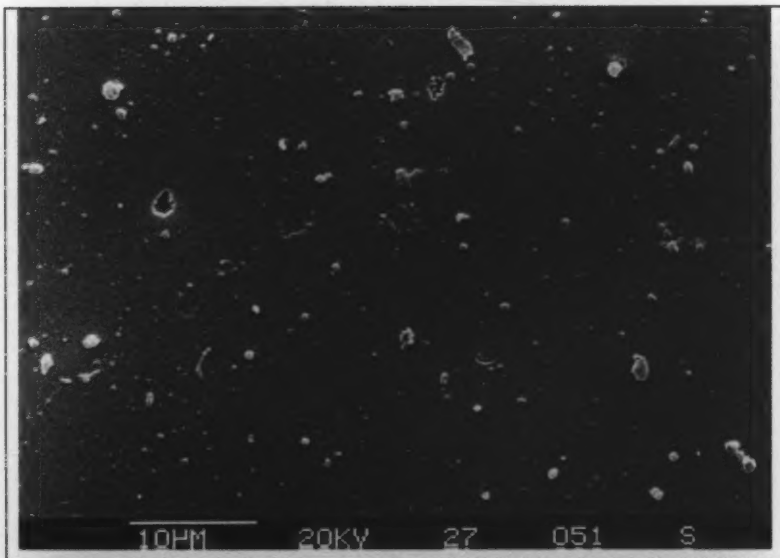

Debris on surface

Nd:YAG
10^{11} W/cm^2
1.5μm coating

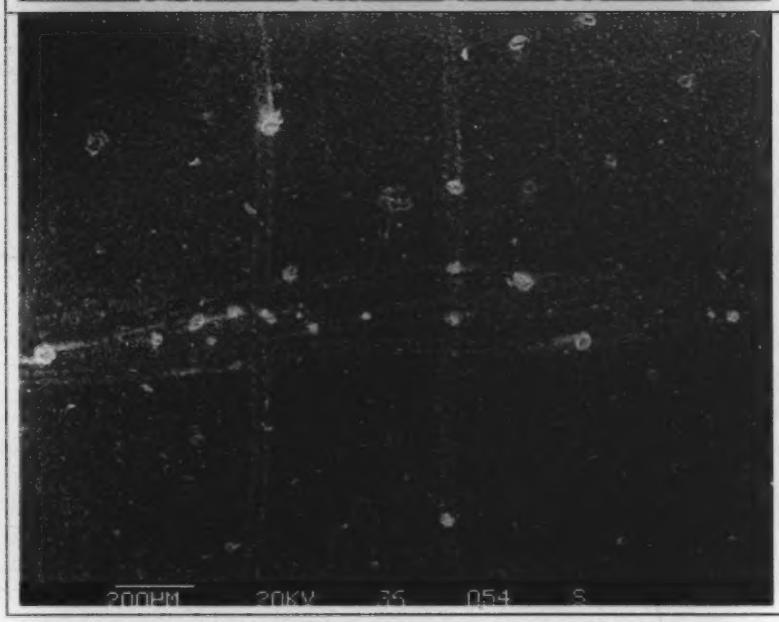

Failure spots
in scratch test
initiated at debris
sites on surface

Nd:YAG
10^{11} W/cm^2
1.5μm coating

Scratched with
razor blade

Fig. 9 Razor blade scratch test of PLD diamond like carbon film [36].

I.4.2 Plasma guiding for debris reduction

A magnetic plasma guiding system has been developed as a possible means to solve this problem by steering the plasma around a bent magnetic field so that debris particles cannot directly reach the coating substrate. The system includes 2 or 3 solenoids coils placed as shown in the insets of Fig. 10. As shown in the figure, the KrF laser pulse is focused onto the target material (50mJ/pulse, $2x10^{10}Wcm^{-2}$) placed at the entrance of the series of solenoid coils. The laser creates an ablation plume which is a mixture of electrons, ions (K.E~200eV), nanometer scale neutral particles, and micrometer scale particles (debris). Our aim is to extract only pure plasma out of the rest of the ablation gas by confining the plasma with a strong magnetic field (B_p=0.3T) produced in the solenoid coil. In our system, a pulsed electric current (I_p=300A), which is synchronized with the trigger pulse used to trigger the laser, goes through the solenoid and creates a transient B-field during the time period when plasma is going through the solenoid. The duration of the magnetic field is on the order of 1ms which is much longer than the transit time of the ions throught the magnetic guide which typically is around 10μsec. Therefore, the magnetic field is effectively constant during the plasma deposition process. Using copper plasma from laser pulses focussed on a copper block the number of debris particles observed on the coating surface was 60,000 particles per mm^2 without magnetic guiding for KrF laser pulses at 100mJ energy versus 50 particles per mm^2 after a curved magnetic guide field for films with approximately the same thickness [37]. However, for carbon the reduction in debris was less pronounced. The population density of the debris particles for carbon, which are more than 1μm in diameter, on the film made at 15cm from the plasma source without magnetic field was approximately 500 particles/mm^2

(6500shots with 100mJ). The same population density was found for the film made by the ablation species which had propagated for 15cm through the two-solenoid geometry. However, population density reduced down to 100 particles/mm^2 for the coating made by the ablation species which had propagated for 40cm from the target through the three-solenoid geometry as shown in Fig. 10. The bend angle between the first and second solenoid is 30degrees. The good reduction of debris particles for copper coatings is due to the fact that most of the particles are liquid which tend to stick to the first surface hit. For carbon the particulates are expected to be solid and tend to fragment upon impact. Thus while a number are blocked by the baffles in the guide tube a fraction will fragment leading to a higher starting number of smaller size particulates. In this case an increase in guide tube length will be required to obtain the desired reduction in debris particles.

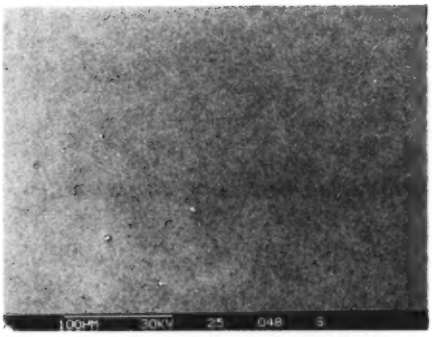

Debris for total of
650J laser energy
Krf $2x10^{10}$ W/cm^2

Without magnetic guiding

~500 particles/mm^2 > 1 μm

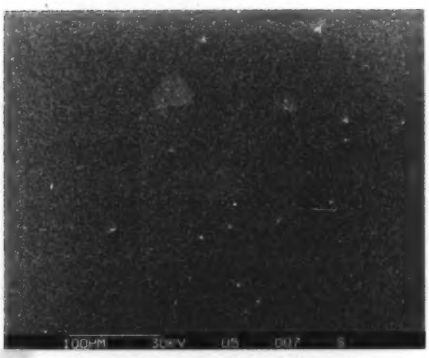

15cm from target after 2 short coils with baffles

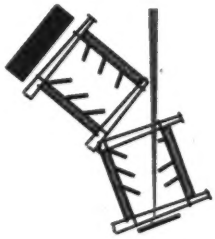

~500 particles/mm^2 > 1 μm

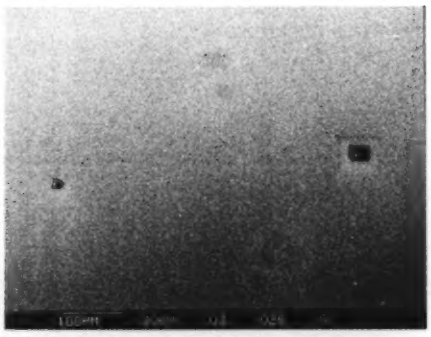

40cm from target after 3 coils with baffles

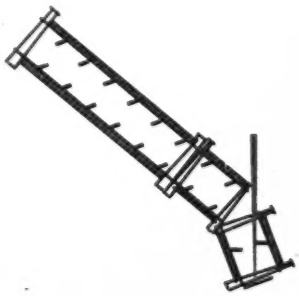

~100 particles/mm^2 > 1 μm

Fig. 10 Debris Reduction with Long Tube Geometry. Population density of the macro particle whose diameter is more than 1 μm was reduced significantly with 40cm plasma guiding with 3 coils geometry [36].

I.4.3 Current Setup for Magnetic Guided Pulsed Laser Deposition Facility

A pulsed laser deposition facility with a curved magnetic plasma guide has been developed at the University of Alberta. A schematic diagram for the setup is shown in Fig. 11. The facility employs one solenoid which has the inner and outer radius of the curvature of approximately 77cm and 80cm, respectively. The length of the arc at the middle point of the cross section of the solenoid is 46cm. The solenoid is covered with a water jacket in order to dissipate the heat created upon the generation of the magnetic field. Deionized water is used in order to avoid discharge breakdown through the water. Carbon tape (GRAFOIL® TAPE by UCAR CARBON COMPANY INC. GRAFOIL Products, Ohio, USA. [38]) is used as the source target material. The tape target is placed parallel to the face of the entrance of the solenoid and is 3cm away from the face of the entrance. A 0.5 T permanent magnet is placed at the back side of the tape target in order to cause more uniform magnetic field region at the entrance to the solenoid.

With the plasma guide, one can extract pure plasma from the ablation species and, therefore, comparisons can be made between the laser-plasma coatings obtained using the normal laser plasma and those obtained with pure ion plasma using the magnetic guiding technique. Using the split coil geometry shown in Fig. 10. It would also be possible to compare films made using the pure ion plasma with those produced by the residual neutral particles escaping through the gap between the coils and differentiate the contribution of various coating species to the properties of the resultant thin film. However, the latter experiment was not carried out as part of this thesis research.

It should be noted that improved film qualities of carbon films prepared by vacuum cathode arc deposition with curved magnetic solenoid have been reported [39,40,41].

Fig. 12 shows the apparatus for Mass Selective Ion Beam (MSIB) deposition by magnetic filtering employed by McKenzie et al [41]. In their apparatus a cathode arc is employed for the ion source. The analyzer filters neutrals, cluster species, graphitic fragments and impurities from the beam and allows only a pure beam of C^+ (or C^-) ions to reach the substrate. The films made with this method were found to be fully amorphous (not crystalline) with the highest fraction of sp^3 bonding (~80%) for those from any present deposition process. The main practical problem with this method is the high compressive stress in the films, which limits their adhesion. The kinetic energy of the plasma and the strength of the magnetic field were not mentioned in the paper.

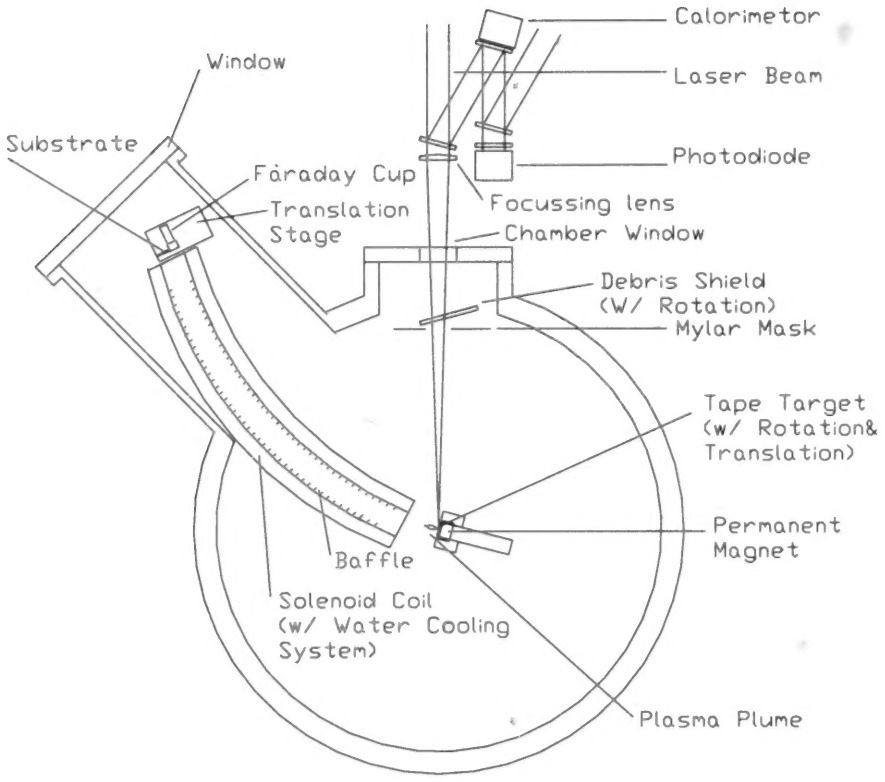

Fig. 11 Schematic diagram of magnetic plasma guide developed at the University of Alberta. Ionized species are guided by magnetic field generated by the solenoid coil.

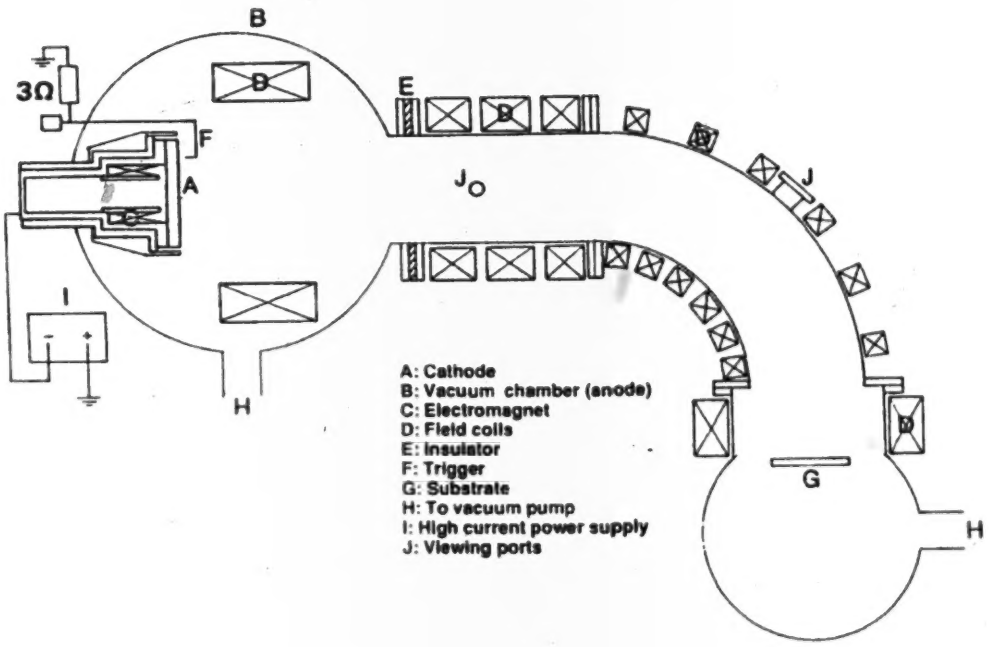

Fig. 12 Apparatus for Mass Selected Ion Beam deposition by magnetic filter, using a cathode arc source, after McKenzie et al [41].

II Important Properties of Thin Diamond-Like Film and Diagnostic Measurement Techniques

There are several important properties of thin films which should be characterized in order to assess their suitability for a particular coating application. These include thickness, density, hardness, Young's modulus, stress, index of refraction, and conductivity, etc. In this chapter these properties will be discussed for diamond-like carbon films and diagnostic techniques used to measure these properties will be discussed.

II.1 Mechanical Properties

The important mechanical properties are Young's modulus(E) and Hardness(H). An example of some measured mechanical properties for various forms of diamond-like carbon and other thin film coatings are shown in Table 1[42]

One can see that the Young's modulus of the carbon films except C60 and graphite is about 10 times bigger than the Hardness. Therefore Young's modulus is often used as an indicator of the hardness of the film. The table also shows that DLC produced by Mass Selective Ion Beam (MSIB) and polycrystalline diamond produced by the CVD technique have properties very close to that of pure diamond. Techniques which can be employed for measuring these properties are described in the following sections.

Table 1 Mechanical properties: Comparison of Young modulus, bulk modulus, shear modulus, Poisson ratio, hardness and yield stress [42]

	Young's modulus *E* (GPa)	Bulk Modulus *B* (GPa)	Shear Modulus *S* (GPa)	Poisson's ratio ν	Hardness *H* (GPa)	Yield Stress *Y* (GPa)
Diamond	1050	442	478	0.104	103	59
CVD diamond	730-850				60-90	
PD a-C:H (100V)	145	52	24	0.4	16	9.7
PD a-C:H (1kV)	55	23	31	0.2	6.3	3.1
a-C (sputtered)	140				15	3
a-C (MSIB)					20-110	12-65
Graphite	686					
Glassy C (GC10)	29		12.5	0.15	3.0	1.0
Glassy C (GC20)	32		13.5	0.17	2.2	0.73
C60	12	6.4		0.18		
Si	130	97.8	50.9	0.278	10.4	5.0
a-Si:H	100			0.32	10.0	4.9
Cubic BN					41-71	
WC					21	

II.1.1 Thickness and density

Thickness can be measured directly by a stylus instrument. To exploit this method one must prepare a smooth substrate and make a sharp step at the edge of film by physically masking the surface during deposition or photolithographic etching technique after deposition. Instruments available at AMC and the University of Alberta microlithography laboratory allow such measurements with an accuracy of ± 4 nm as shown in Fig. 13. With this instrument large scale surface roughness can also be measured. The film mass can be measured by the microbalance available at the Microanalytical Laboratory in the Department of Chemistry in the University of Alberta by weighing the substrate before and after deposition. From the thickness and areal mass density one can calculate the density of the film.

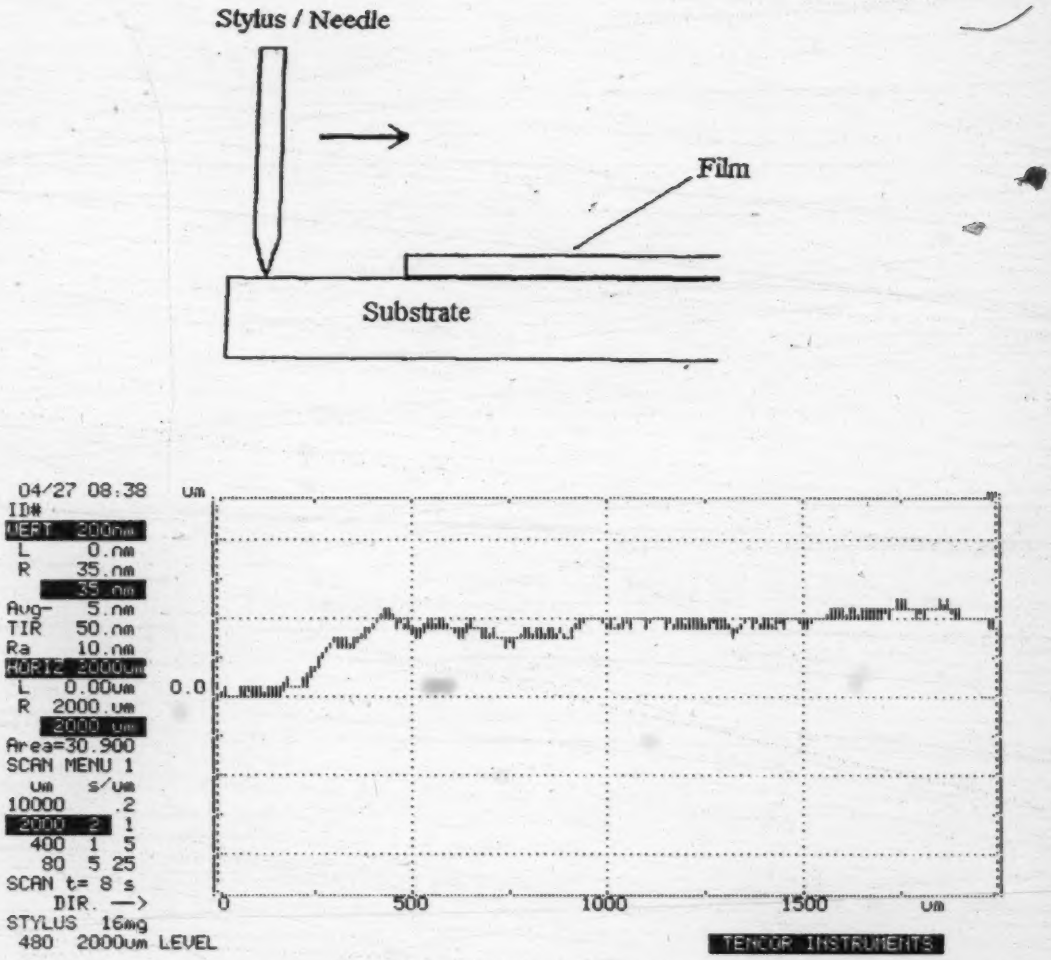

Fig. 13 Schematic diagram of a stylus instrument and an example of the measurement. A 40nm thick copper film on a silicon substrate is profiled. The grid space represents 500μm per division on the horizontal scale and 40nm per division on the vertical scale.

A quartz crystal oscillator is another tool which measures the areal mass density of the film and gives the thickness of the film if the density of the film is known. This tool measures the difference in resonant frequency with the film and without film on the surface of the quartz crystal. When the initial resonant frequency for quartz f_q is shifted to f_c after a film is deposited on top of quartz plate, the product of film thickness t_f and density is given by

$$t_f \rho_f = \rho_q t_q \frac{\tan^{-1}\left(Z \tan(\pi F)\right)}{\pi Z (1 - F)} \qquad (1)$$

where

ρ_q : density of the quartz plate,

ρ_f : density of the film,

t_q : thickness of the quartz plate,

$F \equiv \frac{f_q - f_c}{f_q}$: normalized frequency shift and

$Z \equiv \frac{Z_q}{Z_f} = \frac{\sqrt{\rho_q \mu_q}}{\sqrt{\rho_f \mu_f}} = \frac{\rho_q v_q}{\rho_f v_f}$: the acoustic impedance ratio where

Z_q : Acoustic impedance of quartz

Z_f : Acoustic impedance of the film

μ_q : Shear modulus of quartz

μ_f : Shear modulus of the film

v_q : Shear wave velocity in quartz

v_f : Shear wave velocity in the film

When $F \sim 0$, the equation above can be approximated as

$$\rho_f t_f = \frac{v_q \rho_q}{2} \frac{f_q - f_c}{f_q^2} = N \rho_q \frac{f_q - f_c}{f_q^2} = \rho_q t_q \left(\frac{f_q - f_c}{f_c} \right) \quad (2)$$

where N= $1.67*10^6$ Hz*mm; a material constant for quartz. With this method, very high sensitivity of about one monolayer in thickness of mass density can be measured. With the thickness and areal mass density measurements combined one can then obtain the mass density of the film, which normally is less than bulk density (typically ~90% of bulk density).

Density can also be estimated from the plasmon peak obtained from Electron Energy Loss Spectroscopy (EELS) [43]. Plasmons are the quantized plasma oscillations caused by the valence electrons and have the strongest oscillation at a peak energy given by

$$E_p^{\ 2} = \hbar^2 \frac{N_e e^2}{\varepsilon_o m} \quad (3)$$

where E_p is the plasmon peak energy, $\hbar = h/2\pi$, h is Planck's constant, N_e is number density of the electron, ε_o is permittivity of free space, and m is the mass of the free electron. Fig. 14 shows some examples of the plasmon peak measured for the various kinds of carbon film [44]. It should be noted that this model is not valid for pure graphite. Since one carbon atom has four valence electrons the number density of the carbon atom in the film N_a can be estimated as

$$N_a \approx \frac{N_e}{4} = \frac{E_p^{\ 2} \varepsilon_o m}{4\hbar^2 e^2} \quad (4).$$

We could then estimate the mass density of the carbon film by using the equation given as

$$\rho = A \frac{N_a}{N_{avogadro}} \quad (5)$$

where ρ is the density of the carbon film, A is the atomic weight of carbon, and $N_{avogadro}$ is Avogadro's number.

Other ways of measuring density include sink float method [45], weight gain measurements during deposition, and Rutherford back scattering [46].

Pure diamond has a density of 3.515 g/cm^3. Graphite, on the other hand, has a lower density of 2.267 g/cm^3 for monolithic crystal graphite and 1.6 to 1.95g/ cm^3 for pyrolytic graphite due to its porous structure. The density of DLC ranges between these values. Hardness and density are somewhat correlated and, therefore density is often used as an indicator of a quality of DLC.

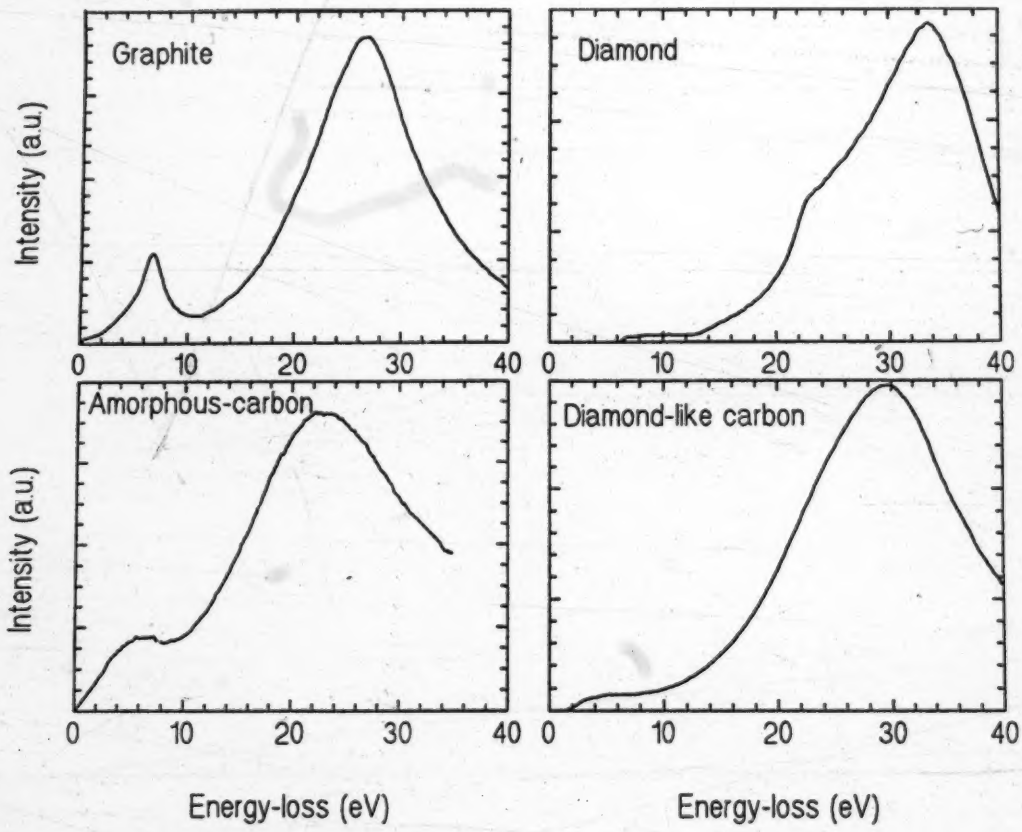

Fig. 14 Plasmon peaks of different forms of carbon measured by EELS [44].

II.1.2 Hardness

Hardness of protective coatings is a very important tribological parameter to know for a film. The stylus indentation method is a standard method to measure the hardness. In this method a stylus (usually diamond) is pressed onto the specimen as shown in Fig. 15 and hardness H is given by

$$H = \frac{\bar{F}}{A} \qquad (6)$$

where $\bar{F}$ = the applied force, and A= the indented area of contact.

In order to avoid the influence of the substrate, the indentation depth must be less than 10 % of film thickness. However, if the penetration is too small, the deformation of the stylus is no longer negligible and therefore causes some error. Usually, for the conventional stylus instrument, a minimum film thickness of several microns is required for an accurate measurement. In our case the films produced were much thinner and no direct hardness measurement was carried out.

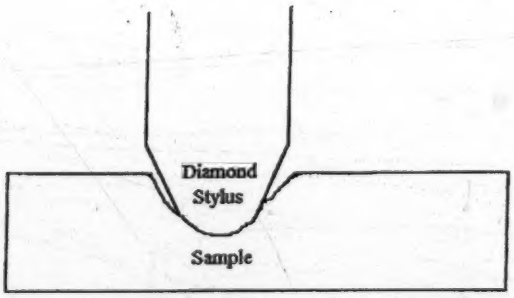

Fig. 15 Schematic diagram of stylus indentation.

II.1.3 *Stress and Adhesion*

Cracking, delamination, and buckling are the typical examples of film failure. It is understood that these are caused by excessive internal stress and poor adhesion to the substrate. Therefore, internal stress and adhesion are very important properties in terms of the stability of the film/substrate composite [11,42,47,48,49,50]

Stress can be measured by observing the bending of a thin substrate material after the application of the thin film. The disk method is a conventional method to measure stress of films using a circular disk substrate (Fig. 16). In the disk method, the deflection of the film is measured by observing interference fringes (Newton rings) appearing with reference to an optical flat. In this method the stress is given by the equation;

$$\sigma = \frac{\delta}{r^2} \frac{E_s}{3(1-\nu)} \frac{d_s^2}{d_f} \qquad (7)$$

Where δ is the upward deflection at a distance r from the center of the disk, E_s is the Young's modulus of the substrate, ν is the Poission's ratio for the substrate, d_s is the substrate thickness, and d_f is the film thickness. A glass, quartz, or silicon crystal wafer of 0.1 to 1.0 mm thickness is a basic substrate for this measurement method. The typical sensitivity of this method is of the order of 10 MPa.

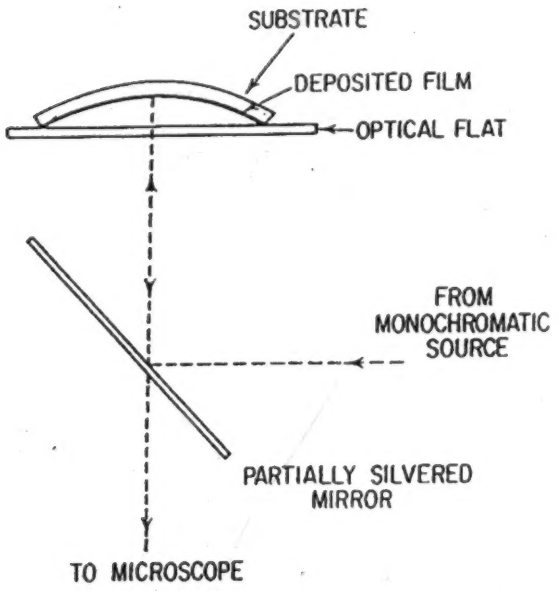

Fig. 16 Apparatus for observing fringes produced by the variable air gap between a stressed circular and an optical flat [47]

Another conventional method is the beam bending method. In this method, deflection of the unclamped end of the cantilever is measured as shown in Fig. 17 and the stress is given by the equation

$$\sigma = \frac{E_s}{6R(1-\nu)}\frac{d_s}{d_f} \tag{8}$$

This equation can be modified into an equation relating stress to end deflection by substituting

$$R = \frac{L^2}{2\delta} \tag{9}$$

where L= length of the cantilever, δ= deflection of the unclamped end of the cantilever, namely,

$$\sigma = \frac{\delta}{L^2}\frac{E_s}{3(1-\nu)}\frac{d_s^{\,2}}{d_f} \tag{10}$$

This method gives higher sensitivity (0.1MPa) than that given by the disk method. In this method, however, the substrate has to be about fifty times longer than it is wide. While this method utilizes a large variation of displacement detection systems, a capacitance system seems to give the highest sensitivity.

Adhesion is a very important property especially for protective film coatings since it gives a measure of how well the film adheres to the substrate. Although many techniques for testing adhesion exist, only the scratch test seems to give very meaningful results [51,52] In this method, an indenter (e.g. diamond tip) moves on the surface under an increasing load and eventually damages the film. The smallest load at which the coating is damaged (either by adhesive or by cohesive failure) is called the critical load L_c. Optical or Electron microscopy and/or acoustic emission is used to determine L_c.

Differential thermal expansion and intrinsic stress which is developed during the deposition are main causes of internal stress. The deposition microstructure is closely related to stress since intrinsic stress is caused by incorporation of impurities and incomplete structural ordering or structural reordering. Also stress is related to morphology of the microstructure, e.g. porous structure cannot sustain a high stress.

DLC produced by conventional coating techniques such as CVD, suffers from limitation in thickness for adhering films because of its extremely high internal stress [53]

Layers of i-C made by conventional methods are generally found to be poorly adherent when the film thickness is above about 1 μ m. However, carbon films produced by pulsed laser deposition using high intensity laser pulses can produce thicker film without sacrificing their mechanical properties. For example a 5 μ m DLC film was produced by Pulsed Laser Deposition using high intensity laser pulses , the thick film

showed no reduction in its hardness when compared with thinner film [50]. It appears that the internal stress of the films produced decreases as laser intensity to the target increases as shown in Fig. 18 [54]. Adhesion can also be improved with the formation of intermediate layers such as an interlayer of TiC which holds i-C film produced by pulsed laser deposition and a Ti substrate together as observed in previous work as shown in Fig. 19 [55].

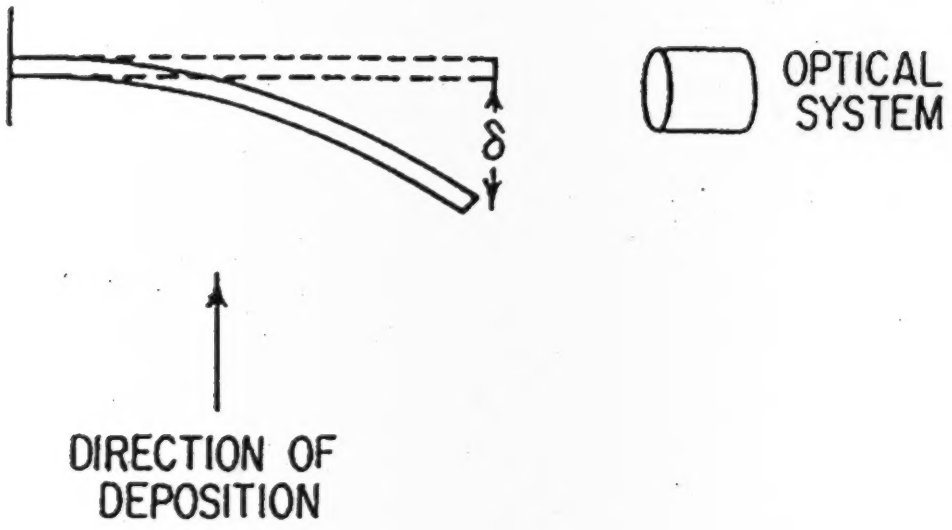

Fig. 17 Method of measuring stress by bending techniques. The displacement is measured by optical means in this case [47]

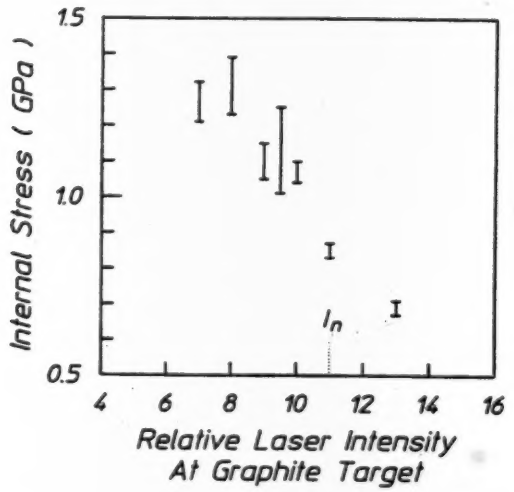

Fig. 18 Plot of the internal stresses of the amorphic diamond films prepared with deliberate alteration of laser intensity. Data are shown for films produced by laser beams having the indicated relative intensities. Nominal amorphic diamond films with 75% sp^3 fraction used in these experiments are produced with the relative laser intensity indicated by I_n which on the order of $10^{12}W/cm^2$ [54].

Fig. 19 Cross section of the amorphic diamond film on a $TiAl_6V_4$ substrate, thinned and then imaged by TEM. An interfacial layer of microcrystals of TiC is evident from the bright points due to the diffractions of electron beam [55].

II.1.4 Elasticity

Young's modulus E_s is the most common value used to indicate elasticity [47] The simplest way to measure Young's modulus is to load a known force on the end of the cantilever of length L and observe the deflection of the beam. The equation relating E_s to the deflection δ is

$$E_s = \frac{4GL^3}{wd_s^3\delta} \qquad (11)$$

Where G is the force placed on the end, d_s is the thickness of the substrate and w is the cantilever width. A plot of G against δ will thus give a value for E_s.

Recently, a more sophisticated technique, called "a surface acoustic wave (SAW)" monitor has been developed for measuring Young's modulus of thin films materials as shown in Fig. 20 [56]. This technique allows us to measure the relative Young's modulus to that of the substrate material with less restriction on the size and thickness of the films by looking at the dispersion of the acoustic wave as a function of frequency. Also, if the film thickness is similar to the wavelength of the surface acoustic wave (~ μ m), non-linear dispersion arises, and it allows us to measure not only Young's modulus, but also film thickness, density, and Poisson's ratio if a very precise measurement of dispersion is made. This technique will be described further in the next chapter.

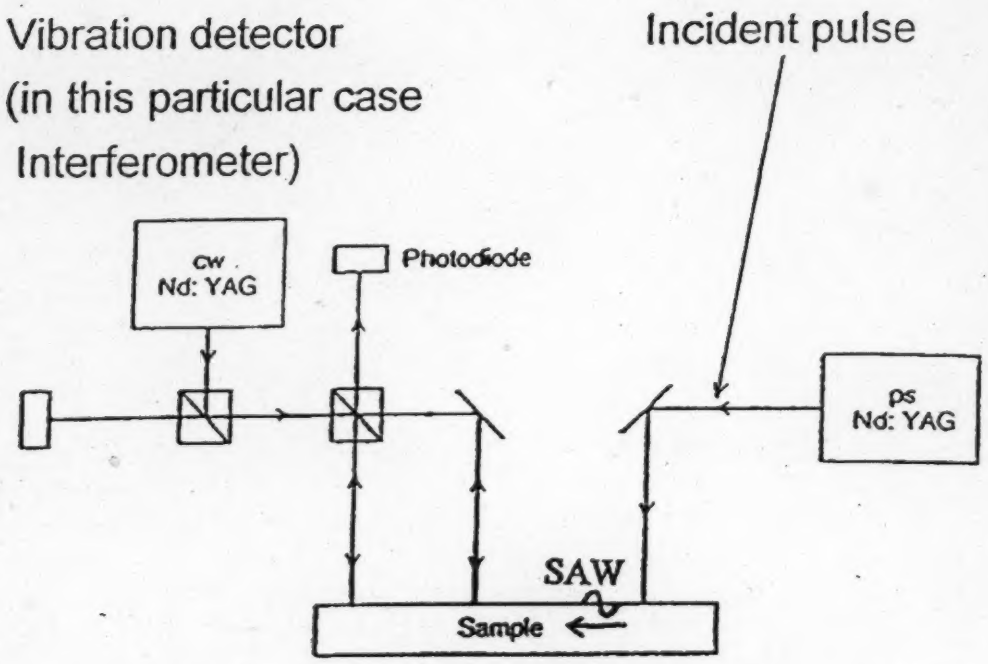

Fig. 20 Schematic diagram of SAW measurement apparatus [56]

II.2 Optical Properties

II.2.1 Index of Refraction

Index of refraction n in its complex form can be separated into its real part n_r and imaginary part n_i as

$$n = n_r + in_i \qquad (12).$$

The imaginary part of the complex index of refraction, also called extinction coefficient which is usually denoted as k, is a very useful quantity related to the absorption coefficient and is another indicator of film quality. The value n_i is described as follows [50]

$$n_i = \frac{\lambda \ln[I / I_o]}{4\pi d_f} \qquad (13)$$

where d_f=thickness of the film, λ=wavelength of the light, I=intensity at the incident wavelength λ transmitted by the combined film and substrate, and I_o=intensity transmitted by the substrate in the absence of the film, corrected for reflective losses created by the film. The wavelength λ =6328 Å of a HeNe laser is often used for the measurement because of convenience.

Fig. 21 shows the correlation between n_i and the intensity of laser pulse used to produce the DLC, the mass density, and the resistivity of the films [61]. From the figure, one can easily see that all three quantities decrease as n_i increases. Thus lower values of n_i correspond to higher quality films suggesting that n_i can be used as a convenient indicator of film quality.

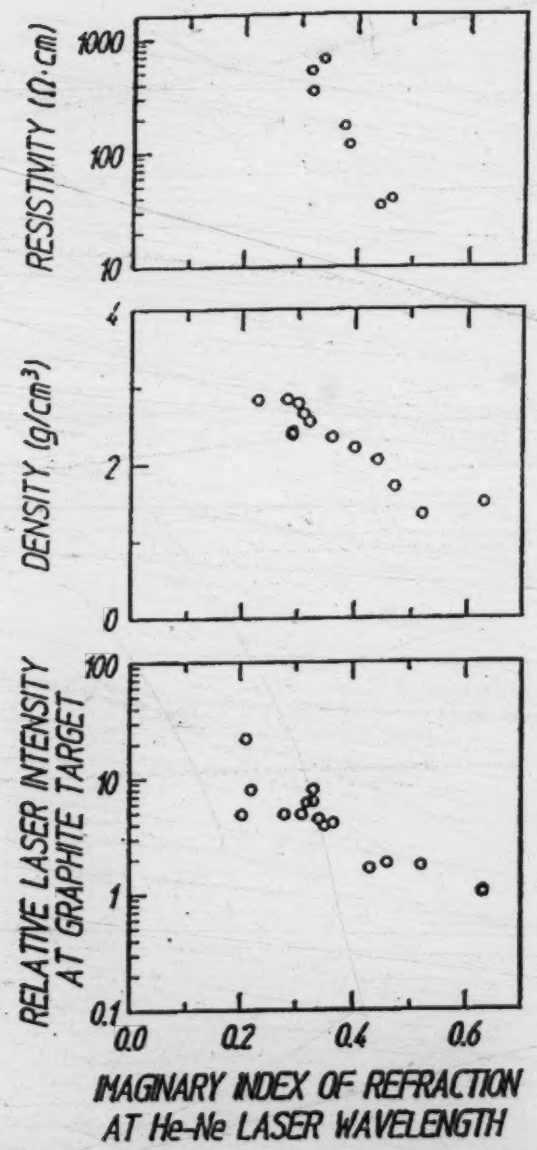

Fig. 21 Plot of electrical resistivities, mass densities, and relative laser intensities needed to produce amorphic diamond films with the values of n_i, the imaginary part of the complex index of refraction measured at 6328 Å as shown. Values of ordinates plotted for different properties at the same values of n_i do not necessarily correspond to measurements made on the same physical sample [61].

An optical ellipsometer can also be used to determine the thickness and the complex refractive index of the film. The V-shape ellipsometer, which is the most standardized ellipsometer, as shown in Fig. 22, measures two parameters Ψ and Δ which are defined as

$$\tan\Psi = \frac{\rho^p}{\rho^s} \qquad (14)$$

and

$$\Delta = \delta^p - \delta^s \qquad (15)$$

where ρ^p and ρ^s are the reflection coefficients of the components in and perpendicular to the plane of incidence after reflection; δ^p and δ^s, the absolute phase shifts of the same two components, brought about by the reflection. Usually a conventional ellipsometer instrument has simple calculation programs to deduce film properties based on the theoretical model [57,58] by using the measured values of Ψ and Δ, the complex refractive index for the substrate, and an approximate answers for the unknown film properties defined by the user. Numerical techniques to find such film properties are discussed in [59].

Such a V-shaped spectropic ellipsometer has been used to determine the complex refractive index of diamond-like carbon film as shown in Fig. 23 [60].

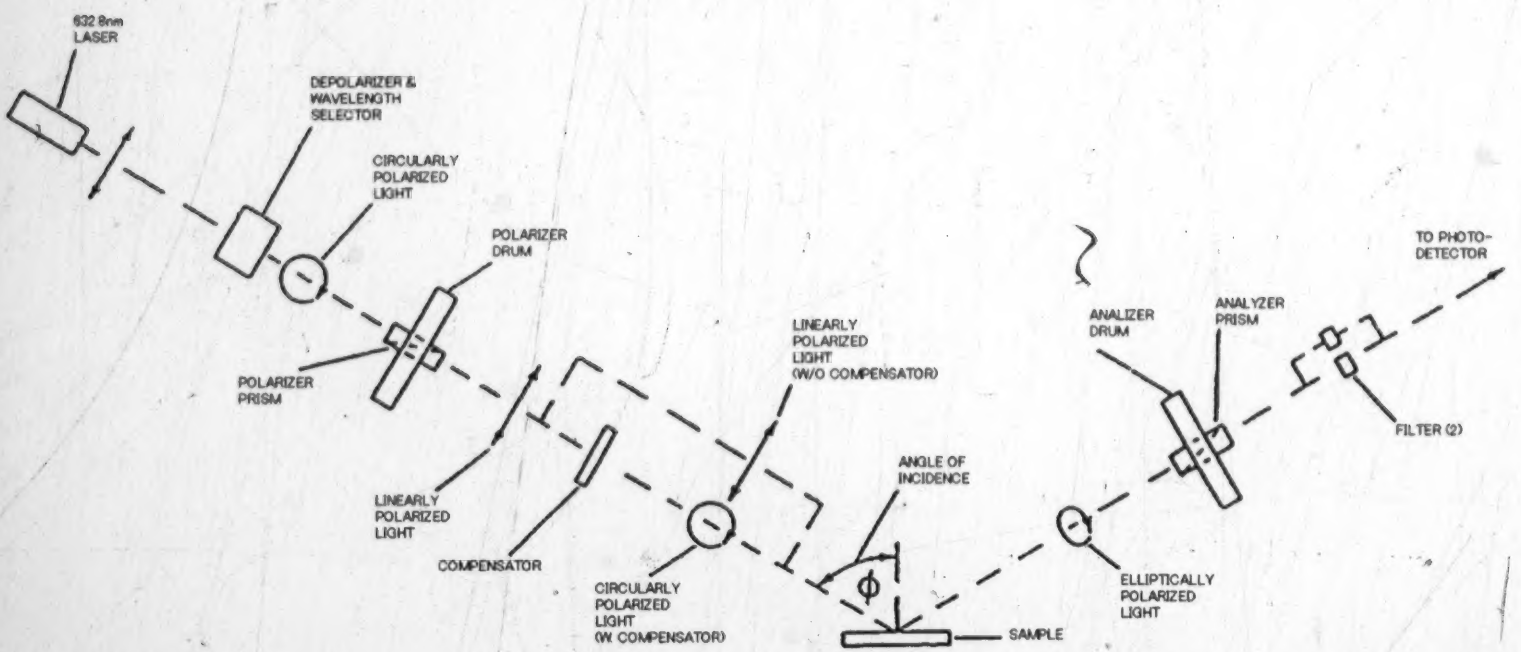

Fig. 22 Schematic of V-shape ellipsometer.

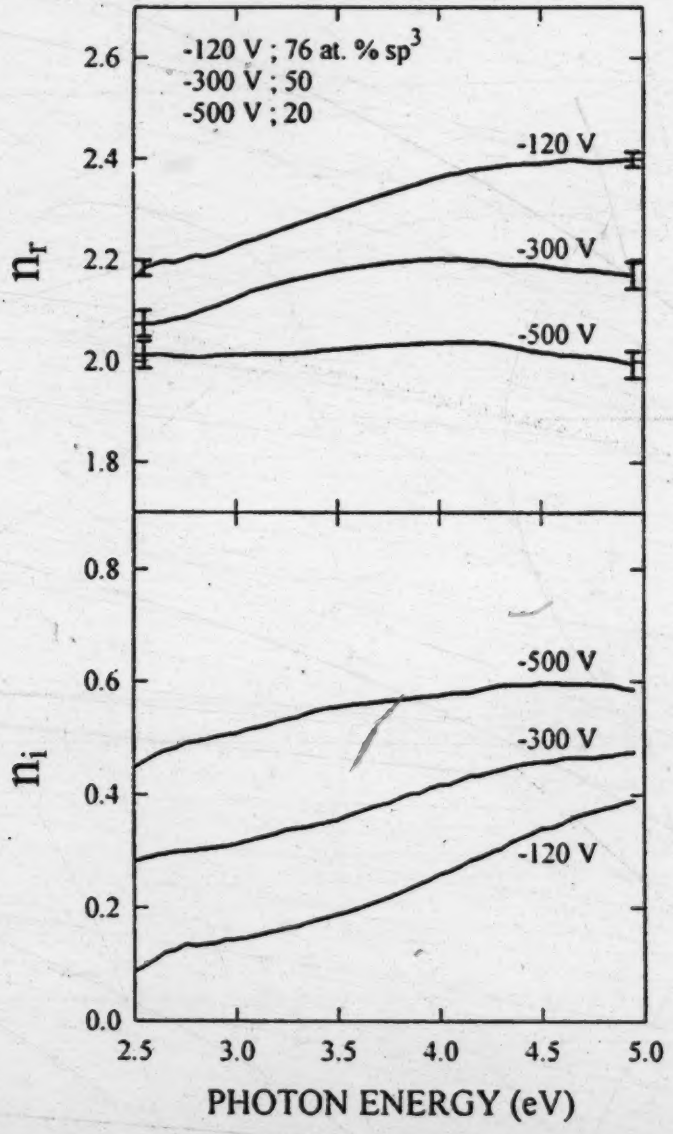

Fig. 23 Selected spectra in the index of refraction n and extinction coefficient n_i, deduced from spectroscopic ellipsometry measurements of a-C prepared using a filtered beam of C^+ ions from a cathodic arc at substrate biases of -120, -300 and -500V, which lead to sp3 contents of 76, 50 and 20 at. % as determined by EELS [60]

II.2.2 Optical Absorption Edge Energy

An important factor for optical protective coating films is that they have sufficient transparency in the region of desired operating wavelength. The optical absorption coefficient α as a function of frequency is given in terms of the optical gap E_g by the Tauc's equation [49]

$$(\alpha h\nu)^{1/2} = k(h\nu - E_g) \qquad (16)$$

where hν is the photon energy and k [$m^{-1/2}J^{-1/2}$] is a proportionality constant. While E_g=3 eV (24,196cm^{-1}) is required for optical transparency through the visible region, hard a-C:H films deposited by Plasma CVD method typically do not satisfy this requirement as can be seen from Fig. 24 [61]. However they do satisfy requirement of transmission in the 4-6μm range for infrared viewing in the atmosphere. Since hard optical coating is a primary application of DLC, good transmission is desired. It is, however, reported that the optical gap can be increased without changing other properties by controlled bombardment by high-energy noble-gas ions (e.g. 1000-eV Ar ions) during film growth [62].

Films of i-C grown by PLD do not fully satisfy this requirement either since the largest reported optical gap is 2.5 eV. However, since i-C contains no hydrogen, i-C exhibits no C-H stretch absorption band and so is more transparent in the infrared than is a-C:H.

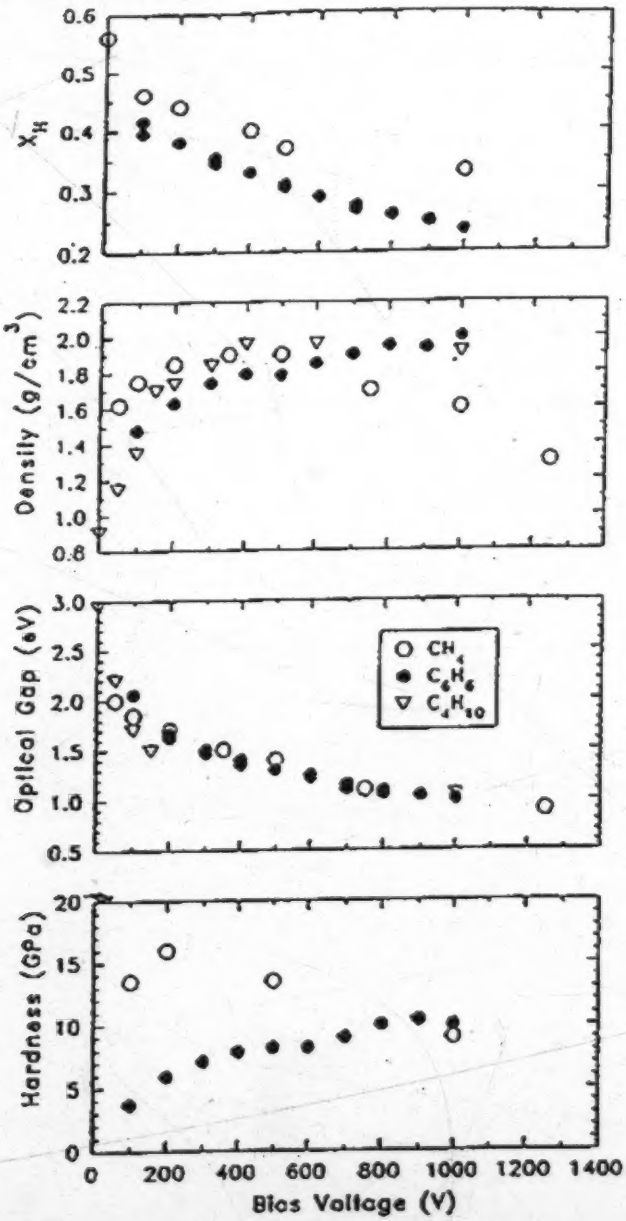

Fig. 24 Key properties (atomic fraction of hydrogen(shown as X_H), density, optical gap, and hardness) of a-C:H deposited by rf plasma CVD as functions of rms self-bias voltage, Vb. Films deposited from three hydrocarbon precursors are compared [61].

II.3 Electrical Properties

II.3.1 Resistivity

Graphite and diamond have very different resistivity, about 10^{15} Ωcm for pure diamond[63] versus 2.5 to $5.0*10^{-4}$ Ωcm and $3*10^{-1}$ Ωcm for graphite along and perpendicular to the hexagonal plane of graphite respectively [5]at 300K. Resistivity is thus a convenient property to check for film quality.

In general, DLC is considered as a composite of very small conducting islands (probably graphite) captured in an insulating matrix (amorphous diamond). Therefore the resistivity may vary significantly due to the grain size of conducting islands. However, it usually has a value of an insulator. Usually the resistivity of a DLC film is measured by depositing the film onto a highly conductive material and measuring conductance across the film thickness since one can easily control the film thickness to the order of a few hundred nanometers which give us measurable resistance with a conventional ohmmeter. When this method is employed, one should be careful about making an ohmic contact between the film and probe. Conductive liquid or paste can be used to make a low resistance contact. Also, the thickness of the film should not be less than a hundred nanometers in order to avoid the tunneling effect [47].

The conventional four point probe system as shown in Fig. 25 is not applicable for an insulating film such as DLC since it is difficult to get any detectable current going through from probe1 to 4 through the film with a typical dimension of a few mm for such apparatus. In addition, for measuring resistivity of the thin film with the four point probe

method, the substrate must have significantly higher resistivity compared with the film material which cannot be assured for the case of DLC film.

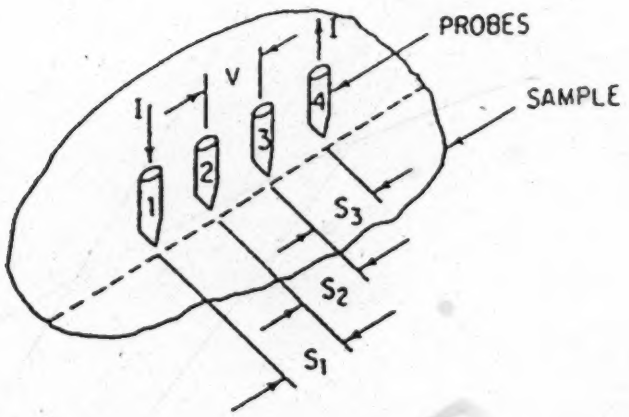

Fig. 25 Schematic of in-line four-point probe. A constant current flows through the film from points 1 to 4 and the voltage across points 2 and 3 is measured [46].

II.4 Chemical Bonding Structure

II.4.1 sp^3/sp^2 ratio

The sp^3/sp^2 bonding ratio is one of the most important properties which determines the quality of the DLC [42]. Raman spectroscopy and Electron Energy Loss Spectroscopy (EELS) are two major techniques used to evaluate the sp^3/sp^2 ratio.

Raman spectroscopy is a probe of the optically active vibration modes of a material. Fig. 26 shows an example of Raman spectra from various carbon materials [1] The sp^3 peak is at 1332 cm^{-1} (called D peak), while the sp^2 peak is at 1550 cm^{-1} (called G peak).

Although Raman spectroscopy is a very powerful tool to examine DLC structure, it is sometimes difficult to measure the exact peak intensity of the D peak because the Raman spectra of DLC is dominated by G mode signal due to its much higher Raman scattering cross-section (30~60 times that of D mode).

EELS is a very convenient and powerful tool to examine DLC. Different from Raman Spectroscopy, EELS measures loss of kinetic energy of electrons passing through very thin samples of material. Lost energy is used for exciting electrons from the 1s state to the higher states. With sufficiently high input beam energy (10 to 20 KeV), one can observe orbital transition energies of the components of the material of the films. For carbon the π peak appears at 285 eV while the σ peak shows a broad peak around 290 eV up to 400eV. Fig. 27 shows EELS spectra from graphite, diamond, and DLC's made by different methods [64,65] Since the signal strengths of π and σ peaks are similar, one can observe the sp^3/sp^2 ratio more easily with EELS than with Raman spectroscopy.

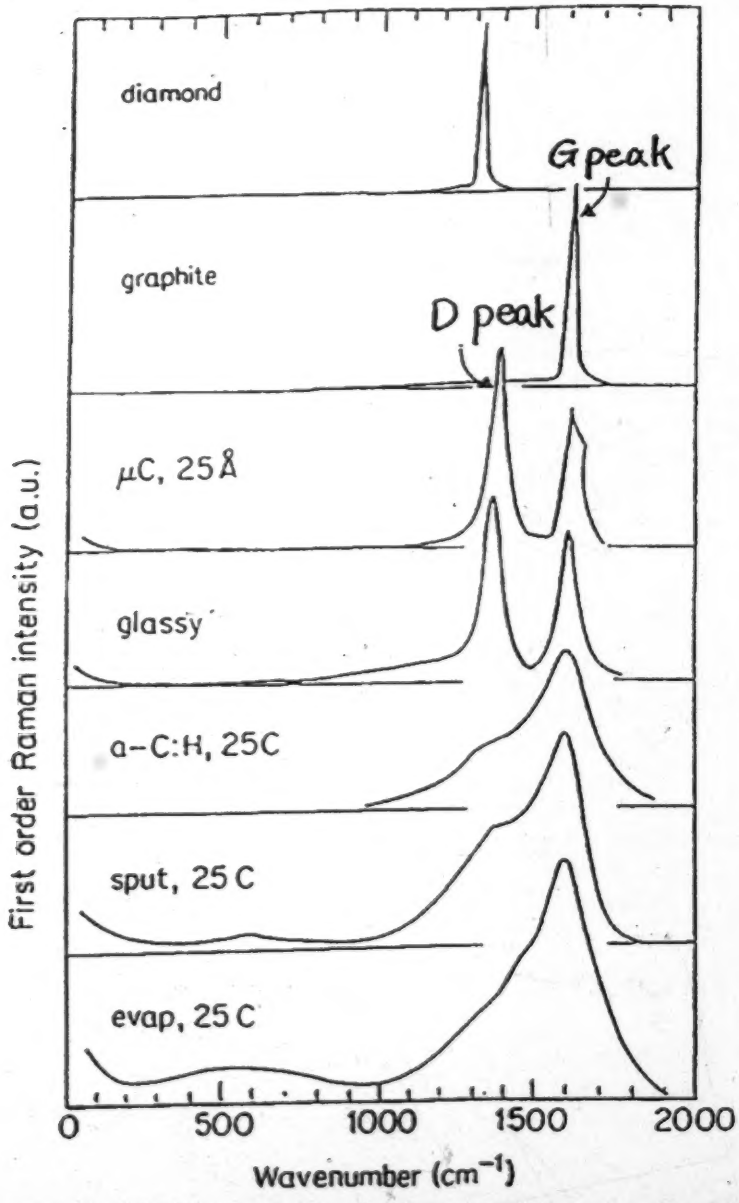

Fig. 26 An example of the Raman spectra of carbon materials made using different techniques. The G peak (1580cm^{-1}) and the D peak (1350cm^{-1}) are the signatures of the sp^2 and the sp^3, respectively [1]. (Note: the D peak in fact has the different wavenumber from that of the pure diamond peak (1332cm^{-1}), but it still can be used as the signature of the sp^3.)

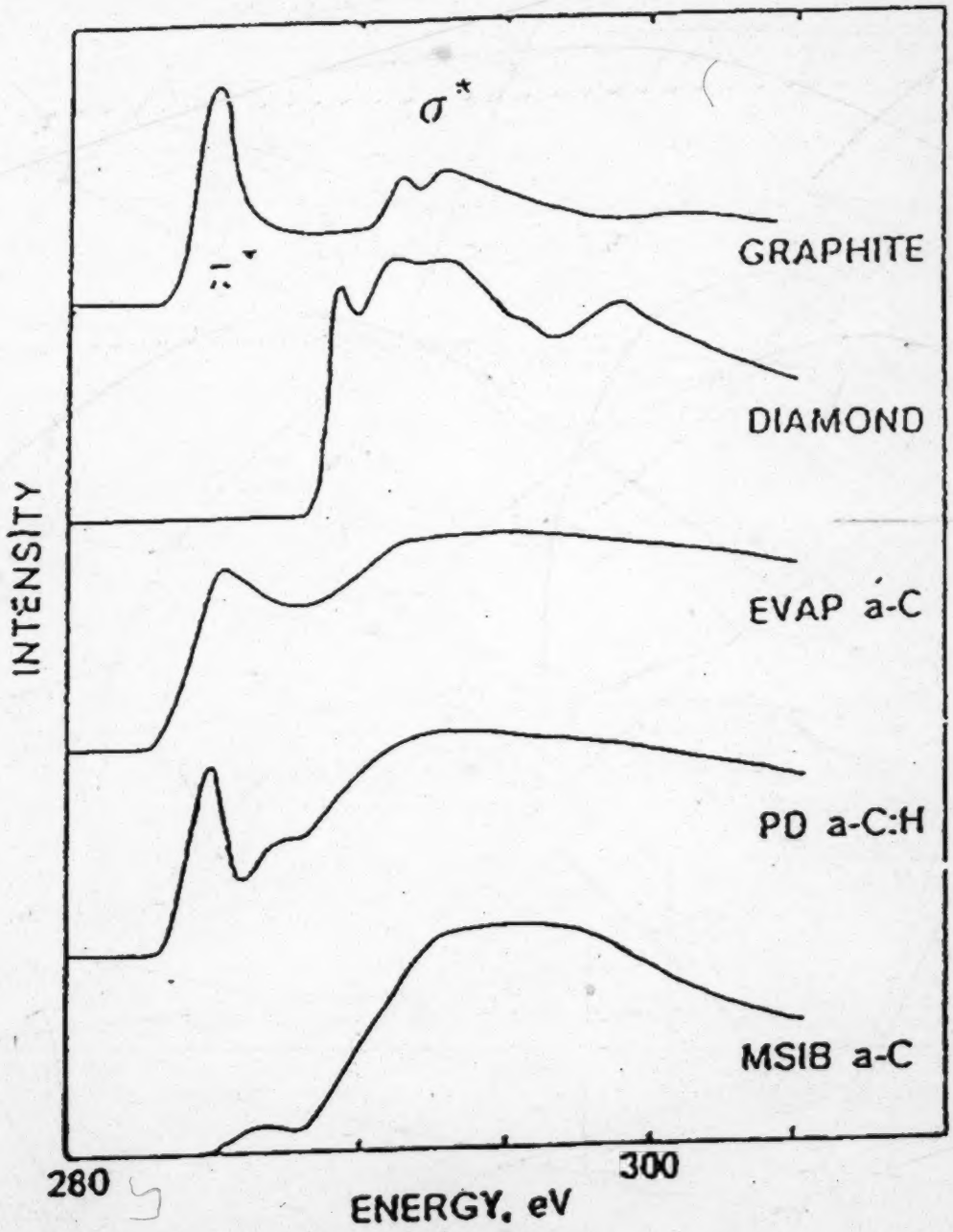

Fig. 27 An example of the EELS spectra of carbon materials. From the π peak one can observe how much sp^2 bonding there is in the sample. The sp^3 fraction of MSIB a-C and evaporated a-C is 85% and 8%, respectively [64,65].

III Development of a SAW Detection System for Film Characterization

III.1 Introduction

A laser acoustic technique for characterization of the Young's modulus of thin films, which is generally related to the hardness, based on the measurement of dispersion of a surface acoustic wave (SAW) has been developed. The film characterization technique involves irradiation of the sample with a laser pulse focussed to a short narrow line which excites a surface acoustic wave in the sample. The dispersion of the surface acoustic wave is measured at various distances from the excitation region using a knife-edge piezoelectric detector. From the dispersion as a function of frequency various characteristics of the film can be determined such as thickness, density and Young's modulus. Initial development and testing of this technique on a gold film has been carried out.

III.1.1 Rayleigh wave

Surface Acoustic Waves (SAWs), also known as Rayleigh waves, are a mode of elastic energy propagation which can only exist near the surface of a solid whose thickness is much greater than the wavelengths of the acoustic wave. The amplitude of the waves decay exponentially with depth and become negligible within a few wavelength of the surface. In fact, usually more than 90% of wave energy is concentrated within one wavelength of surface, and as a result the wave properties, such as velocity,

attenuation factor, etc., depend primarily on the elastic properties near the surface of the medium. Therefore, Surface Acoustic Waves (SAWs) are a useful tool for studying the surface of a solid medium.

Rayleigh waves are named after Lord Rayleigh, who found a solution of the wave equation in the isotropic half-space, and they are elliptically polarized in the sagittal plane (i.e. the plane perpendicular to the surface and parallel to the direction of propagation) [66].

The Rayleigh wave has a constant velocity of slightly less than that of the shear (transverse) wave when it appears on the surface of a bulk material. The Rayleigh wave velocity is approximately given as [66]

$$V_R \approx V_T \frac{0.72-(V_T/V_L)^2}{0.75-(V_T/V_L)^2}, \tag{17}$$

where V_T and V_L are the velocities of the transverse and longitudinal wave respectively, which are given by

$$V_T = \sqrt{\frac{E}{2\rho(1+\nu)}} \tag{18}$$

$$V_L = \sqrt{\frac{E}{\rho}\frac{1-\nu}{(1+\nu)(1-2\nu)}} \tag{19}$$

where E, ρ and ν are Young's modulus, density and Poisson's ratio respectively.

The exact velocities can be found by numerically solving the equation given as[67]

$$\left[2-\left(\frac{V_R}{V_T}\right)^2\right]^2 = 4\left[1-\left(\frac{V_R}{V_L}\right)^2\right]^{1/2}\left[1-\left(\frac{V_R}{V_T}\right)^2\right]^{1/2} \tag{20}$$

III.1.2 Dispersion

Although the surface acoustic wave has a fixed velocity for a given material, a velocity dispersion may arise when it propagates in a thin layer on top of the surface of a bulk material. Low frequencies propagate primarily in the substrate with the group and phase velocity of the substrate and high frequencies propagate more in the thin film layer and the group and phase velocities are pulled towards the values of the film as the frequency increases (Fig. 28). Since the shape of dispersion curve depends on the film thickness and thus the elastic and physical constants of both film and substrate, it is possible to study film characteristics by fitting theoretical curves to the measured dispersion curve of phase velocity versus frequency.

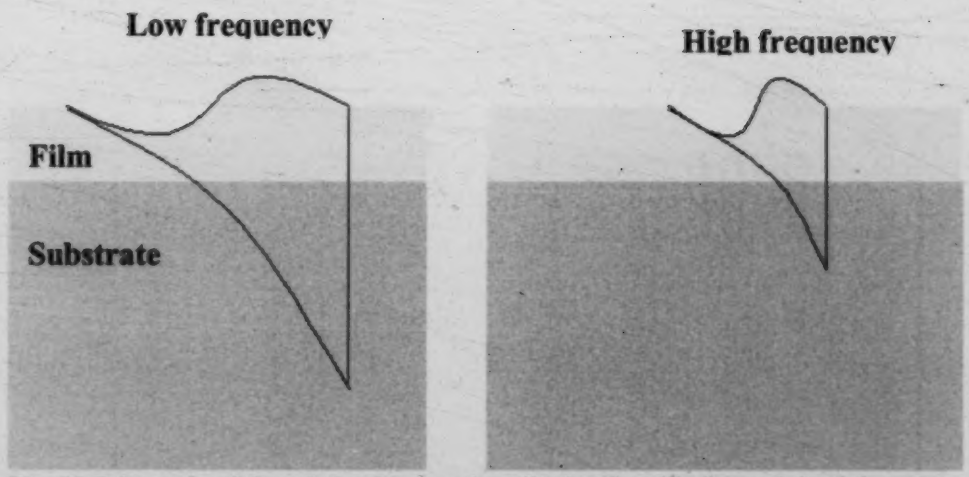

Fig. 28 Schematic of the relation between amplitude of oscillation and depth into the substrate for low frequency versus high frequency waves. When a film is present on a substrate, higher frequencies (i.e. shorter wavelengths) are more likely to be affected by the elastic properties of the film than lower frequencies which penetrate well into the substrate.

By taking into account the ten boundary conditions between the film and substrate and film and air, for an isotropic film on an isotropic substrate, a matrix governing propagation of SAW is given by [66]

Equation (21)

$$M = \begin{bmatrix} b^{(s)} & -1 & -b^{(s)} & -1 & -b^{(c)} & 1 \\ -1 & -b^{(e)} & -1 & b^{(e)} & 1 & b^{(d)} \\ 1-b^{(s)2} & 2b^{(e)} & 1-b^{(s)2} & -2b^{(e)} & -r\left(1-b^{(c)2}\right) & -2rb^{(d)} \\ 2b^{(s)} & -\left(1-2b^{(s)2}\right) & -2b^{(s)} & -\left(1-b^{(s)2}\right) & -2rb^{(c)} & r\left(1-b^{(c)2}\right) \\ \left(1-b^{(s)2}\right)\exp\left(ikb^{(s)}h\right) & 2b^{(e)}\exp\left(ikb^{(e)}h\right) & \left(1-b^{(s)2}\right)\exp\left(-ikb^{(s)}h\right) & -2b^{(e)}\exp\left(-ikb^{(e)}h\right) & 0 & 0 \\ 2b^{(s)}\exp\left(ikb^{(s)}h\right) & -\left(1-b^{(s)2}\right)\exp\left(ikb^{(e)}h\right) & -2b^{(s)}\exp\left(-ikb^{(s)}h\right) & -\left(1-b^{(s)}\right)\exp\left(-ikb^{(e)}h\right) & 0 & 0 \end{bmatrix}$$

where;

$$b^{(s)} = +i\sqrt{1-(V/V_T)^2}, \qquad b^{(e)} = +i\sqrt{1-(V/V_L)^2}$$

$$b^{(c)} = +i\sqrt{1-(V/v_T)^2}, \qquad b^{(d)} = +i\sqrt{1-(V/v_L)^2}$$

$$r = \frac{\rho_{sub}}{\rho_{lay}}, \qquad k = \frac{2\pi f}{V}$$

h= Film Thickness

f= Frequency of SAW

V_T= Transverse wave velocity in layer material

V_L= Longitudinal wave velocity in layer material

v_T= Transverse wave velocity in substrate material

v_L= Longitudinal wave velocity in substrate material

Solutions for the allowed SAW phase velocities for a given frequency are found by setting the determinant of the matrix to zero

$$\det(M(V))=0. \qquad (22)$$

The roots are found numerically by varying V (phase velocity) and finding the values which satisfy the equation.

When the phase velocity in the surface film material is lower than in the substrate (called loading), guided modes can appear leading to multimode propagation at high frequencies (typically >150 MHz). In this case, the maximum velocity of the 1st order mode is the Rayleigh wave velocity for the substrate material at zero frequency and the minimum velocity is the Rayleigh wave velocity for the layer material as shown in Fig. 29 [66]. On the other hand, when the phase velocity in the surface film material is higher than in the substrate (called stiffening), only one mode exists which has the Rayleigh wave velocity of the substrate material as a minimum value of phase velocity at zero frequency and the Transverse wave velocity of the substrate material as the maximum value at infinite frequency as shown in Fig. 30 [66].

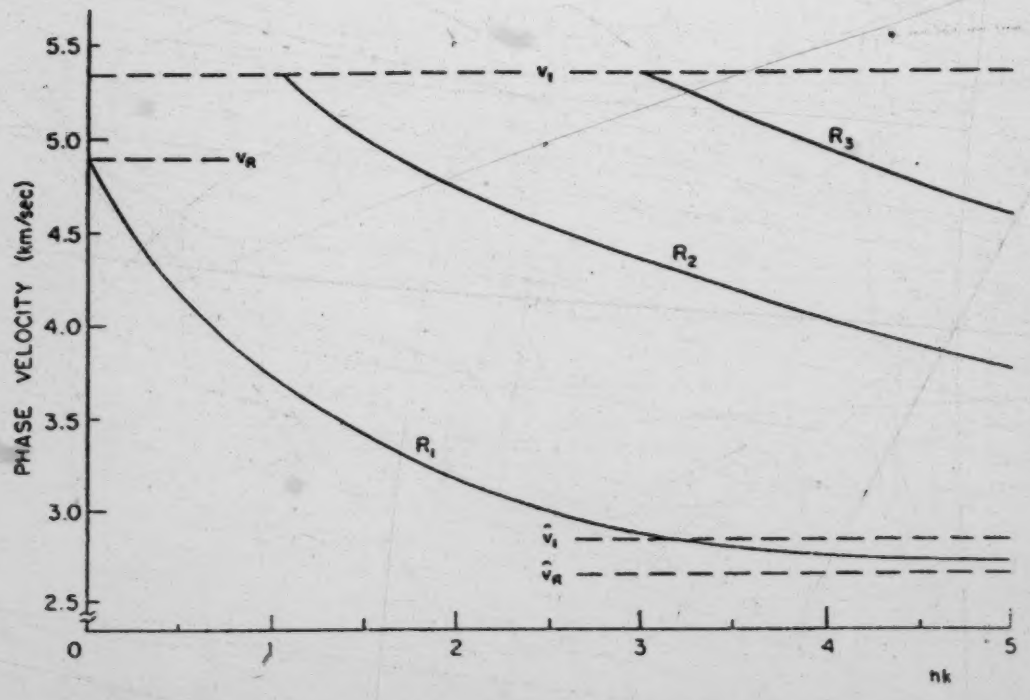

Fig. 29 Phase velocity of the first three Rayleigh modes; ZnO layer on siLicon assuming isotropic parameters [66]. v_T is transverse wave velocity in the substrate material, v_R is the Rayleigh wave velocity in the substrate material, V_T is transverse wave velocity in the layer material and V_R is the Rayleigh wave velocity in the layer material.

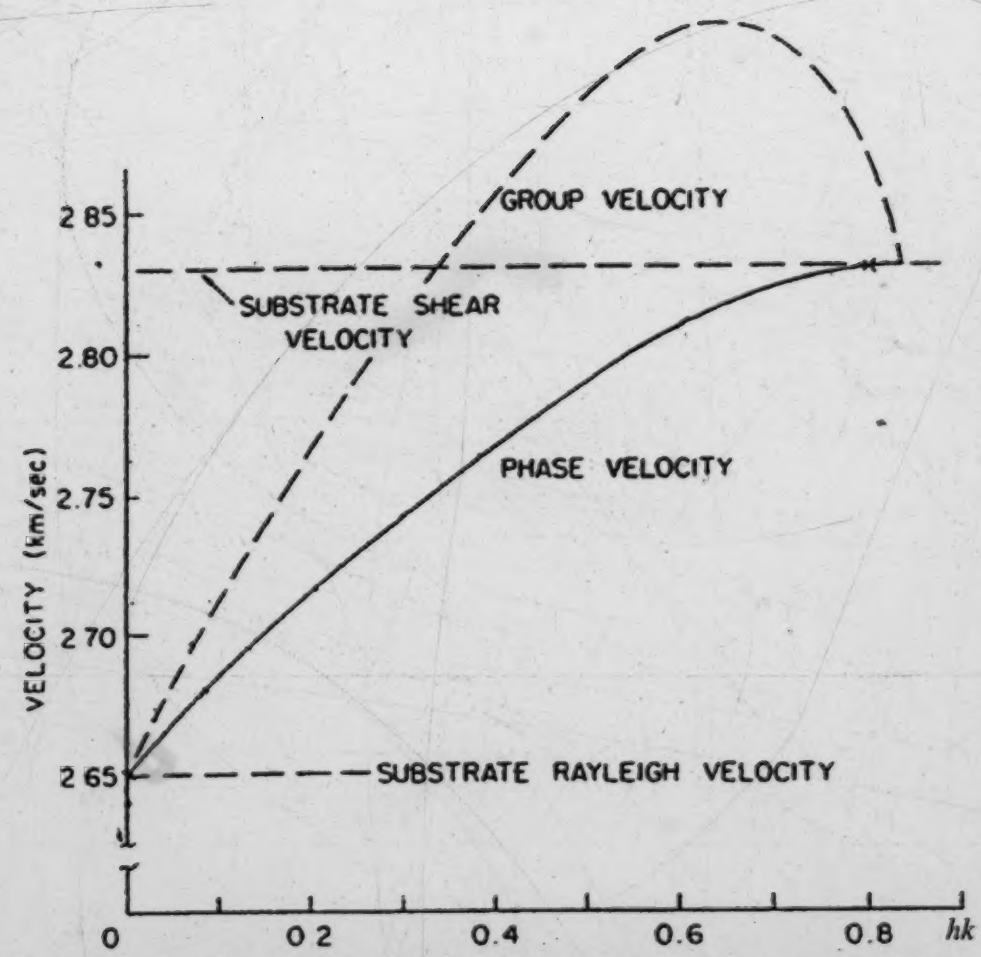

Fig. 30 Phase and group velocity of a silicon layer on a ZnO substrate with respect to the product of the film thickness h and wavenumber.k, assuming isotropic parameters and layer shear velocity is larger than that of the substrate [66].

III.1.3 Pulsed Laser Excitation of SAW

When an elastic medium is heated transiently, first the heated region expands and then shrinks by escape of the thermal energy from the heated region. This heating and cooling process is employed for the Pulsed Laser Excitation of SAWs. When a laser is employed to create a high temperature region in materials in order to generate acoustic waves, one must find an optimal spot size / linewidth which gives minimum interference between elementary radiators created in the different points in the excitation spot as shown in the inset in Fig. 31 [69]. The optimal spot size irradiated by monochromatic lasers is given by Krylov et al [68] as

$$k_R = \sqrt{2}/a, \tag{23}$$

where k_R is wavenumber of Rayleigh wave and a is radius of laser spot or width of the line. However, this condition usually can hold only for continuous wave lasers. Pulsed lasers usually excite a wide spectrum and cannot be considered as monochromatic. Fortunately, an additional condition for the case of pulsed laser irradiation has been found by Arnold et al as [69]

$$\omega_R = \frac{1}{\sqrt{2}\tau}, \tag{24}$$

where ω_R is a peak angular frequency of Rayleigh wave generated by a Gaussian shape laser pulse with the time duration of τ. By combining this condition with the previously given condition by using the relation $\omega_R = v_R k_R$, we obtain

$$a = \frac{v_R \tau}{2}. \tag{25}$$

Experimental data shown in Fig. 31 agrees with this theory [69] Waveforms with different spot sizes are shown in Fig. 32 [69]

If these conditions are not satisfied, interference between elementary radiators given by the above spot size becomes significant and subdivides the surface area exposed under laser irradiation into several coherent regions and thus decreases the energy of the Rayleigh wave.

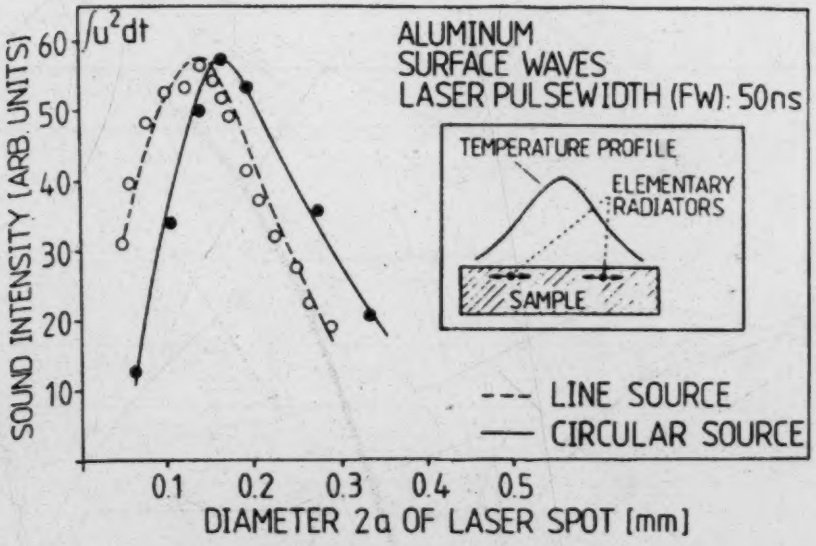

Fig. 31 Surface wave intensity as a function of laser-spot diameter. There is a pronounced maximum which occurs when $a=V_R\tau$ [here $V_R=2.0*10^3$ m/s,τ=25ns,2a=0.16mm(+/-10%)]. The insert shows schematically that each radial component contributes to the measured signal Note that there is also a temperature gradient normal to the surface contributing to SAW generation because this type of wave contains longitudinal as well as transverse components [69].

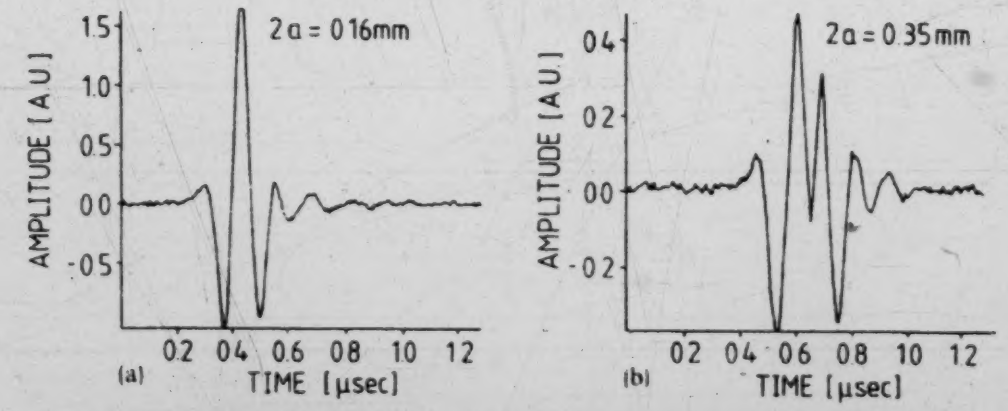

Fig. 32 Received SAW signals for two different laser-spot diameters: (a) There is a well-defined pulse shape if $a=V_R\tau$ is satisfied: (b) For all other diameters the pulse form becomes increasingly modulated [69].

III.1.4 Energy directionality of SAW generated from a line source

When we consider the angular distribution of surface acoustic waves generated from a line source, we should consider the line source as an antenna. Since the penetration depth is much smaller than the length of the line, we could regard our line source as a one-dimensional antenna placed on a plane.

In a one dimensional antenna, first one should consider a distribution of displacement across the aperture caused by the lateral temperature gradient. At the point x at time t this can be written as $F(x)\cos[\omega t - \phi(x)]$, where ω is the angular frequency of the (monochromatic) oscillation and $F(x)$ and $\phi(x)$ are the amplitude and phase, respectively [70]. The amplitude phasor $E(x)$, is the complex quantity given by

$$E(x)=F(x)\exp(-i\phi(x)), \qquad (26)$$

which can be employed wherever displacement fields are dealt with below. We note that the instantaneous field is given by the real part of $E(x)\exp(i\omega t)$

that is,

$$F(x)\cos[\omega t - \phi(x)]=Re[E(x)\exp(i\omega t)]. \qquad (27)$$

By Huygens' principle, the field produced at a distant point will be the sum of the effects of the point elements within the aperture. Each element produces an effect proportional in amplitude to the field at the element and retarded in phase by the number of cycles contained in the path to the distant point. Thus at a distance r the field due to the element between x and x + dx is proportional to

$$E(x)dx\exp(-i2\pi r/\lambda), \qquad (28)$$

where λ is the wavelength.

Consider the field at a distant point P in a direction making an angle θ with the z axis as shown in Fig. 33 [70]. Let the point P be at a distance R from the origin x=0, z=0. Then for large distances from the source (the far field region) r is given approximately by,

$$r = R + x\sin\theta = R + xs \tag{29}$$

where $s = \sin\theta$

Giving

$$E(x)\exp(-i2\pi r/\lambda)dx = E(x)\exp(-i2\pi R/\lambda)\exp(-i2\pi xs/\lambda)\,dx. \tag{30}$$

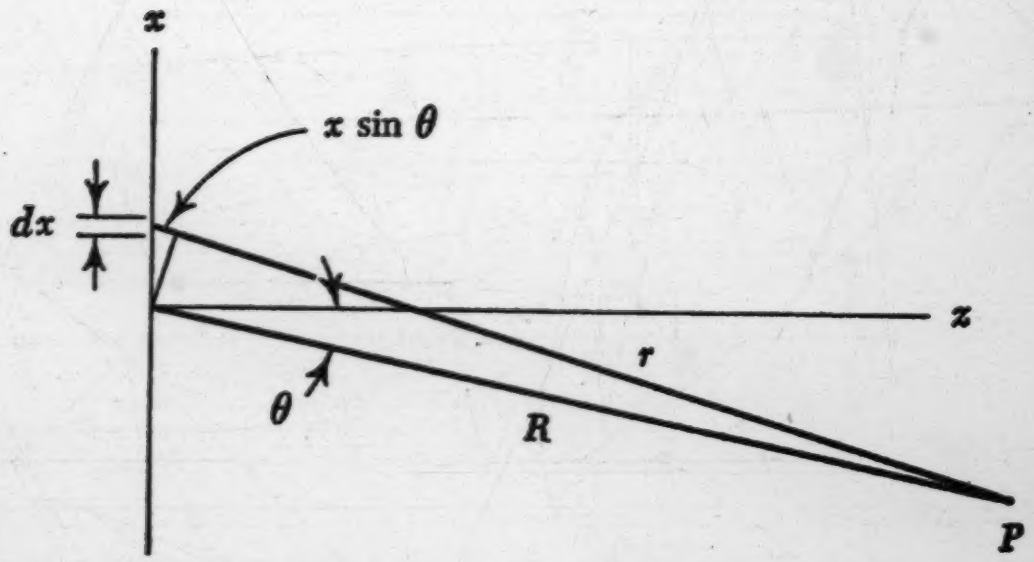

Fig. 33 Construction used in applying Huygens' principle.

Let the factor $\exp(-i2\pi R/\lambda)$, which expresses the average phase retardation at a distance R, be lumped in with the amplitude phasor. Then, integrating along the line radiator, we find that the distant field, in the direction s, is given by

$$\int_{-\infty}^{\infty} E(x)e^{-i2\pi xs/\lambda}dx \tag{31}$$

The distant field, as a function of direction, is thus seen to be related to the aperture field distribution through the Fourier transformation. To throw the basic relation into the standard form, we henceforth measure distances in the aperture plane in terms of the wavelength; that is , we deal in x/λ instead of x. We then define $E(x/\lambda)$ to be equal to the old $E(x)$ and introduce $P(s)$ such that

$$P(s) = \int_{-\infty}^{\infty} E\left(\frac{x}{\lambda}\right) e^{-i2\pi(x/\lambda)s} d\left(\frac{x}{\lambda}\right) \tag{32}$$

The quantity P(s), which is proportional to the distant field produced in the direction s, is known as the field radiation pattern or angular spectrum. Usually it is normalized in some way, but as we have introduced it, it depends not only on the character of the aperture excitation $E(x)$ but also on the level of excitation. When normalized, it is characteristic of the antenna alone, irrespective of the strength of the energy source.

By the reciprocal property of the Fourier transformation, it then follows that

$$E\left(\frac{x}{\lambda}\right) = \int_{-\infty}^{\infty} P(s) e^{-i2\pi(x/\lambda)s} ds. \tag{33}$$

Since s is the sine of an angle, the meaning of an integral taken between infinite limits of s may be obscure. However, the restriction to high directivity ensures that the integrand falls to zero while s is still well defined.

As an example consider an aperture for which

$$E\left(\frac{x}{\lambda}\right) = \Pi\left(\frac{x/\lambda}{w}\right) \tag{34}$$

where $\Pi(y)$ is a unit square function, that is , a uniform field maintained over a distance of w wavelengths outside of which the field is zero. Then

$$P(s) = \text{sinc}(ws) = \frac{\sin\left(\pi l \nu / V_R \sin\theta\right)}{\pi l \nu / V_R \sin\theta} \tag{35}.$$

where

l =length of the line source

ν=frequency of the wave

V_R= velocity of the Rayleigh wave for given frequency

This relation is illustrated in Fig. 34 [70].

Fig. 35 shows frequency dependence of directionality of the SAW amplitude for 4mm line source at 3MHz where V_R=2906m/s. It shows that the higher the frequency, the more the radiation is oriented normal to the line source.

Fig. 36 shows the surface displacement waveforms of aluminum sample (3"x3"x1") detected 15mm away from the center of the line source created by YAG laser irradiation at various angles [71]. At the higher angles, the pulse signal becomes smaller and broader meaning that there is a lack of high frequency components which is consistent with the result shown in Fig. 35.

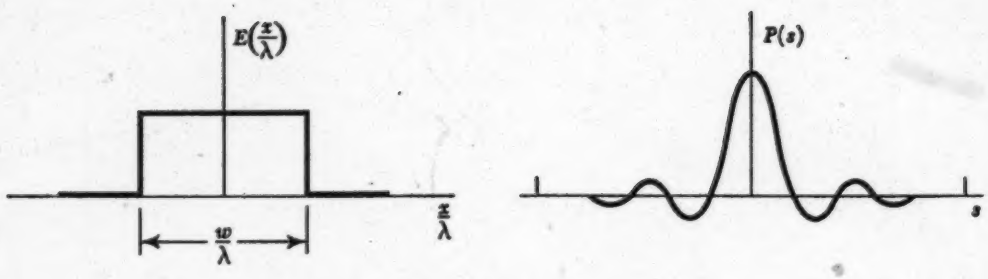

Fig. 34 An aperture distribution and its angular spectrum.

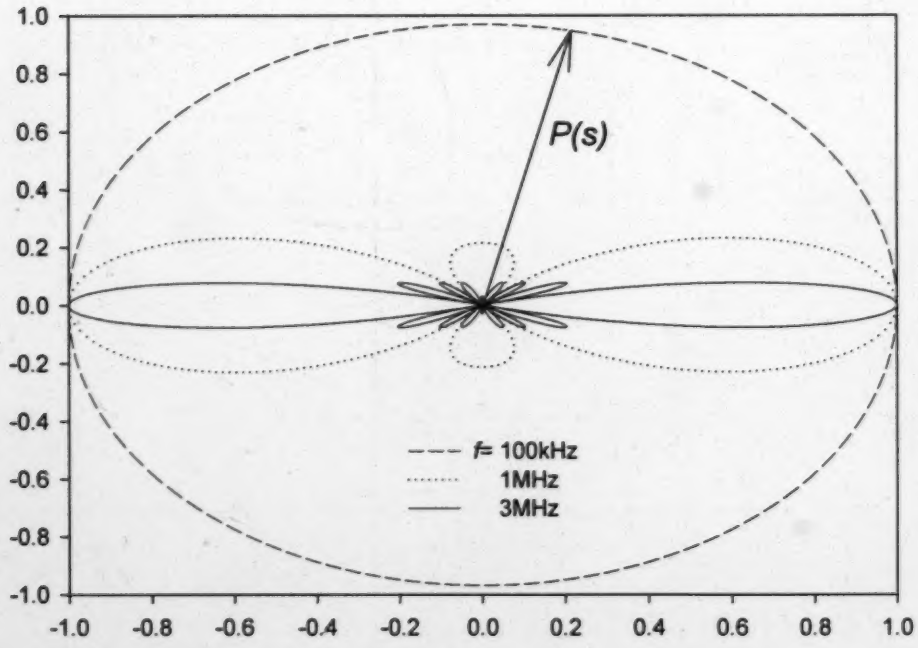

Fig. 35 Angular distribution of the amplitude of surface acoustic waves with different frequencies generated from a 4mm line source on an aluminum sample. The line radiator is oriented along the vertical direction.

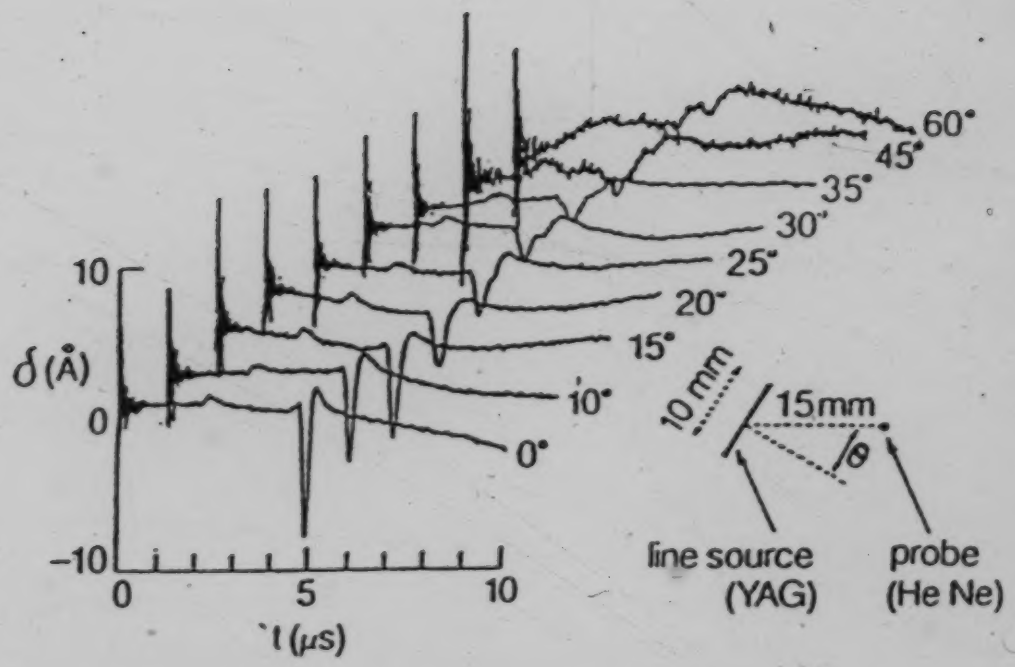

Fig. 36 Displacement waveforms produced by the thermoelastic line source in various directions. Last three signals are expanded vertically by a factor of 2 [71].

III.2 System Development

A SAW detection system has been developed as part of this thesis research. Fig. 37 shows a schematic diagram of the setup. A pulse of KrF excimer laser radiation (wavelength=248nm, FWHM=15ns) passes through the cylindrical lens and is focused onto the surface of the sample to be studied in order to create a line heat source in a short period of time. A transient surface acoustic wave is created due to the rapid heating and subsequent cooling of the focal spot region and mainly propagates along the direction perpendicular to the line source. The size of the focal spot has a length of 20mm and width of the 20 to 30 micrometers. Fine adjustment of the focus was carried out for each material in order to obtain the maximum energy conversion to the surface acoustic wave. The input energy was controlled by tilting a zero degree 100% reflection mirror in the beam path to allow a small amount of transmission and was maintained below 1mJ for creating only thermal expansion on the surface. This was increased up to 10mJ for ablation excitation when desired. A piezoelectric film (polyvinyldifluoride (PVDF)) wrapped around a knife-edge which is placed onto the sample detects the vertical displacement of the surface of the sample at a distance from the excitation source as the SAW pulse travels under the contact area as shown in Fig. 38. The transient displacement is converted into a voltage which has a peak amplitude of a few microvolts when displacement is created by thermal expansion and a few hundred microvolts for the case of laser ablation. The knife-edge must be placed parallel to the line source in order to obtain the high frequency components. The voltage is then amplified by 3 stages of broadband amplification with a total gain of 50db. After the signal is amplified, it is measured using a Tektronics TDS380 (400MHz, 2Gs/sec) oscilloscope. Measurements

are taken at two different distances between the line source and knife-edge. The distance between the line source and knife-edge is precisely controlled by a translation stage with the help of a micrometer. Two waveforms recorded at two different distances are then analyzed in order to obtain a dispersion curve as describe in III.5. Fig. 39 shows a picture of the SAW detection system developed at the University of Alberta.

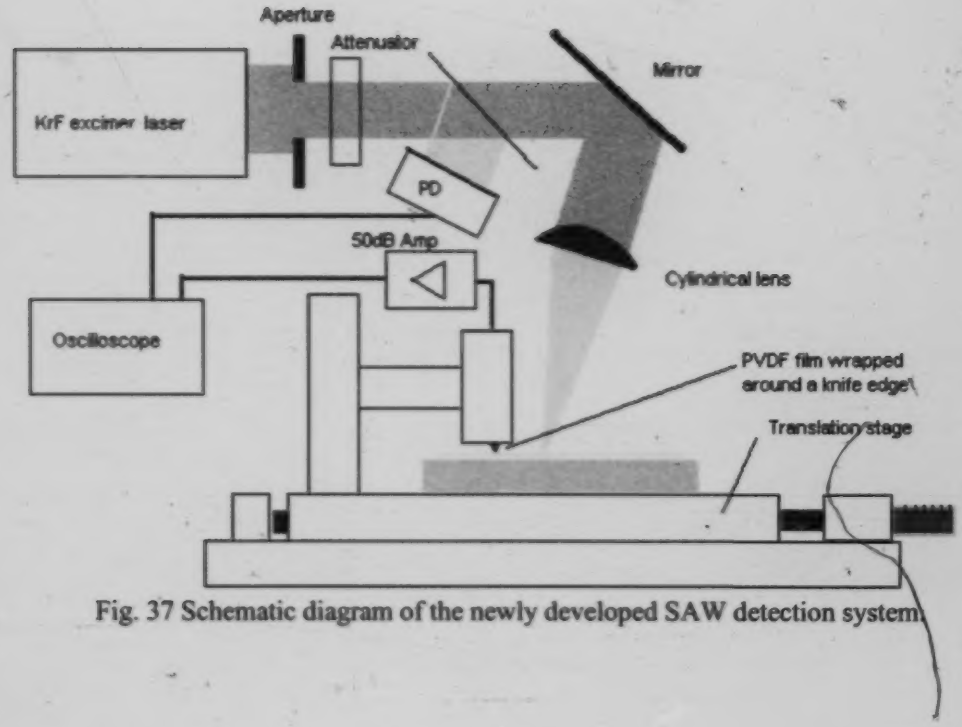

Fig. 37 Schematic diagram of the newly developed SAW detection system

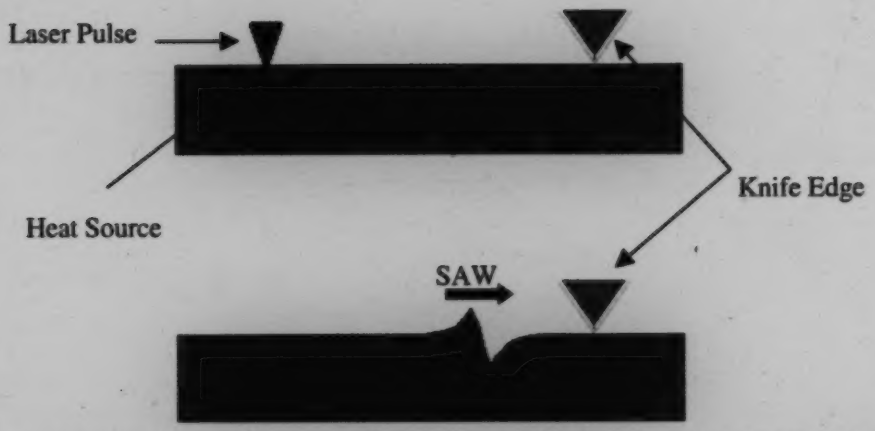

Fig. 1 A piezoelectric film wrapped around the knife-edge detects the SAW induced by the laser heating/ablation process. The laser line focus is parallel to the knife-edge.

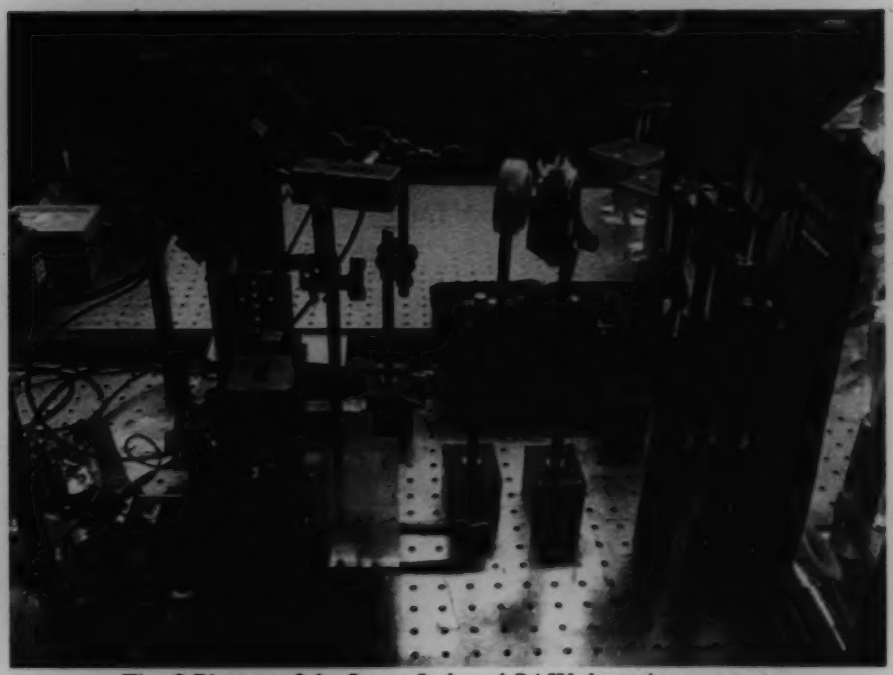

Fig. 2 Picture of the Laser Induced SAW detection system.

III.2.1 Knife-edge

Fig. 40 shows the picture of the broadband SAW transducer. The design was developed from the one proposed by Coufal et al [72] shown in Fig. 41. Tungsten was selected for the knife-edge material because of its high specific acoustic impedance and its hardness which allows us to sharpen the edge with a radius of the curvature on the order of a few microns. Fig. 42 shows the magnified image of the knife-edge. From the picture we found the radius of curvature of the knife-edge less than 2μm. The length of the knife-edge is approximately 12mm. The rod with the knife-edge on it is insulated from the aluminum housing by Teflon Insulation.

Fig. 40 Picture of broadband SAW transducer. A slot is made in order to allow the laser pulse to approach close to the knife-edge

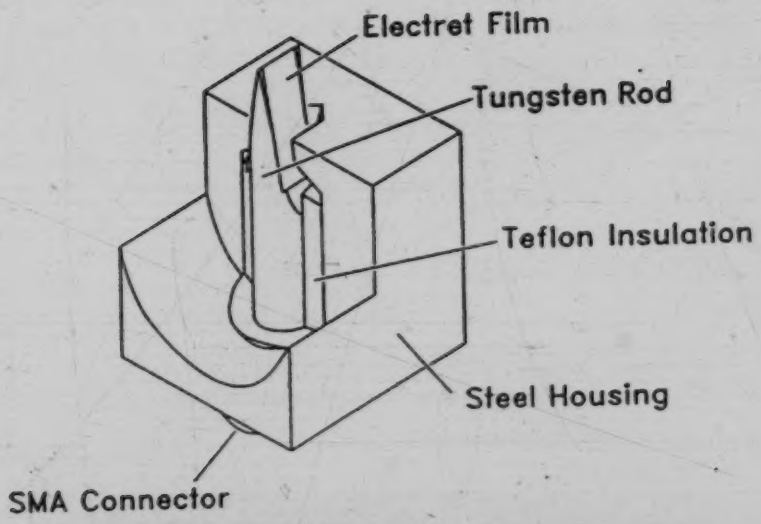

Fig. 41 Schematic of the SAW transducer proposed by Coufal et al [72].

Fig. 42. Image of the top of the knife-edge.

III.2.2 Piezoelectric Film

Polyvinyldifluoride (PVDF) film was selected as the piezoelectric film material which has wrapped around the knife-edge. The thickness of the film is about 9 micron and it is coated on both sides with10 nm thickness of silver film as purchased. To mount on the detector the film was first cut into pieces 18mm by 11.5 mm in size. Then we etched away one side of the metal film and placed the etched side against the knife-edge. When the film was wrapped around the knife-edge, a very tiny amount of silicon based vacuum oil was used to give good mechanical contact between the film and tungsten knife-edge. The reason for doing this is to insulate the PVDF film and the Tungsten rod except at the region where the film is making contact with the top of the knife-edge. This process gives a better frequency response as well as larger signal amplitude. The remaining silver coating on the outside of the film is in contact with the outside metal case in order to ground the outer surface of the PVDF film. This is necessary to detect the voltage difference between inner and outer surfaces of the PVDF film.

III.2.3 Amplifier

We used 2 stages of Minicircuits MAR-6SM amplifiers [73] which have a bandpass of 0.3MHz to 2GHz and typical gain of 20dB for each stage and 1 stage of Minicircuits MAR-8SM which has a bandpass of 0.3MHz~1GHz and typical gain of 10dB. The length of connecting wires whose characteristic impedance is not 50 ohms was minimized in order to reduce reflection and ringing. Also, in order to avoid the deviation from the specified value of each of the electrical components in the frequency region

beyond 100MHz, we employed carbon based resistors (not metal film resistors) for resistance, ceramic capacitors (not dielectric film based capacitors) for capacitance, and coils made on the ferrite tori as filters on the supply voltage lines.

III.3 Noise Reduction

Various efforts have been made in order to reduce electrical noise picked up by the SAW detector circuit which mainly originates from the electrical discharge pumping of the KrF laser.

Firstly, we minimized the internal noise of the amplifier by reducing oscillation and feedback as discussed in III.2.3. Secondly, the whole SAW detection system was placed into a Faraday cage in order to reduce the effect of electromagnetic radiation from the excimer laser and other RF noise such as FM radio stations. Thirdly, a metal strip was directly connected from the Faraday cage ground (optical table) to a high speed aluminum ground bus which is run down to stakes in the ground outside the building. Fig. 43 shows the comparison of the signal before and after the installation of the fast grounding line to the detector housing. It was always difficult to reduce the noise of the FM radio transmissions, especially, that of the campus radio station since the distance between the transmission antennae and the detector was approximately 100m. The average of a number of signals was taken for further noise reduction.

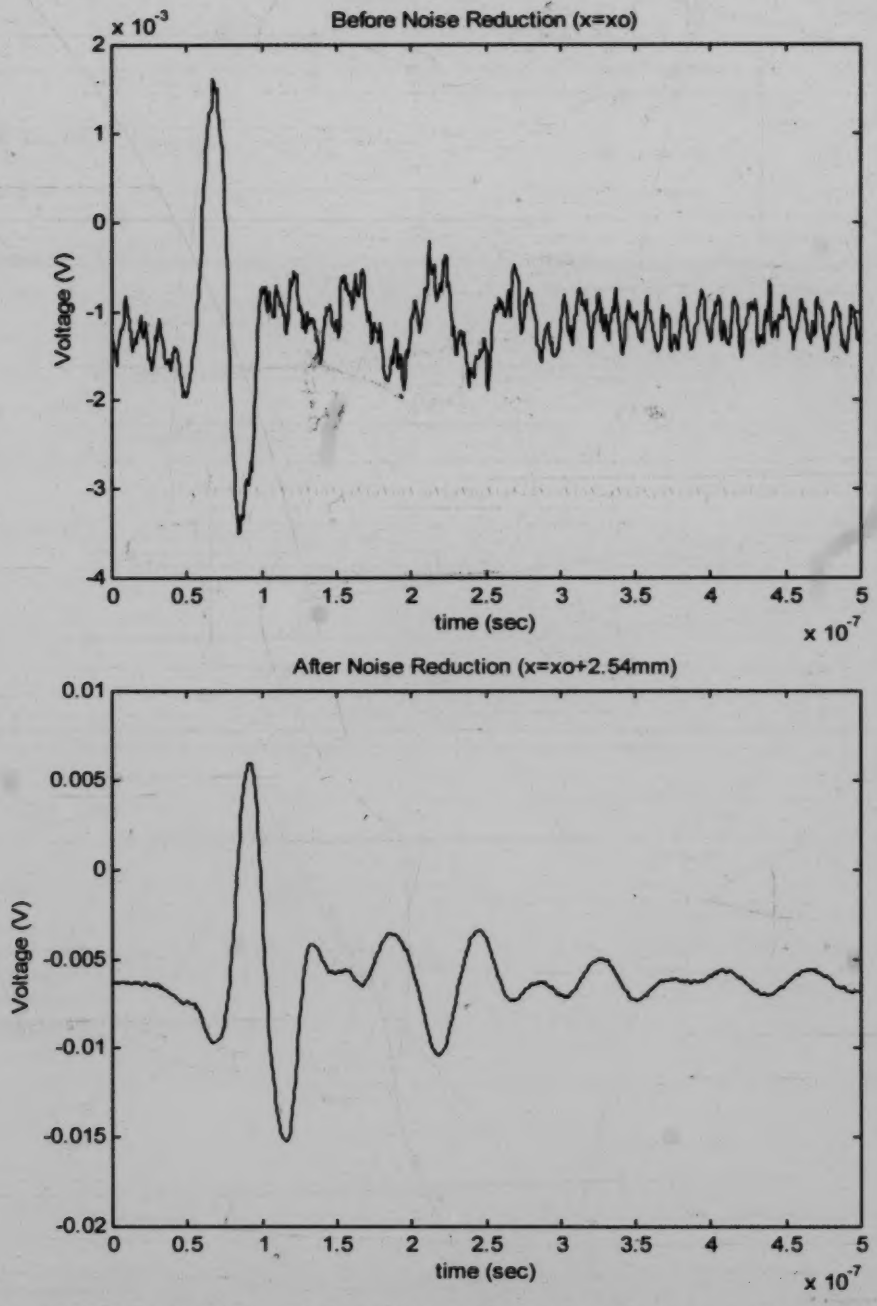

Fig. 43 Noise reduction by the installation of a low inductance grounding metal strip to the aluminum housing of the broadband SAW transducer. Each SAW signal is the average of 256 waveforms measured on BK7.

III.4 Signal Detection

Various measurements have been conducted to study the influence of a number of parameters on the laser induced SAW.

III.4.1 Effect of the Contact Pressure of PVDF Film.

Although the PVDF film provides a relatively simple setup and high precision in the measurement of SAW velocities and dispersive effects, the magnitude as well as the shape of the observed signal varies with the pressure used to press the foil onto the surface. Once the detector is removed from the surface of the sample, it is difficult to reproduce the previous setting exactly. As our primary interest was to obtain broadband phase information out of the SAW signals detected at two different distances, we investigated the correlation between contact pressure and signal quality, i.e. S/N ratio. The change in the waveform and its spectrum with different contact pressure is shown in Fig. 44 and Fig. 45, respectively. It can be seen from Fig. 44 that the waveform is distorted from bipolar shape as the knife-edge is pressed harder. This pulse distortion seems to be reflected as the growth of the subpeak observed at about 125MHz as shown in Fig. 45.

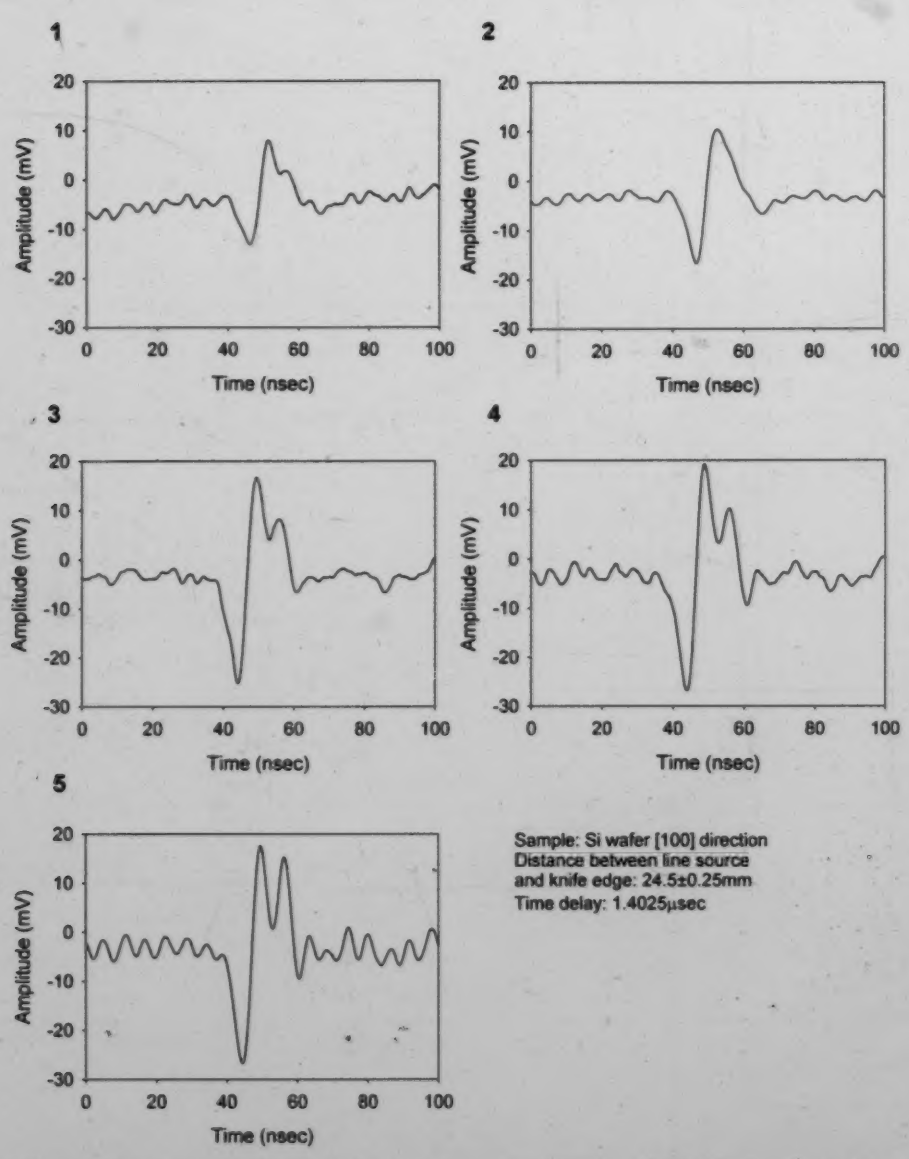

Fig. 44 Correlation between the waveform and contact pressure. Pictures are sorted in order of increasing contact pressure. The pressure was adjusted by the vertical position of the knife edge mount that is adjusted by 40 turns per inch screw. It was not possible to deduce the exact pressure applied on the PZT film, but it is expected to lie in the μN range. It can be seen that the waveform is distorted from its bipolar shape as the knife-edge is pressed harder. Once the film makes good contact with the sample, the peak amplitude of the signal quickly saturates.

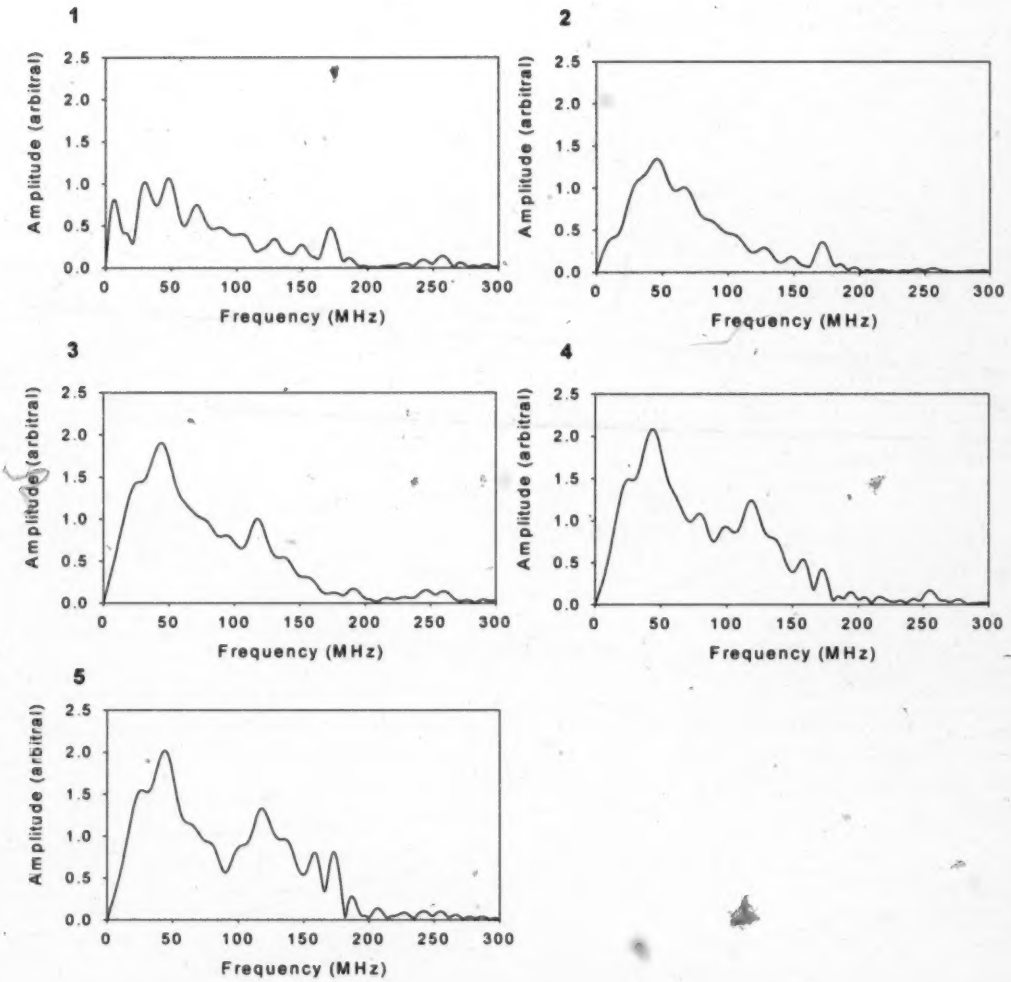

Fig. 45 Correlation between spectrum of the signals and contact pressure. Growth of a subpeak possibly due to the ringing noise is observed at about 125MHz. Inset numbers corresponding to those in Fig. 44.

III.4.2 Effect of Linewidth to the Signal amplitude.

As discussed in III.1.4, we have different optimal laser focal linewidths for different materials when thermal expansion is the main physical event for the SAW generation.

We tested the correlation between linewidth and signal amplitude on a (100) cut silicon wafer. The line focus was oriented on the silicon wafer parallel to the [010](or[001]) direction and the SAW traveled along [001](or[010]) direction before being picked up by the PVDF film.

The linewidth was controlled by varying the distance between cylindrical lens and the sample. Fig. 46 shows correlation between the peak to peak signal amplitude to the vertical displacement of the cylindrical lens. In this case the cylindrical lens had a focal length of 128mm and the cross-section size of the laser beam was approximately 12mm by 6mm. Fig. 47 shows the correlation between linewidth and signal amplitude. From the figure the optimal linewidth is found to be at a position of 11mm displacement where the linewidth was 43μm. However, linewidths were calculated based on a TEM00 mode, which results in a smaller linewidth than the actual width. Usually the M^2 factor results in a linewidth which is larger for KrF excimer lasers, which would be consistent with the calculated optimum linewidth of 74μm for Si[100] propagation based on a pulsewidth of 15 nsec and phase velocity of 4915 m/sec.

However, when ablation is the main physical event for the SAW generation, the maximum peak appeared at the focus of the lens. This was expected because the smaller the spot size, the higher the resultant plasma temperature and ablation pressure. The magnitude of SAW signals created by laser ablation can be more than 100 times bigger

than those created by thermal expansion. Also one should note that the pulse width of the SAW created by laser ablation is longer than that created by thermal expansion. This is due to the fact that the instantaneous thermal heating and cooling process is a shorter physical event compared with the unloading of plasma and compressed material following laser ablation.

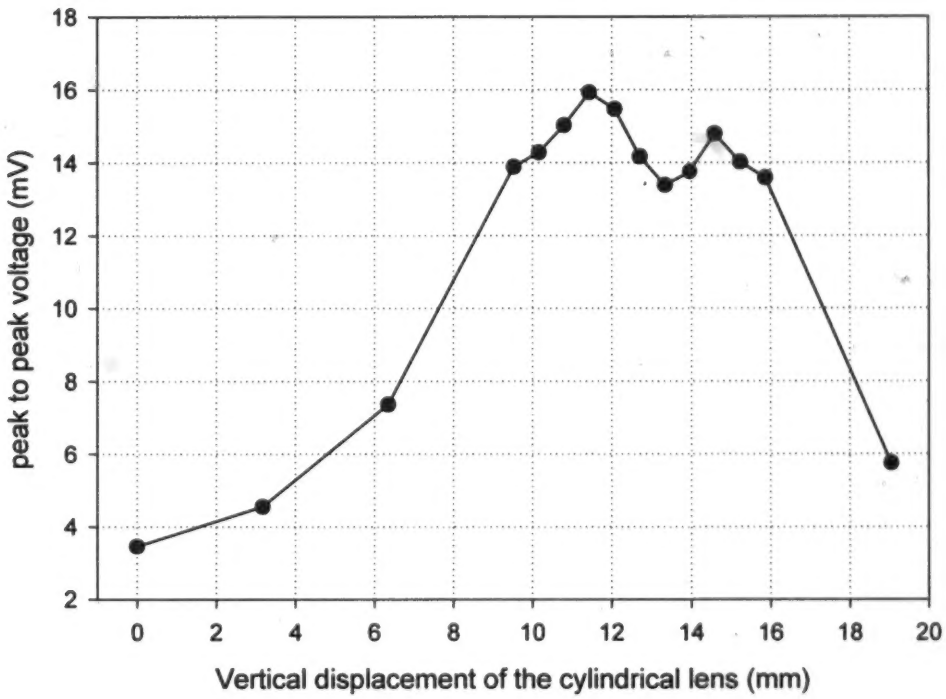

Fig. 46 Relation between vertical translation of the cylindrical lens and peak to peak voltage of the SAW signals (after 50db of amplification).

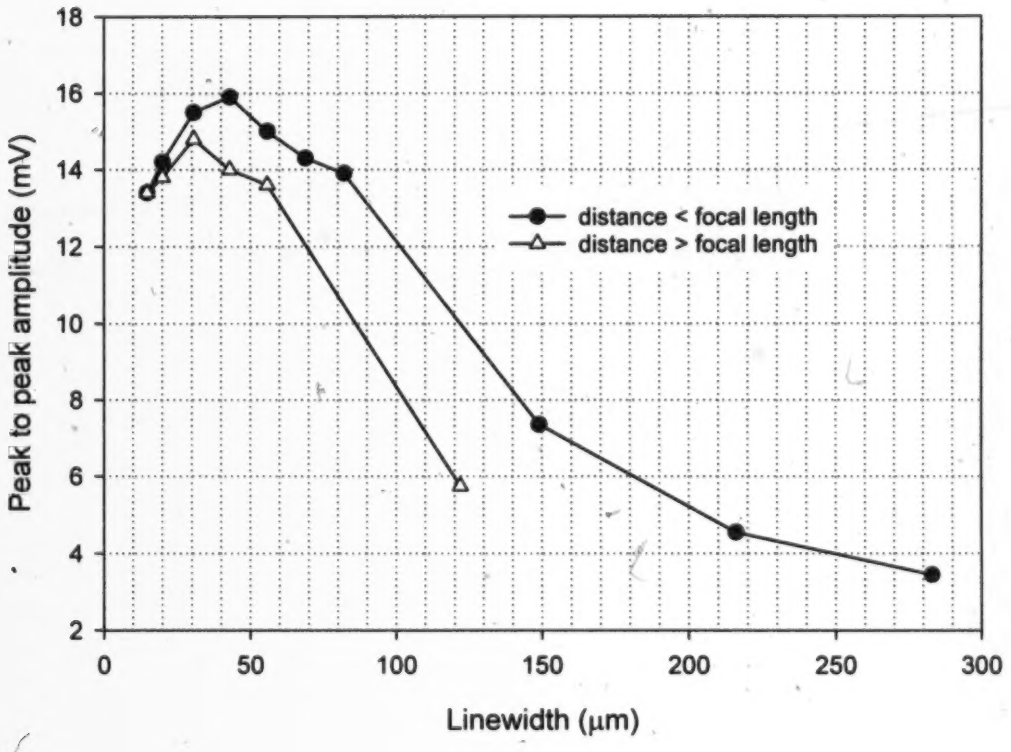

Fig. 47 Relation between peak-to-peak amplitude of SAW and linewidth deduced from the measurement shown in Fig. 46.

III.4.3 Dispersion Effect

Dispersion of the SAW becomes visible in the detected signals when the film properties are significantly different from the those of the substrate. Fig. 48 shows the dispersed acoustic signals from 1μm thick gold film deposited on an aluminum substrate. As can be easily seen from the figure, the pulse becomes broader as the wave travels a further distance. This indicates that there is a dispersion effect involved. Also one can see that in the wave packet lower frequency components appear first and higher frequency components later. This indicates that the Rayleigh wave velocity of the film is slower than that of substrate.

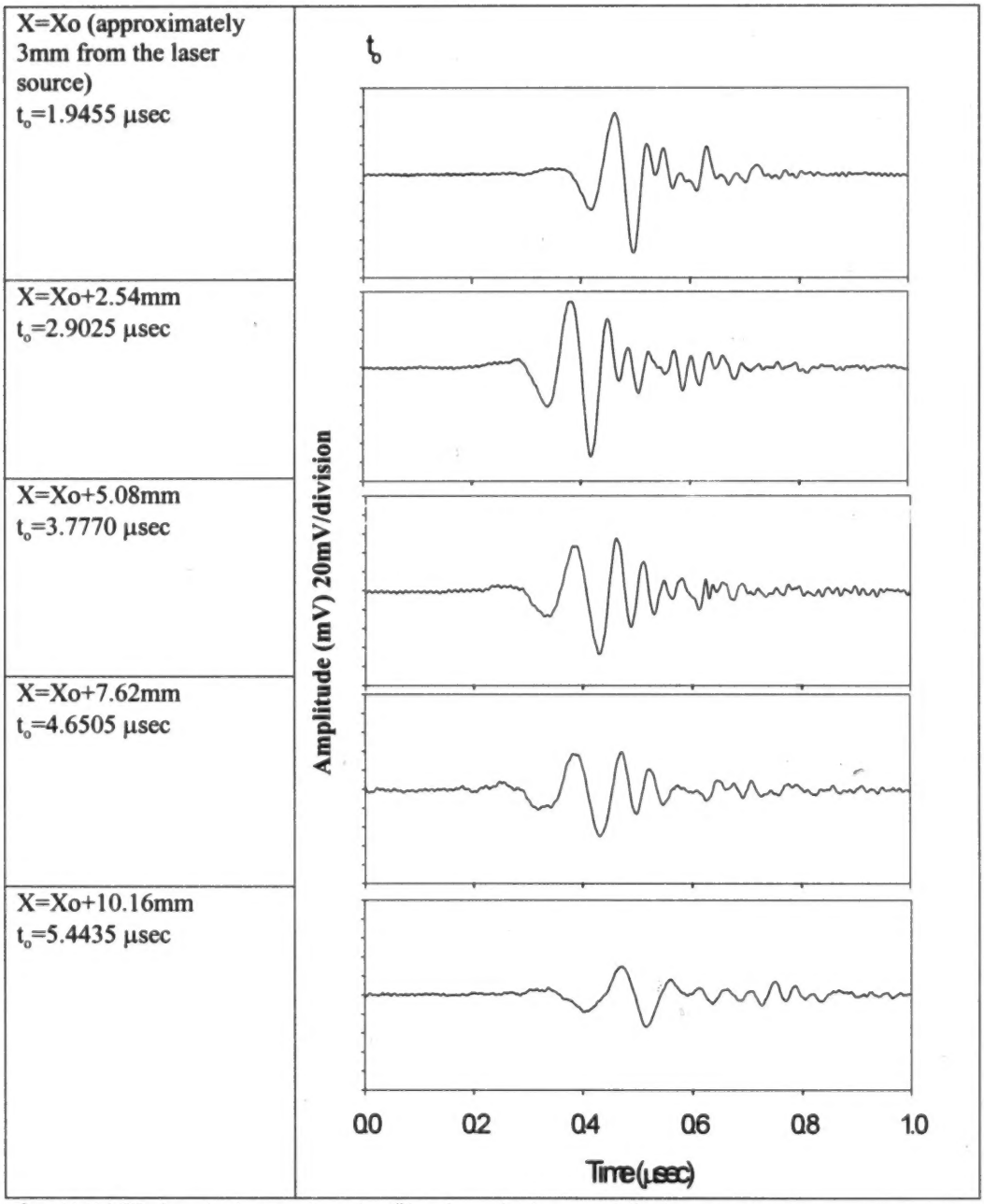

Fig. 48 SAW signals detected on Au film deposited on an Al substrate. As the propagation distance increases, the pulse broadens due to dispersion effects.

III.5 Data Analysis

In order to calculate the phase velocity as a function of frequency the phase delay of the spectral components between two of the waveforms must be calculated. A computer program written in Matlab language has been developed for the extraction of the phase velocity from two SAW signals detected at two different distances. For the example calculated here the two signals are chosen from the 2nd and 3rd signals in Fig. 48. The followings are the basic procedures of the program.

i) When two signals are detected at different distances, first they are placed into the same time coordinate range. The final number of the data samples should be a power of 2 in order to employ a Fast Fourier Transformation(FFT).

ii) The FFT's are taken for these two signals. The result of the FFT returns a list of complex numbers corresponding to the amplitudes of the various frequncy components. The spectrum shown in Fig. 49 is the absolute value of the result.

iii) Once the amplitude is given the phase information must be obtained. The equation for that is given as;

$$\theta = \arctan\left(\frac{IMAGINARY}{REAL}\right) \qquad (36).$$

A built-in function called "angle" is used in the program. Fig. 50 shows the result of the calculation for the 2nd signal and 3rd signals.

iv) Now the total phase shift can be reconstructed from the angle information which is initially in the range from $-\pi$ to $+\pi$. A built-in function called "unwrap" was employed in the program. It is an convenient tool, but sometimes it is fooled by sparse, rapidly changing, phase values. The resultant unwrapped phase information is shown in Fig. 51.

iii) Finally phase velocity at each frequency is calculated by using the equation;

$$V_p(f) = \frac{(x_2 - x_1)2\pi f}{[\varphi_2(f) - \varphi_1(f)]} \qquad (37)$$

where $V_p(f)$ is the phase velocity at frequency f, x is the distance from the line source, $\varphi(f)$ is the unwrapped phase at frequency f. Subscripts 1 and 2 indicate the near field and far field, respectively.

Fig. 52 shows the dispersion curve calculated from the real signals and some theoretical curves which are calculated by numerically finding zeros of the determinant of the matrix shown in III.1.2. Considering frequencies in the range of 5 to 25 MHz which form the main frequency components of the SAW, a best fit to the data was found to be the one calculated for a Young's modulus of 85GPa. This result agrees well with the reported Young's modulus for gold of 84.22GPa. The thickness of the film, 1000±50nm, was measured by the profilometer available at AMC which was used in the above calculation.

Also, acoustic waveforms based on the theoretical dispersion curve expected for 1000nm thick gold on an aluminum substrate were calculated. The results are shown in Fig. 53. These wave forms appear qualitatively similar to the real signals shown in Fig. 48, although effects of attenuation of the signal were not taken into account.

Dispersion curves were also calculated by using some typical constants for DLC films as shown in Fig. 54. As can be seen from the figure, the dependence of the dispersion curve on Poisson's ratio is quite small. Therefore, it is common to set the Poisson's ratio to the value of the bulk material. If the thickness and density of the film are already known from other measurements the experimental dispersion curve can be used to obtain a best fit value of Young's modulus.

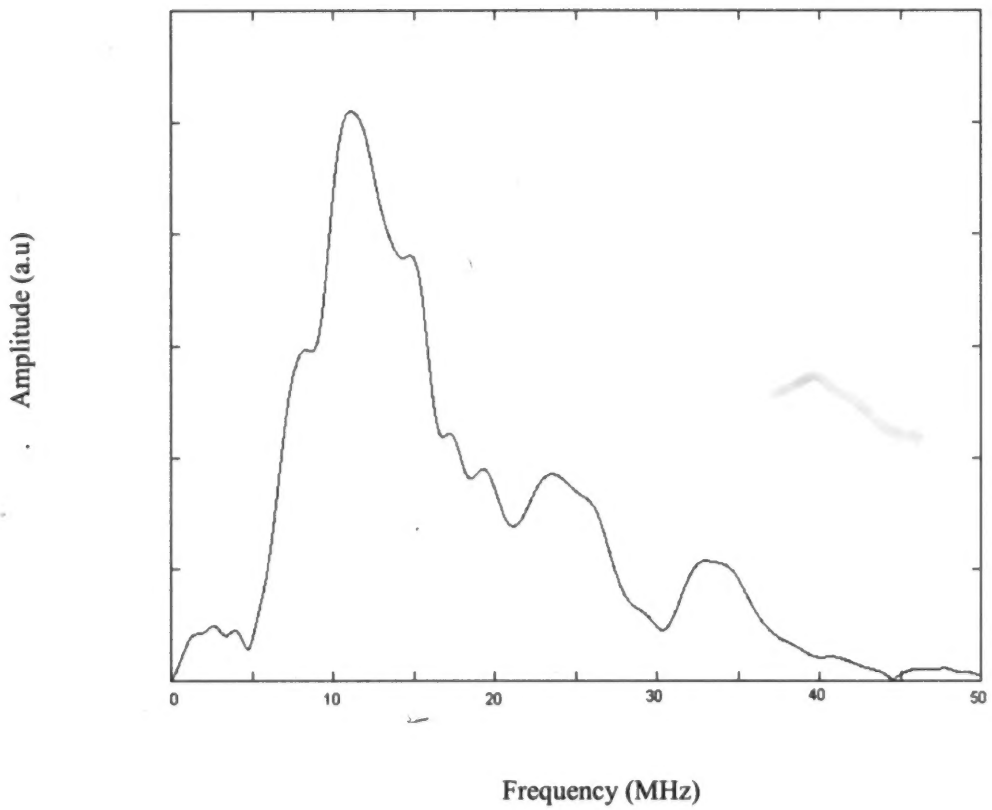

Fig. 49 Frequency spectrum of the SAW detected at x=xo+2.54mm on gold film on aluminum.

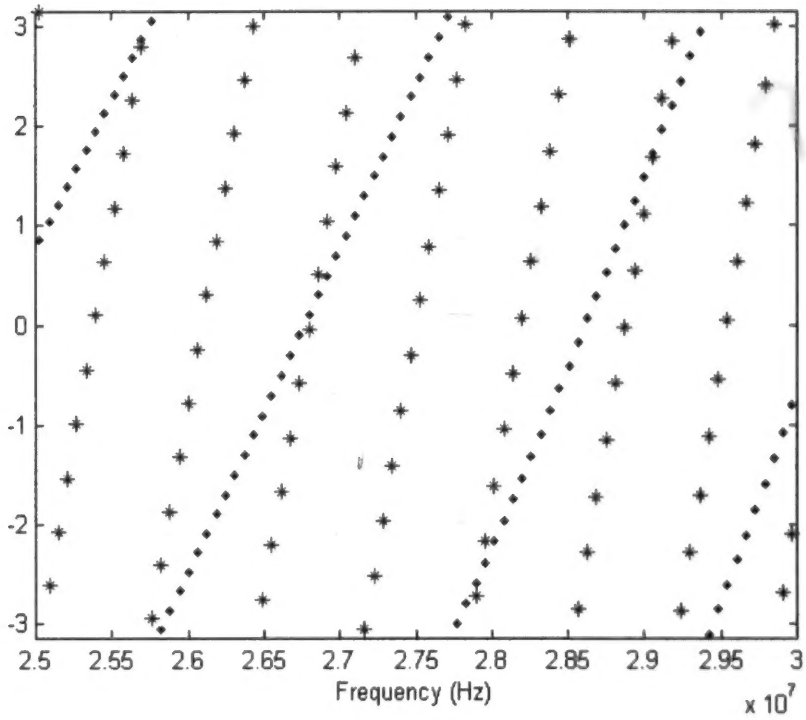

Fig. 50 phase information with +/-2nπ ambiguity for the SAW's detected at

X=Xo+2.54mm (plotted with .) and at $X=X_o$+5.08mm (plotted with *) from a gold film on an aluminum substrate.

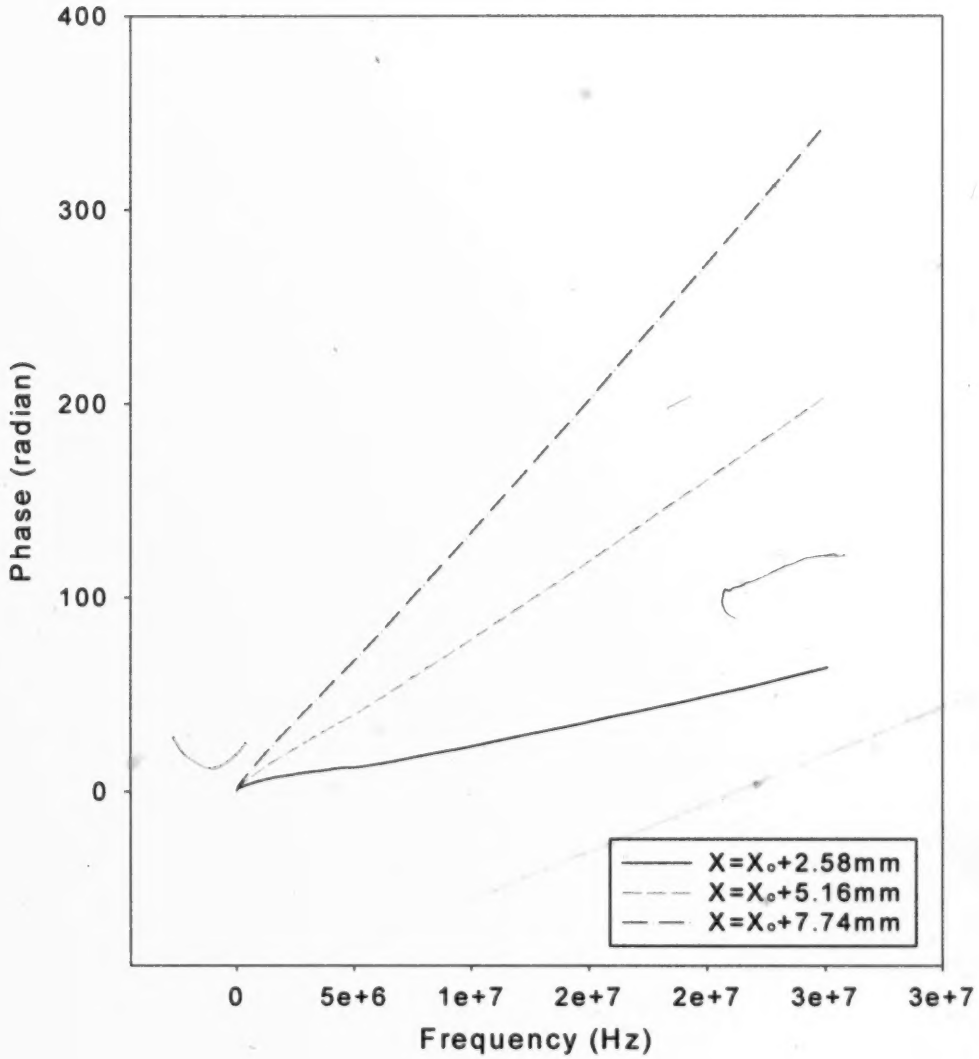

Fig. 51 Unwrapped phase information.

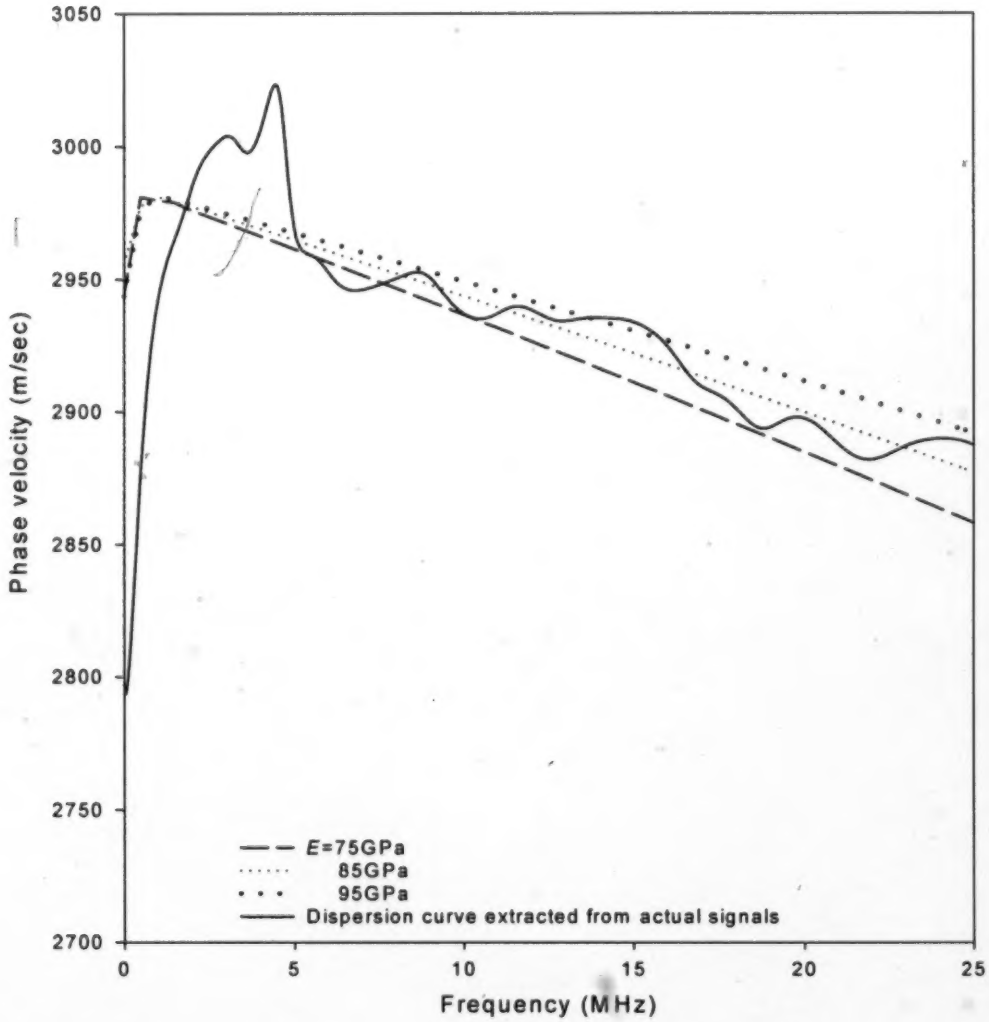

Layer : Gold (ρ=19300kg/m^3, ν=0.421, h =1000nm)
Substrate: Aluminum (ρ=2700kg/m^3, ν=0.345, E=73.9GPa)

Fig. 52 Phase velocity dispersion of SAW on a 1000nm thick gold film deposited on an aluminum substrate.

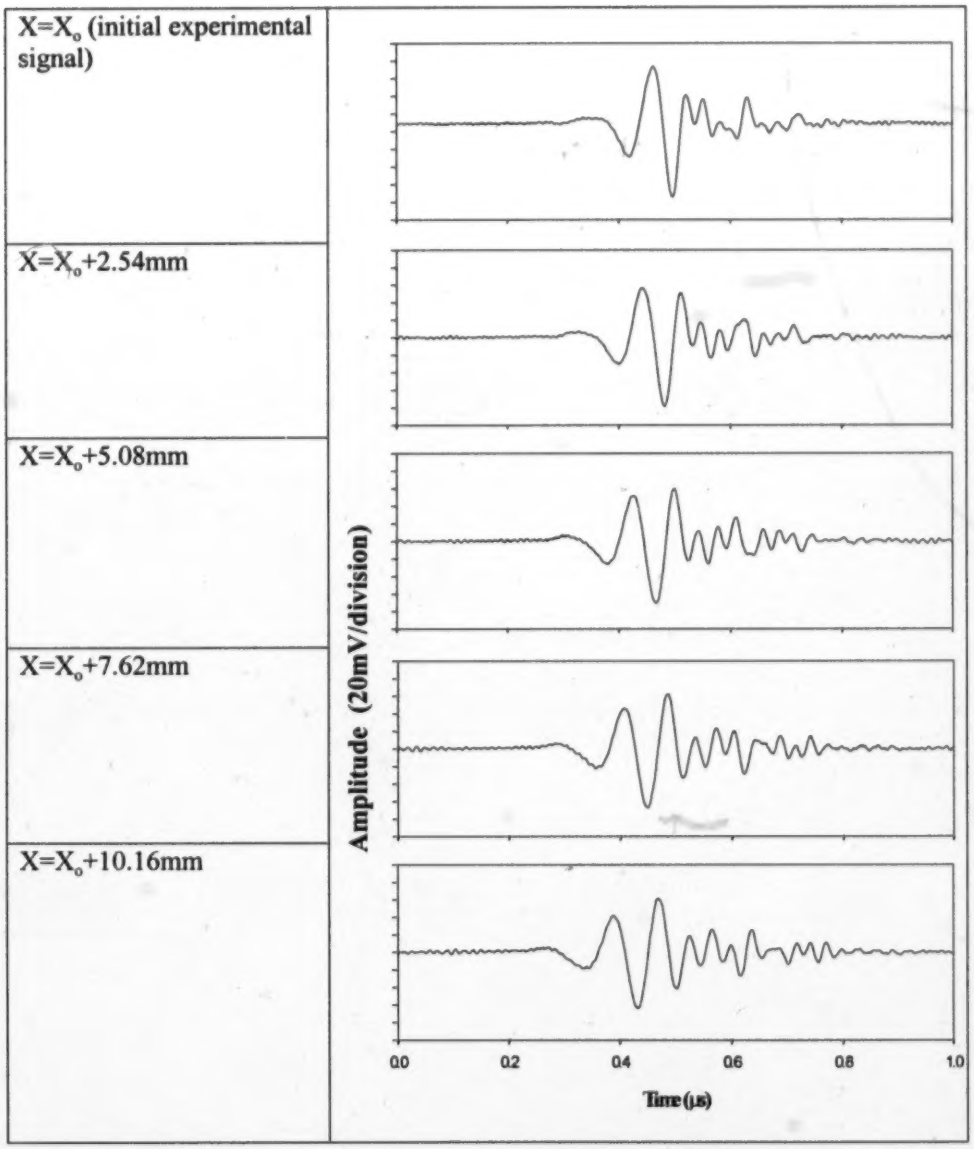

Fig. 53 Predicted waveform calculated based on the theoretical dispersion curve for a 1000nm thick gold film on an aluminum substrate. The initial signal for the calculation is the measured signal at X_o. The relative peak positions of the predicted waveforms agree reasonably with those of actual waveforms shown in Fig. 48.

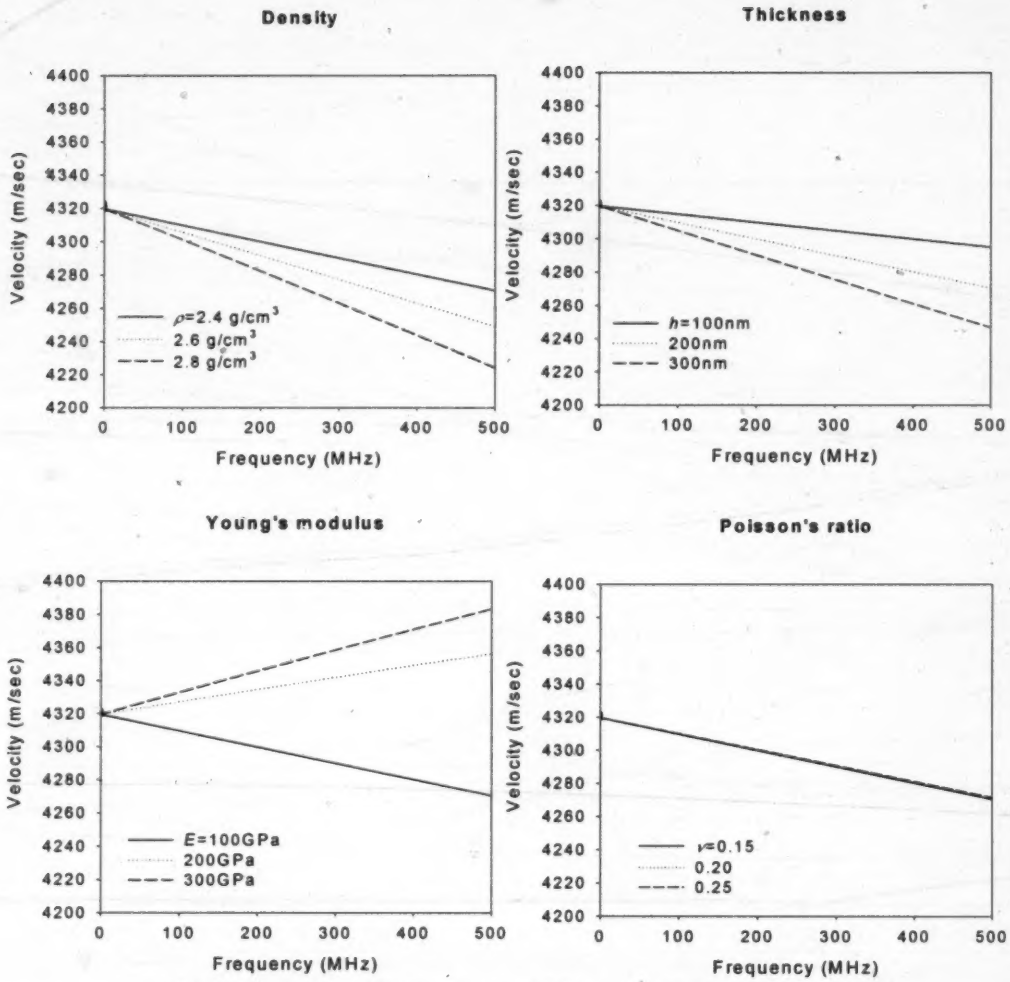

Fig. 54 Dispersion calculated for DLC with a single parameter value varied for each plot. The non varying parameters are set to their nominal values listed in the bottom of the figures. The substrate is Si(100) and propagation direction is{100}.

III.6 Summary

It was found that the extraction of phase information and phase velocities requires high fidelity measurement of the frequency components. Note that the frequency and phase response of the amplifier circuits is not important since signal distortions from the amplifier are the same for the signals measured at two distances and thus cancel out when the dispersion between the two waveforms is calculated. However, low frequency components less than 3MHz appear to be influenced by base line drift over the limited sample time window whereas high frequency components more than 30MHz appear to be corrupted by high frequency noise introduced into the system in our experiments. The amplitude of these high frequencies is limited in any case due to our long 15ns excitation pulse.

The sources of noise could include variations in the laser pulse shape from shot to shot, interference from bulk modes travelling in the substrate and reflecting off of the back side of the substrate, electromagnetic interference from the laser system, and mechanical resonance in the detector. It was found that the geometry and distance must be chosen carefully in order to avoid interference from reflected bulk waves in the sample.

External noise is not only the issue governing the measurement sensitivity. The measurement sensitivity also depends on the combination of film and substrate properties.

If the density and thickness are determined from other measurements then the measurement can yield a fairly accurate value for Young's modulus. Since Young's modulus of DLC film is known to be approximately 10 times higher in value than the

hardness [42], the thin film diagnostic should give valuable information on the quality of the DLC films produced.

IV Fabrication of DLC Films

IV.1 Substrate Preparation

It is necessary to clean substrates before deposition in order to remove grease and dust particles on the surface. For this purpose, we used ultrasonic cleaners. Firstly, ethanol is used as a solution for degreasing. Then acetone is used to remove ethanol and other contamination from the surface of the samples, and distilled water is used for removing acetone and all other residuals. The parts are cleaned for 10 min in each solution. After the cleaning process, the residual fluids on the surface of the samples are blown off with dry nitrogen for about 10 seconds and then exposed to air for a few minutes in order to remove any fluids on the surface. Dicing or cutting of the samples must be done before cleaning procedures. Once cleaning is finished, the samples are immediately placed into the chamber and the chamber is pumped down in order to minimize any contamination of the surface after the cleaning process.

IV.2 Setup

Fabrication of amorphous carbon films without magnetic guiding of carbon plasma was conducted under the intermediate vacuum condition. A diffusion pump with the help of a backing rotary pump achieved a pressure of around 2×10^{-5} torr. Fig. 55 shows a schematic diagram of the vacuum system. A liquid nitrogen filled cold trap with a baffle is installed in order to prevent the chamber from the contamination from oil vapor coming out from diffusion pump.

Fig. 56 shows a schematic diagram of the coating setup. In the chamber the laser pulse (KrF laser or Nd:YAG laser) is focussed by a plano-convex lens (f= 500 mm, ϕ=50mm) and enters the chamber through a UV grade quartz window. In the chamber the laser pulse first goes through a debris shield. The debris shield, which is simply a slowly rotating UV grade quartz window, prevents the chamber window from being contaminated by the coating species. This apparatus allows us to carry out coating runs over 10,000 shots, although the transmission of the debris shield will drop slowly during the run. Once the transmittance of the debris shield has dropped significantly, it can be cleaned by using ammonium difluoride. A mylar mask is employed in order to minimize the area of the shield exposed to the ablation species. After going through the debris shield, the laser pulse focusses to a point onto the carbon tape target from an angle of 40 degrees with respect to the surface normal. This tape target is transported from one wheel to the other which is driven slowly by a motor drive in order to assure that there is a fresh target surface for each laser shot. The laser intensity onto the target is adjusted to approximately 1.0 GW/cm^2 for usual operation, which is sufficient to cause ablation of the target source. The intensity can be changed by adjusting the laser pulse energy by

decreasing the discharge voltage, inserting an attenuator, or by changing the focal spot size by moving the focussing lens along the optical path. Energy density was calculated by dividing the input energy (monitored by a photodiode) by the spot size measured with a CCD camera focal spot measurement system. Up to about 200mJ of energy can be emitted per pulse from KrF laser. Substrates to be coated are placed onto the sample holders which have circular disks with a diameter of one inch. Up to three sample holders can be mounted on the rotation apparatus placed in the chamber. The distance between the epicenter of the each sample holder to the ablation point on the tape target is 6 cm with an angle of 20 degrees normal to the surface of the tape target to be ablated. Each sample holder is rotated during the coating run in order to minimize thickness variations on the sample. The rotation frequency is approximately 0.1 Hz, while a train of laser pulses is injected with a frequency of ~15 Hz, which is triggered by a computer. This sample rotation unit was taken out of the chamber for some experiments. When magnetic field guiding is employed the setup is modified as earlier shown in Fig. 11. The individual shot input energy and the total integrated laser energy are monitored by a calibrated photodiode and data are stored in the computer. These values can later be used for calculating deposition rate with respect to the input energy.

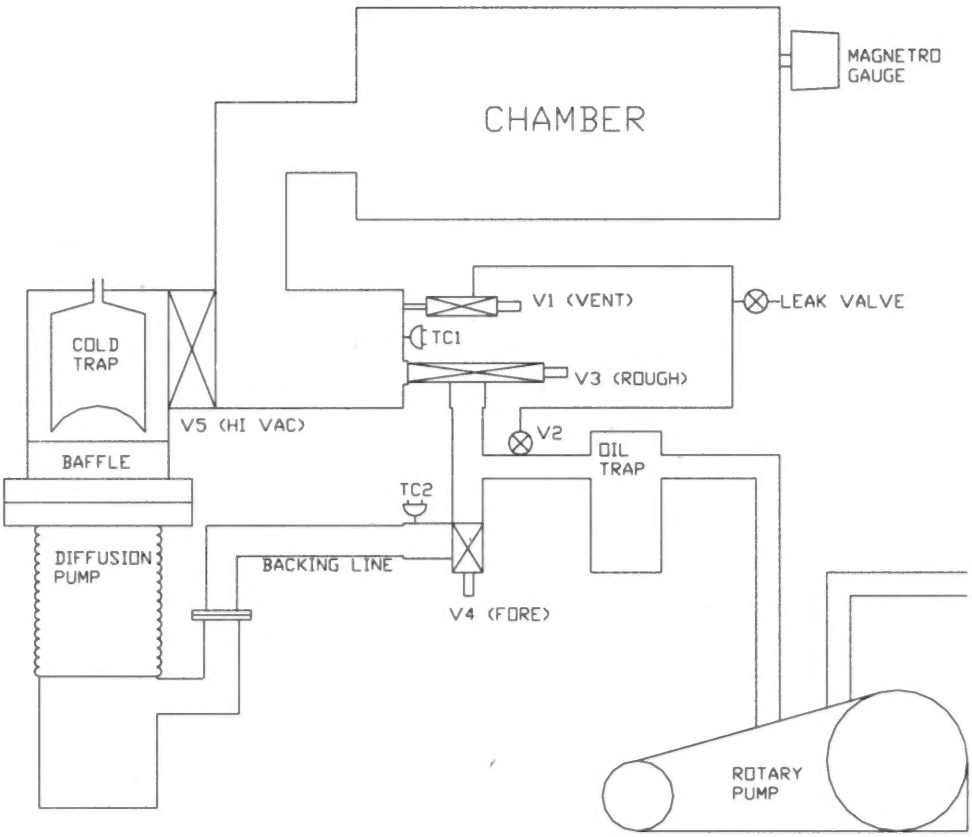

Fig. 55 Schematic diagram of the vacuum system used for pulsed laser deposition

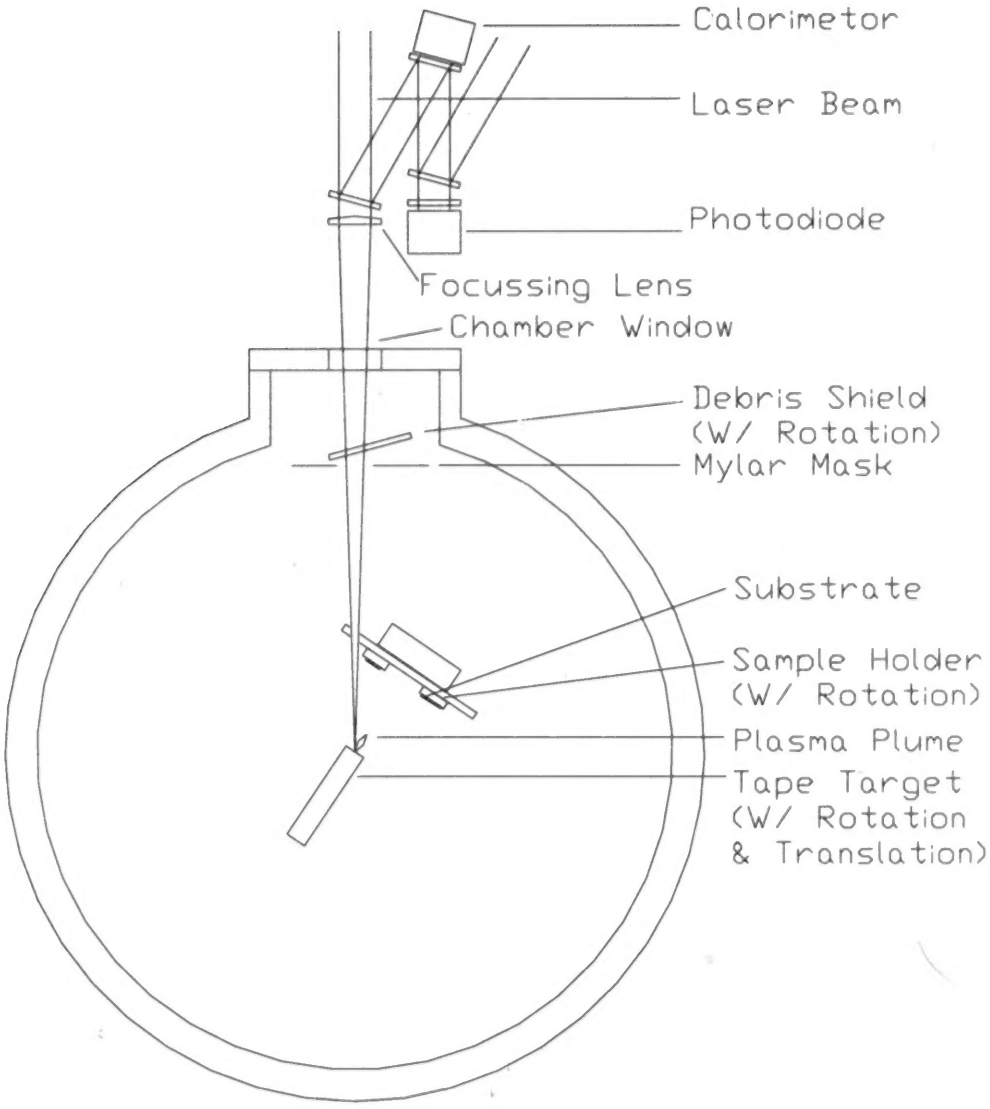

Fig. 56 Setup for Pulsed Laser Deposition.

IV.3 Supportive experiments before coating run

IV.3.1 Faraday Cup Measurement

In order to determine the focal condition, a Faraday cup was used to diagnose the laser produced plasma. We assumed the lens position which gives the largest signal amplitude is the best focus position. Once the best focus position is found, the lens is moved along the optical axis to the point which gives desired laser power density at the target. Fig. 57 shows an example of the Faraday cup measurement taken for the Nd:YAG laser injection. Based on the distance between the target and the detection head of the Faraday cup of 165mm, the kinetic energy of the carbon ions at the peak of the current pulse is estimated to be approximately 1480eV at the best focus condition. In the figure the lens position which gives the maximum signal amplitude was defined as X_o. As can be seen from the figure, the signal amplitude drops and the peak position shifts towards later times as the lens position is shifted from X_o. If the distance between the Faraday cup and the target is known, the kinetic energy of ions can be calculated. We found ion energies of approximately 280, 100 and 50eV for laser intensities of the 10GW/cm^2±40%, 4GW/cm^2±35%, and 0.7GW/cm^2±35% for the KrF excimer laser. These intensities were calculated by dividing laser energy by the product of the spot size at the target and the full width half maximum (FWHM) of the laser duration. In the calculation, laser energy of one pulse and time duration were fixed to 100mJ ±30% and 15 ns, respectively. A first estimate of the spot sizes at various focal conditions was obtained from the burn patterns made on a piece of paper inserted in front of the target before the chamber is evacuated in order to find the in-focus lens position. Once in-focus lens position is found, then CCD

camera was used to measure detailed focal spot size at different focal conditions. The measurement results are shown in Table 2. The Faraday cup was kept in the chamber during the experiment whenever possible so that the plasma generation could be monitored. Similar measurements were taken along the horizontal axis at the exit of the curved solenoid coil before magnetic field is employed during the coating run. Fig. 58 shows the signals observed when a Faraday cup is translated horizontally at the exit of the curved solenoid coil. The kinetic energy was estimated to be between 220 to 300 eV depending on how the trajectory of the particles is calculated.

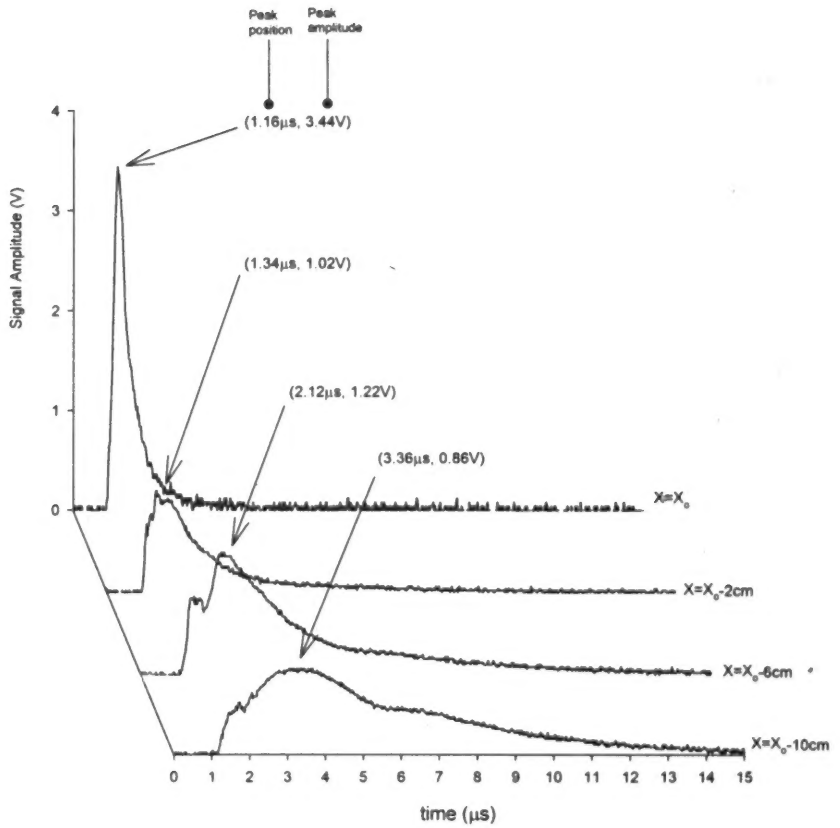

Fig. 57 An example of the Faraday cup measurement for the YAG laser irradiation onto the graphite tape target. The distance between the detection head of the Faraday cup and the target is 165mm.

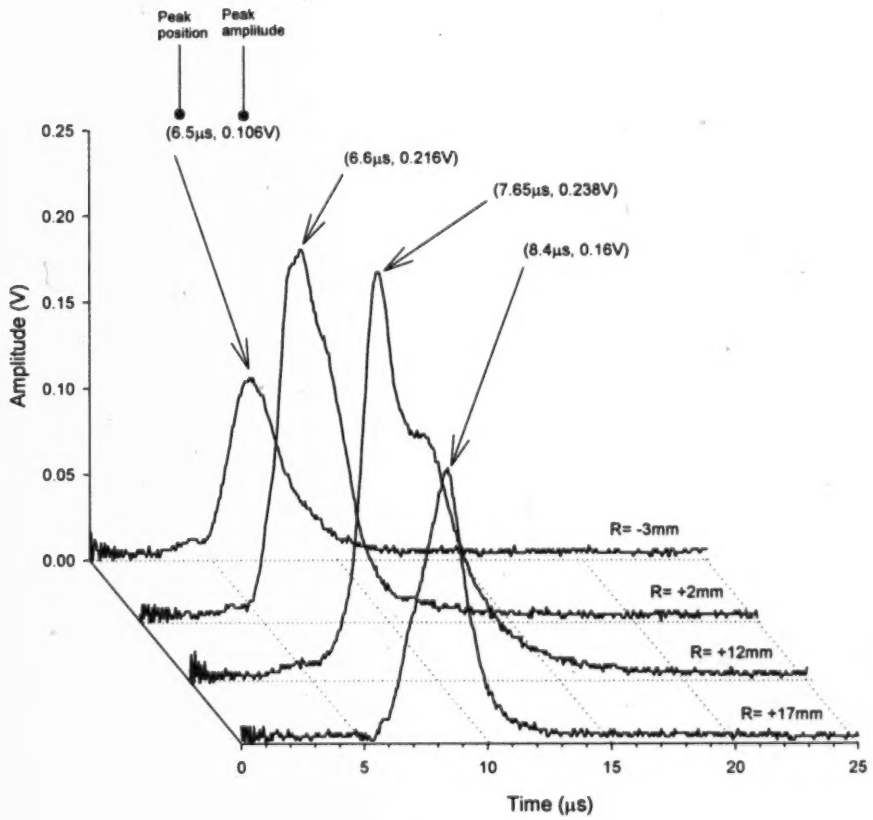

Fig. 58 Distribution of the signals obtained by Faraday cup measurement at different horizontal positions at the exit of the solenoid coil. R indicates the distance from the center of the solenoid coil and the polarity is taken towards the outer radius of the curved solenoid coil. (Please refer Fig. 11 for the schematic of the setup.) KrF laser with a pulse energy of approximately 120mJ is focussed onto the graphite tape target with a 50cm focal lens. The target was at the best focus position and the laser intensity used was $10GW/cm^2$.

Table 2 The results of the laser intensity measurements by using a CCD camera. For calculations, the laser pulse was assumed to have a energy of 100mJ and the time duration of 15ns (FWHM).

Lens position with respect to the in-focus position	Radius of 50% energy contour	Intensity based on 50% contour	Peak intensity
0cm	100±10μm	10±2GW/cm^2	15GW/cm^2
1.5cm	160±10μm	4±0.5GW/cm^2	5.5GW/cm^2
3cm	380±10μm	0.7±0.02GW/cm^2	1GW/cm^2

IV.3.2 Calibration of quartz crystal monitor

When the sample was located only at zero degrees with respect to the target normal, a quartz crystal monitor (QCM) was placed at the angle of the 40 degrees in order to monitor the approximate thickness deposited on the sample during the measurement. However, an initial calibration is necessary for such a measurement. Fig. 59 shows the readings of the two QCM is placed at the 0 (QCM1) and 40 (QCM2) degrees with respect to the target for the various lens positions, i.e., with different laser intensities. The distance between the QCM's and the target were approximately 7cm. The KrF laser pulses with pulse energies of 70 to 150 mJ were focused with a 500 mm focal length lens for these measurements. The density of the film was set to 1 g/cm^3 by default in the QCM module since we don't know the exact density of the film during the coating run. After calibration we made one sample film by placing the substrate over the QCM1 position and measured the thickness directly with profilometer. The results are discussed in the next chapter. The reading from the QCM2 was monitored during the coating run. Fig. 60 shows the angular dependence of the deposition rate with respect to the different lens positions obtained with both KrF and Nd:YAG lasers for comparison.

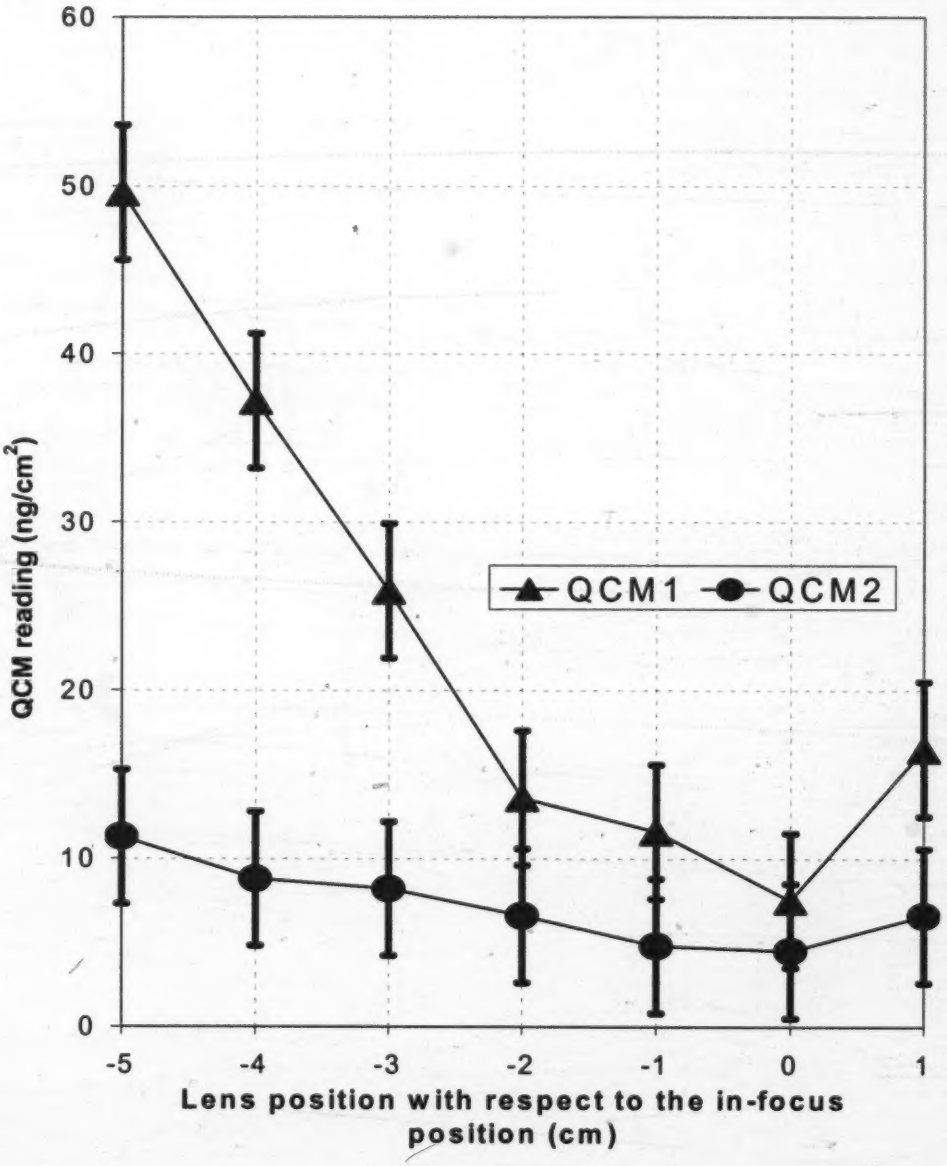

Fig. 59 QCM reading with respect to the lens position. The QCM1 and QCM2 are located at 0 and 40 degrees with respect to the target.

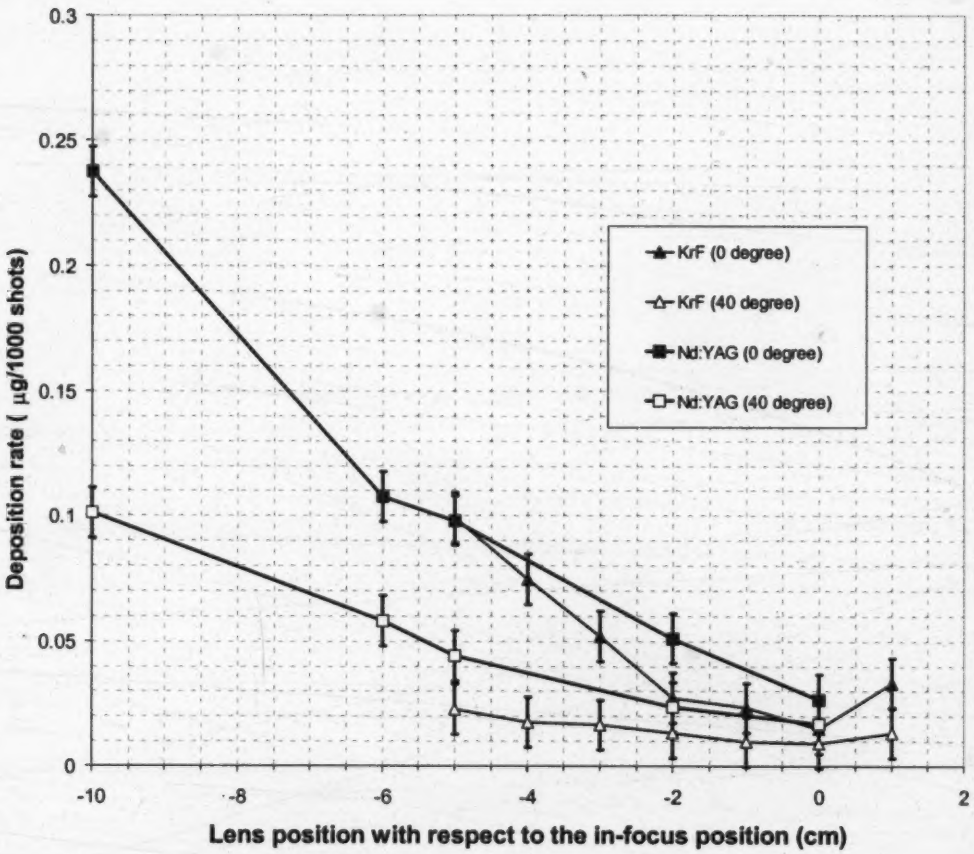

Fig. 60 The angular dependence of the deposition rate with respect to the different lens positions. Measurements are taken for KrF and Nd:YAG laser. The distance between the target and the quartz crystal monitor is approximately 7cm and the average pulse energy is about 120mJ and 1000mJ for KrF laser and Nd:YAG laser respectively. The reduction in the deposition rate was observed when the lens position is adjusted to the in-focus position.

IV.4 Films deposited

For this thesis work 23 samples were fabricated with various conditions as tabulated in Table 3. All samples were fabricated with a KrF laser not with a Nd:YAG laser, although supportive measurements necessary for film fabrications described in IV.3 were conducted for a Nd:YAG laser as well. The detailed characterization of a number of these films is discussed in the next chapter.

Table 3 samples fabricated with PLD with various conditions.

sample#	date	substrate	target	B-field	intensity (GW/cm2)	distance (mm)	angle (degree)	no. of shots
1	970625	(a)Quartz	C		4	54	0	6500
		(b)NaCl	C		4	49	60	6500
		(c)Si	C		4	56	0	6500
		(d)Si	C		4	56	30	6500
		(e)Si	C		4	56	30	6500
2	970708	(a)Si	C		4	56	0	2000
		(b)NaCl	C		4	49	0	2000
		(c)NaCl	C		4	49	30	2000
		(d)NaCl	C		4	49	30	2000
		(e)NaCl	C		4	49	60	2000
3	970903	(a)NaCl	C		4	60	0	800
		(b)NaCl	C		4	60	30	800
4	980820	(a)Cu	C		4	60	30	9000
		(b)BK7	C		4	60	30	9000
		(c)Quartz	C		4	60	30	9000
		(d)Si	C		4	60	30	9000
5	981020	(a)Cu	C		4	60	30	15000
		(b)BK7	C		4	60	30	15000
		(c)Quartz	C		4	60	30	15000
6	981209	(a)Cu	C		4	60	30	2000
		(b)pylex	C		4	60	30	2000
		(c)s1uv	C		4	60	30	2000
		(d)Si	C		4	60	30	2000
		(e)NaCl	C		4	60	30	2000
		(f)NaCl	C		4	60	30	2000
		(g)NaCl	C		4	60	30	2000
7	981213	(a)Si	C		>0.7	60	30	4000
		(b)s1uv	C		>0.7	60	30	4000
		(c)pyrex	C		>0.7	60	30	4000
		(d)s1uv strip	C		>0.7	60	30	4000
		(e)NaCl	C		>0.7	60	30	4000
		(f)NaCl	C		>0.7	60	30	4000
8	990113	(a)Si	C		4	150	0	600
		(b)NaCl	C		4	150	0	600
9	990118	(a)NaCl	C		4	150	0	8000
		(b)s1uv strip	C		4	150	0	8000
		(c)Si	C		4	150	0	8000
10	990119	(a)NaCl	C		0.7	150	0	1200
11	990303	(a)Si	C		4	150	0	1200
12	990307	(a)Si	C		4	60	30	4500
13	990310	(a)Si	C		4	60	30	4000
14	990316	(a)Si	Cu		4	150	0	3000
15	990317	(a)Si	Cu		4	150	0	2000
16	990318	(a)Si	Cu		4	150	0	22500
17	990330	(a)NaCl	C	O	10	400		10000
		(b)NaCl	C	O	10	400		10000
		(c)NaCl	C	O	10	400		10000
		(d)NaCl	C	O	10	400		10000
18	990402	(a)NaCl	C	O	10	400		10000
		(b)NaCl	C	O	10	400		10000
		(c)NaCl	C	O	10	400		10000
		(d)NaCl	C	O	10	400		10000
19	990411	(a)Al(100nm) on Si	C	O	10	400		13000
20	990413	(a)Si	Cu	O	10	400		21000
21	990417	(a)NaCl	C		10	50	0	1000
		(b)Al(100nm) on Si			10	50	0	1000
		(c)NaCl	C		10	60	30	6500
		(d)Al(100nm) on Si	C		10	60	30	6500
		(e)s1uv strip	C		10	60	30	6500
		(f)s1uv	C		10	60	30	6500
22	990419	(a)NaCl	C		4	50	0	450
		(b)Al(100nm) on Si			4	50	0	450
		(c)NaCl	C		4	60	30	4000
		(d)Al(100nm) on Si	C		4	60	30	4000
		(e)s1uv strip	C		4	60	30	4000
		(f)s1uv	C		4	60	30	4000
23*	980515	(a)Si	C	O	10	460		150000

*sample provided by Dr. Tsui

V Characterization of Diamond Like Films Produced

The deposited films were characterized with various methods. Table 4 summarizes the measurement techniques employed with comments on the ability of each technique. Also, measurement techniques applied for the characterization of each sample are summarized in Table 5.

Table 4 Measured properties and characterization methods

Properties	Characterizing method	Comment
Film thickness	Profilometer	Ideal for measuring h>100nm Direct measurement
	EELS (Zero loss)	Error is large (approx. ±30%) Best for h<50nm Film must be placed on EELS grid
	Ellipsometer	For a very thin film (h<30nm) with known index of refraction placed on the substrate with known index of refraction.
Density	Microbalance	Error is large for thin films (approx. ±100%) Direct measurement
	EELS (plasmon peak)	Free electron model assumed
Absorption Coefficient	Spectrophotometer	Can be calculated from the reflectance and transmittance
Index of refraction	Ellipsometer	Ideal for h<30nm. Sensitive to surface roughness and transition layers
Extinction coefficient	Spectrophotometer	Calculated from absorption coefficient
	Ellipsometer	Ideal for h<30nm. Sensitive to surface roughness and transition layers
Optical gap	Spectrophotometer	Applying Tauc's model to the spectrum of the absorption coefficient.
sp^3 fraction	EELS (K-edge peak)	Direct measurement
	EELS (Plasmon peak)	Use parametric relationship (Fig. 80)

Table 5 Measurement techniques applied for each sample.

sample #	profilometer	zero loss (EELS)	QCM	microbalance	plasmon (EELS)	K-edge (EELS)	spectrophotometer	ellipsometer	SAW	resistance
1		X								
2		X								
3		X			X	X				
4	X						X		X	
5	X									
6	X	X			X	X				X
7	X	X			X	X				
8	X	X	X		X	X				
9	X			X						
10	X	X	X		X	X				
11	X		X							
12	X		X	X						
13	X		X							
14	X									
15	X		X							
16										
17										
18		X			X	X				
19										
20	X									
21	X	X			X	X	X			
22	X						X			
23								X		

V.1 Thickness Measurement

Thickness can be measured directly by the stylus instrument (profilometer) at AMC (Alberta Microelectronics Corp.). This measurement also gives us surface roughness of down to a few nm.

The thickness can also be calculated from EELS measurements based on the fractional transmission of the zero loss peaks for the sample if the mean free path of the electron in the sample is known. This measurement gives a range of the error of approximately ±15% for DLC samples since the mean free path of an electron with a kinetic energy of 200 KeV in graphite and diamond is about 150 to 200 nm. Ellipsometry can be used as well to measure the thickness of the very thin films with a thickness less than 30nm placed on a substrate if the index of refraction and extinction coefficient for the both film and substrate are known.

An example of a profilometer measurement from a 70nm thick film is given in Fig. 61. The samples fabricated ranged in thickness from 30nm to 3μm thick with no guiding magnetic field and 10nm to 200nm thick with a guiding magnetic field. The distribution of the thickness across the films deposited with magnetic field guiding was also measured.

The correlation between the profilometer measurement and EELS measurement was investigated from the sample #21. Thicknesses of 36±4nm and 21±5nm were observed with profilometer measurement and EELS measurement, respectively. This discrepancy may be due to some misalignment in the deposition setup. Due to the time limitations and the lack of knowledge of the exact refractive index of the film no attempt was made to measure the thickness with the ellipsometer technique.

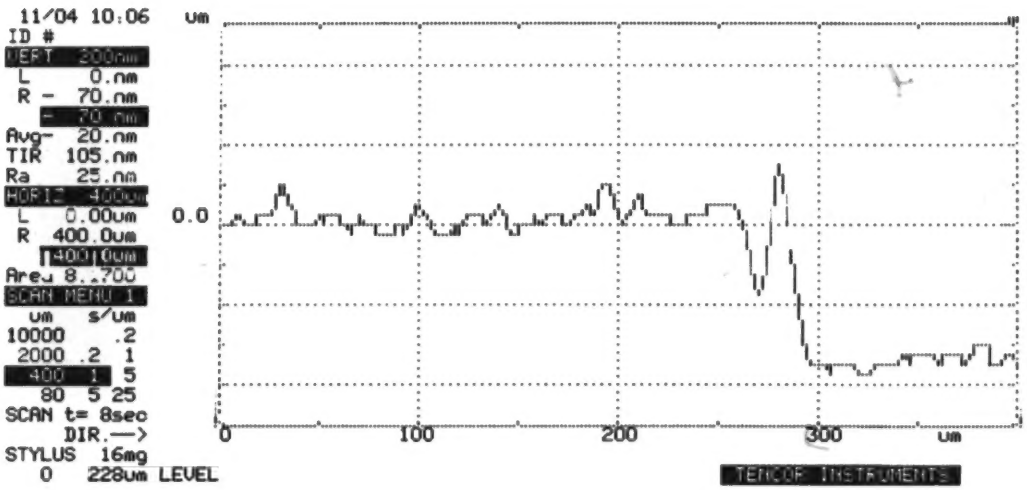

Fig. 61 Profilometer measurement of a 70nm thick DLC film (sample # 4-(c)). The grid spaces represent 100mm per division on the horizontal scale and 40nm per division on the vertical scale.

V.2 Density Measurement

Density was measured by measuring the film mass directly with the microbalance which is available in the Microanalysis Laboratory in the Department of Chemistry at the University of Alberta and dividing by area and thickness. The film mass is the mass difference of the sample before and after coating run. Since the film mass is so small (e.g. ~20μg for 1200nm thick DLC with the area of 2mm by 25mm), a few dust particles on the sample can make the result inaccurate. Therefore, the samples were kept away from dust particles as much as possible in handling. The PLD carbon film deposited with a laser intensity of 4.0GW/cm^2 (sample #9) had densities of 2.3±0.5g/cm^3. The density was also estimated from the plasmon peak measured with EELS as discussed in II.1.1. Table 6 shows the results. Density can also be determined by the areal mass density measured with a quartz crystal monitor together with the thickness obtained by profilometer measurement. The density of the film is calculated by simply dividing the products of the deposition rate shown in Fig. 60 and the number of the laser shots by the film thickness obtained by profilometer measurement, and was found out to be 2.4±0.3g/cm^3. This value agreed with the above measurements from weighing the samples to within an error of 10%. However, one should note that this error would be increased significantly if the thickness of the film becomes too thick (probably on the order of a few hundred microns) where the equation (2) does not hold anymore. For thicker film equation (1) should be employed and shear wave velocity in the film should be measured therefore.

Table 6 Results of density measurements.

Sample #	Substrate #	Laser intensity (GW/cm^2)	Density (g/cm^2)	Error	Method	Comment
3	(b)	4.0±0.5	1.7	±30%	EELS	
6	(e)	4.0±0.5	1.7	±30%	EELS	
6	(f)	~0.7	1.6	±30%	EELS	
7	(f)	4.0±0.5	2.0	±30%	EELS	
8	(b)	4.0±0.5	1.7	±30%	EELS	
9	(b)	4.0±0.5	2.3	±20%	Microbalance	Measured for the free standing film
10	(a)	0.7±0.02	1.75	±30%	EELS	
12	(b)	4.0±0.5	Inconclusive	>100%	Microbalance	Sample was too large for the stage of the digital balance that gave rise to the large fluctuations on the readings.
18	(a)	10±2	1.3	±30%	EELS	
18	(b)	10±2	1.75	±30%	EELS	
21	(c)	10±2	Inconclusive	>100%	Microbalance	Sample broke into pieces
21		10±2	1.75	±30%	EELS	

V.3 Measurement of Index of Refraction

V.3.1 Imaginary Part of Index of Refraction(Extinction Coefficient)

The imaginary part of the complex index of refraction was measured using a spectrophotometer. A CARY spectrophotometer was available at the Thin Film Laboratory at University of Alberta. It has three different lamps (UV, visible, and infrared) with optical gratings which allow for scanning a wide range of the wavelength (180nm to 3000nm) and has two optical detectors (UV-visible and infrared) for detecting such wavelengths. One can measure either external transmittance or reflectance of the sample by changing modules.

When the imaginary part of the complex index of refraction is of interest, the internal transmittance of the film is measured. Internal transmittance cannot be measured directly, however, it is possible to calculate by using the measured transmission results by correcting for the reflectance at the interfaces using the equation

$$T_{FI} \approx \frac{T_E}{T_{SI}} \frac{1}{1-R} \tag{38}$$

where;

T_{FI}: Internal transmittance of the film,

T_E: External transmittance of the whole sample,

T_{SI}: Internal transmittance of the substrate,

R: Reflectance from the surfaces of the sample and substrate.

Transmittance of the substrate can be calculated if it is made of known materials or estimated from measurement. Account must be taken of the effect of multiple reflection to give a better result which has less than 0.5% of error as shown in Fig. 62 for a fused

silica slab. The dispersion formula for the refractive index of a UV grade fused silica was taken from [74] and the internal transmittance was taken from [75].

The substrate must have high transmittance over the examined frequency region. We made a transmission measurement for the DLC film deposited on an S1 UV grade fused silica which has high internal transmittance from 300nm to 1000nm. The film thickness was 70±5nm. In the CARY spectrophotometer a background is taken before the sample is placed into the instrument in order to calibrate the 100% transmission level at each wavelength. However, because this zeroing by the instrument is inaccurate when a large wavelength range is covered, a more accurate result is obtained by doing the background subtraction manually by taking a measurement without the sample first and then correcting the data by 100% of transmission reference spectrum in order to compensate for residual instrumental error as much as possible.

Fig. 63 shows the measured external transmittance of a 70±5nm PLD deposited DLC on 3/4 inches thick S1UV fused silica and also 28±10nm samples deposited on 1mm thick S1UV quartz. One normally should take into account the Fabry-Perot interference effect, which is caused by the wave interference between film-air interface and the film-substrate interface when the thickness of the film is uniform. However, a significant amount of such interference modulation is lost in the measured transmission plot since the thickness of the tested film was not uniform over the measured area. Also such interference may be washed out if the DLC forms a graded index interface with the quartz substrate. This may result in the absence of sharp peaks both in the reflectance and transmittance spectrum. The reflectance of the film was measured by the same spectrophotometer. An integrating sphere was employed in order to collect all the

scattered light from the surface. The result is shown in Fig. 64. Using this reflectance measurement, the internal transmittance of the film was calculated by using equation (38) and is plotted in Fig. 65. The effect of the modulation appearing in Fig. 64 is so small that it is hardly apparent in Fig. 65

The absorption coefficient was calculated from the internal transmittance and is plotted in Fig. 66. Thicknesses of 70±5nm, 28±10nm, and 28±10nm were used to calculate the absorption coefficient of the samples #4, #21, and #22, respectively. The absorption coefficient is then used to calculate the imaginary part of the refractive index n_i (extinction coefficient) as plotted in Fig. 67. Values of 0.10±0.1, 0.42±0.1, and 0.3±0.1 were found at the He-Ne wavelength (632.8nm) for the samples #4, 21, and 22, respectively. This result indicates the lower laser intensity at the target gives the lower value of imaginary part of refractive index.

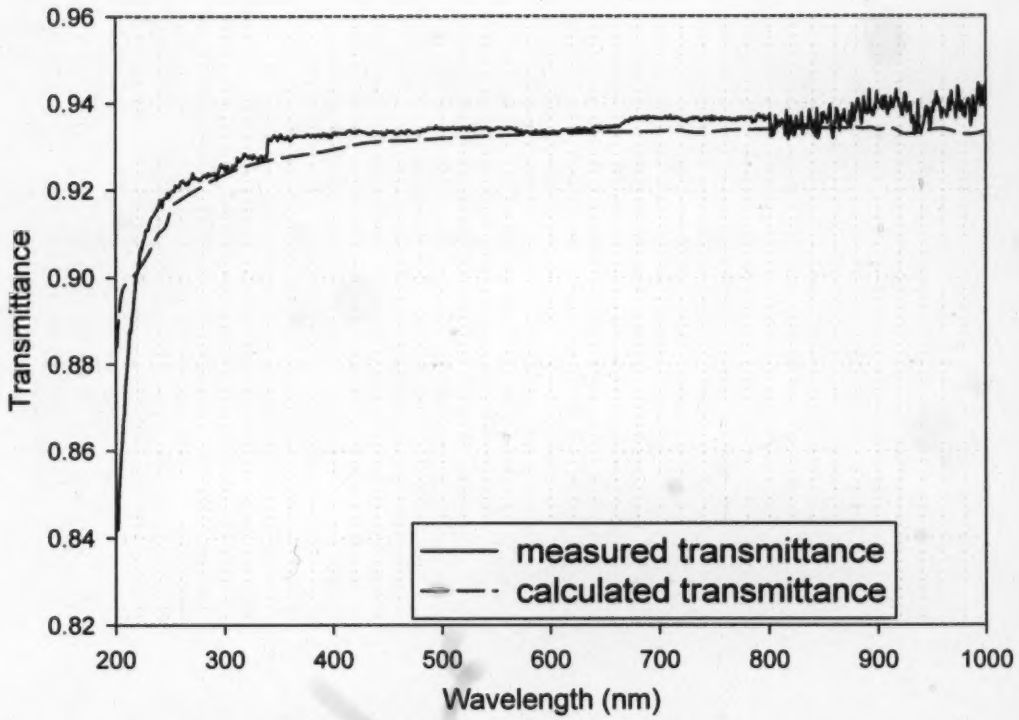

Fig. 62 Comparison between measured and calculated external transmittance of the UV grade quartz with the thickness of 3/4 inch. The jump in the measured values at 800nm is due to the detector change, and those at 340 and 680nm are due to lamp changes. The spectrum above 800nm was shifted to match that below 800nm to correct for a residual nonlinearity in the infrared detector.

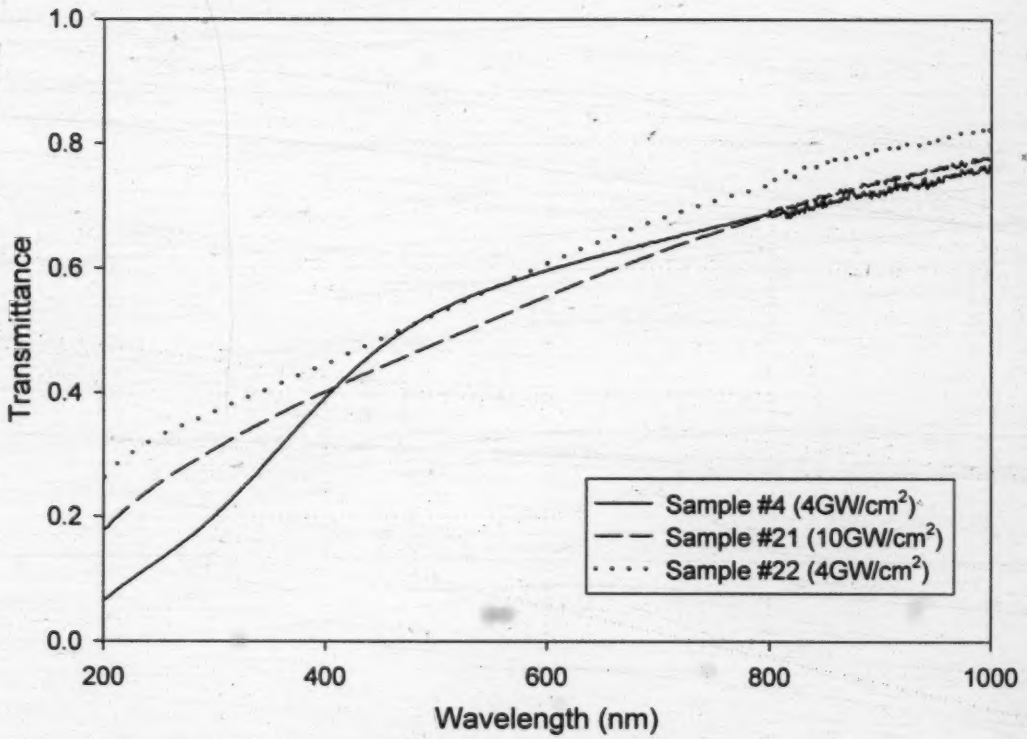

Fig. 63 External transmittance of the carbon films deposited with different laser intensities. The film thicknesses for smple #4, 21, and 22 are 70±5nm, 28±10nm, and 28±10nm. A 3/4 inch thick S1UV substrate was used for sample #4 whereas 1mm thick S1UV substrate for samples #21and #22.

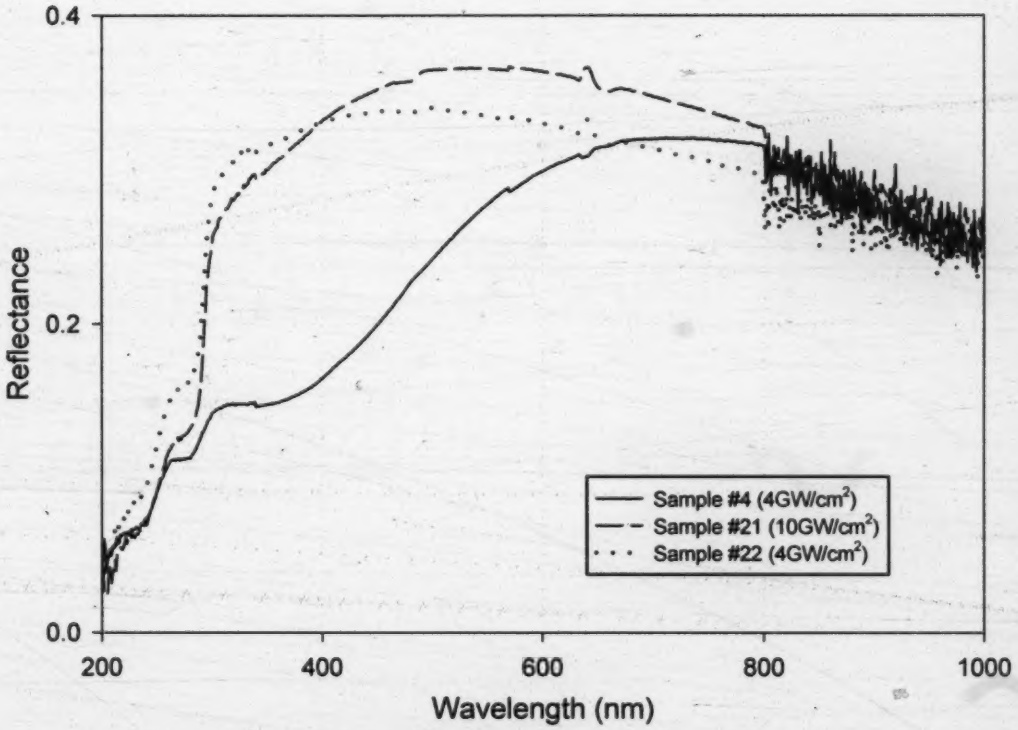

Fig. 64 Reflectance of the DLC film deposited on the quartz substrate. The amplitude modulation between 200nm and 400 nm is suspected to be due to instrumental error and not due to the Fabry Perot effect since modulation peaks are observed at same wavelength from 70±5nm thick film (Sample #4) and 28±10nm thick film (sample #21 & #22). One can find similar modulation in Fig. 62. The low transmission from sample #4 in the visible range may be due to the attenuation caused by a greater thickness of the sample compared with the others.

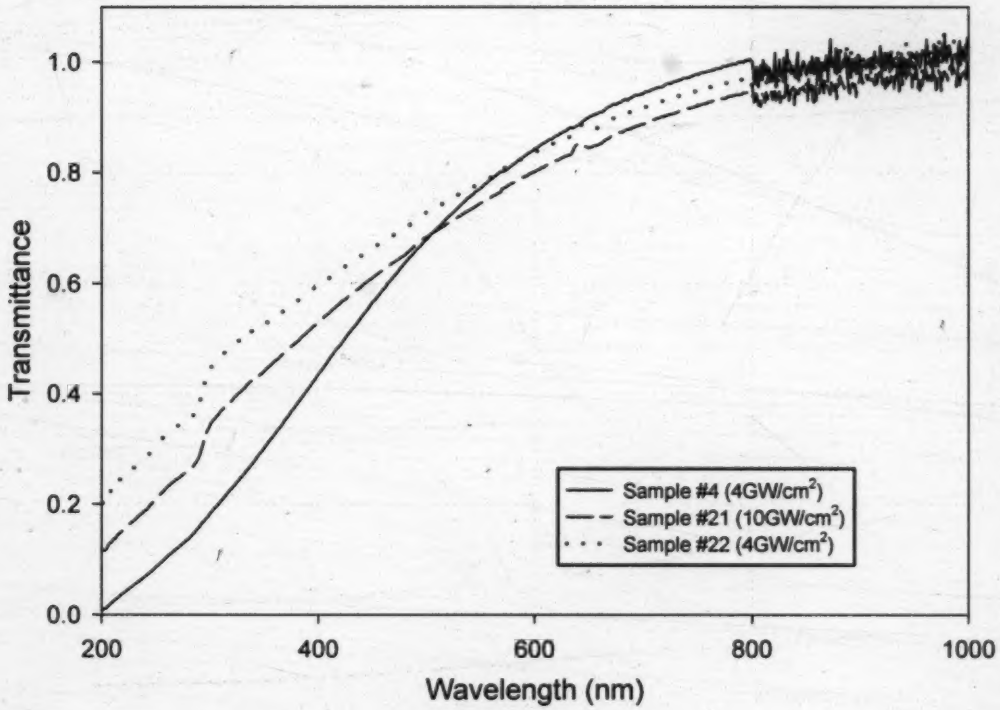

Fig. 65 Internal transmittance of DLC films.

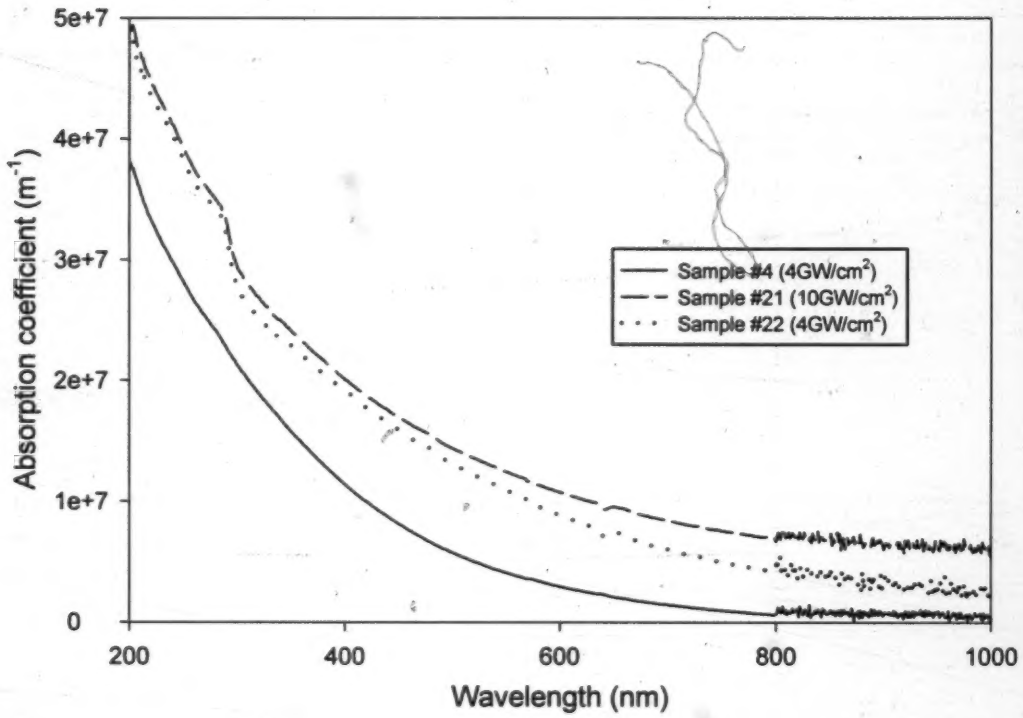

Fig. 66 Calculated absorption coefficient of the DLC films produced with different laser intensities.

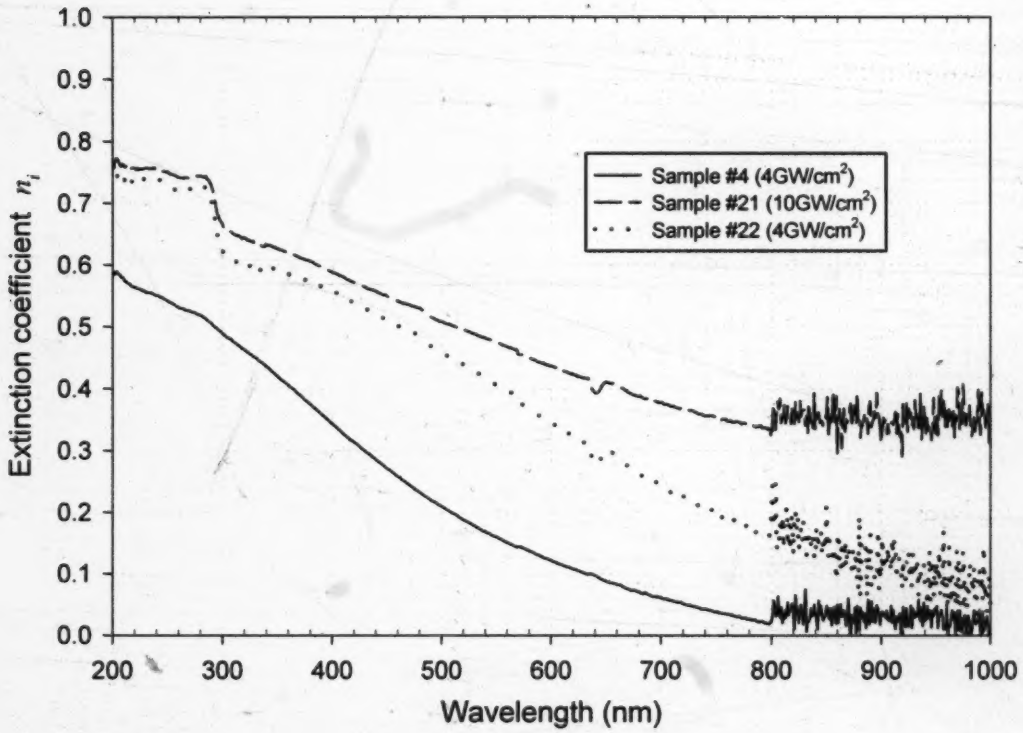

Fig. 67 Calculated extinction coefficient, n_i, of the film. Values of 0.10±0.1, 0.42±0.1, and 0.3±0.1 were found at the He-Ne wavelength (632.8nm) for the sample #4, 21, and 22, respectively.

V.4 Real Part of Index of Refraction(Refractive Index)

An ellipsometer (Gaertner L125B), which is available in the Thin Film Engineering Laboratory, was used to determine the real part of the index of refraction of the film. A polarized HeNe laser is used as the incident lightwave in the ellipsometer we used. The computer program from the ellipsometer instrument was used to process the data. We used the program with single layer absorption model for processing the data. In the program a fixed value of the real part of index of refraction and estimated value of imaginary part of index of refraction at the wavelength of He-Ne laser (632.8nm) and the film thickness are required as inputs. For the estimated value of the refractive index, we chose a starting values in the range of 1.5 to 2.4, which are covering typical values for DLC (1.8 ~2.2), as given by Ogale et al [19]. Profilomter measurements were employed for the estimated thickness at the measurement points. Since the program returns the imaginary part of the refractive index and thickness based on those estimated values and the fixed value of the refractive index, we changed the fixed value over multiple measurements, and the combination of the a real and imaginary part of the refractive index which gives the least deviation of thickness with respect to the values obtained from the profilometer measurement was chosen as an answer.

Measurements were conducted for the films made with magnetic guiding on different substrates. First we examined the film made on a Si substrate (sample #23) as shown in Fig. 68. The thickness of the film at point1 (thickest part) was measured by the profilometer at AMC and was found out to be 225 ± 20nm. Based on this initial information, we took multiple measurements with different values of the real part of refractive index of 1.5 to 2.4 which is typical for films made by the conventional PLD

technique. The initial estimates of 0.1 for the imaginary part of the refractive index which was chosen based on the value (0.12±0.1) obtained for the sample made with conventional PLD technique (sample #4) and the thickness of 225nm were input to the ellipsometer program. As a result, we found a very high index of refraction (real part) of 2~2.3, which is more than 80% of the value for diamond (2.42) and the imaginary part of refractive index of 0.03~0.11. It was found that the real refractive index drops and imaginary refractive index increases as the distance from the point 1 increases. Measurement results are summarized in Table 7. Measurement was also taken for the sample produced with conventional PLD, but the result turned out to be inconclusive.

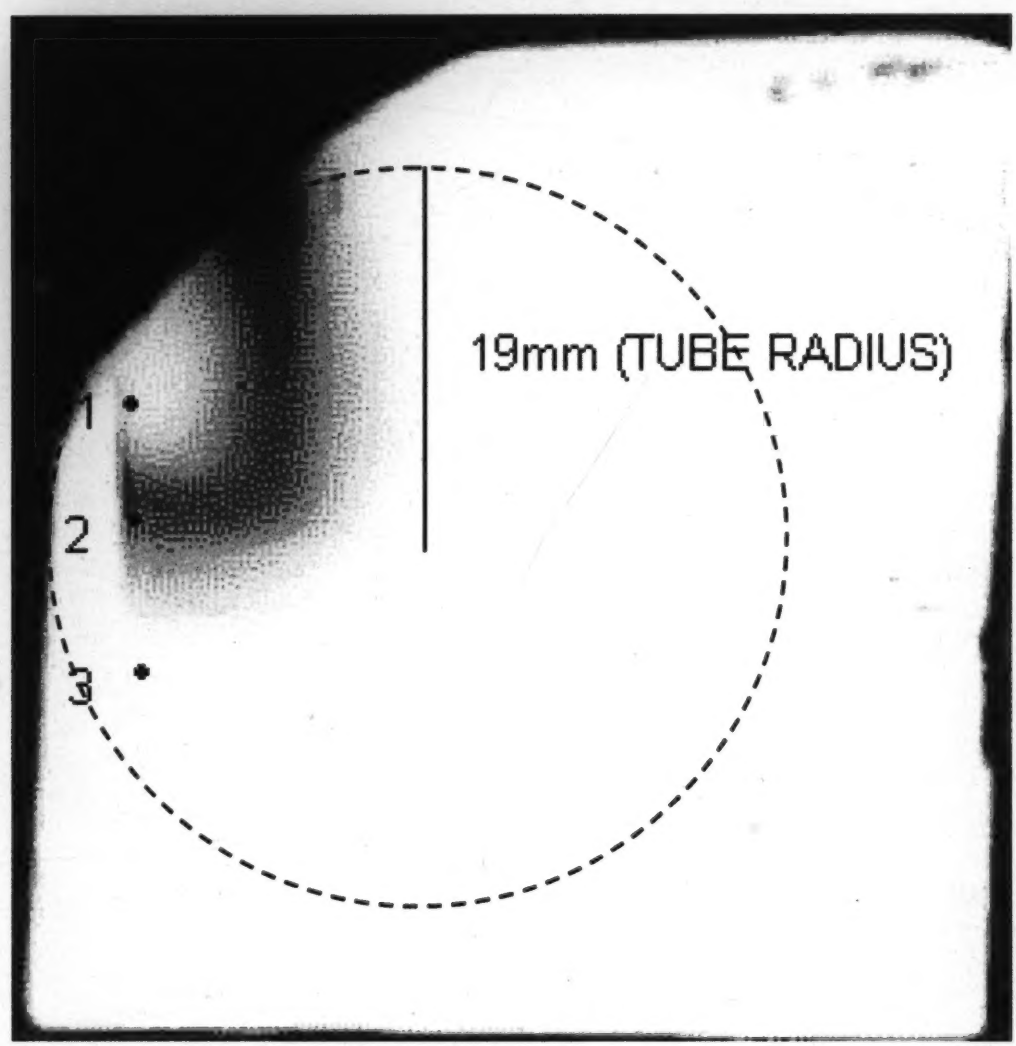

Fig. 68 Visual photograph of carbon film fabricated on silicon (100) substrate (sample #23) by magnetic guiding with a curved 46±1cm long coil geometry. The sample was illuminated by a diffused white light source in order to show the color shift of the film due to the variation of the film thickness. The length of the black line in the picture is approximately equivalent to 19mm, which is the inner radius of the guiding tube. The center of the tube was located at the lower end of the black line. About 3mm of the left end of the substrate was covered with a mask during the coating run. The substrate was placed about 20±5mm away from the exit of the solenoid. Ellipsometer measurements are taken at three points where indicated with black dots. The distances of the dots from the edge of the sample are 2±0.5mm, 8±0.5mm and 15±0.5mm, respectively.

Table 7 Summary of the optical properties of the carbon film produced on Si(100) substrate by B-field plasma guiding PLD method (sample #23) measured at the different points on the sample as shown in Fig. 68.

	Distance from point1 (mm)	Thickness (nm)	Refractive index (real)	Refractive index (imaginary)
Point 1	0	225±20	2~2.3	0.03~0.11
Point 2	6	55±20	2~2.2	0.1~0.2
Point 3	13	35±20	1.6~1.9	0.1~0.2
No b-field (sample #4)	-	-	Inconclusive	0.12±0.1
Diamond	-	-	2.42	$<6*10^{-6}$

V.5 Optical Gap Measurement

A Tauc plot as described in II.2.2 was employed to determine the optical gap of the DLC sample. Fig. 69 shows the Tauc plot for the DLC film produced by the normal PLD technique with different laser intensities. The angle of deposition with respect to the sample normal was 20 degrees for both samples. The optical gap of sample #21 produced with the laser intensity of 10GW/cm^2 was found to be 0.68±0.2eV. Also, the optical gap of sample #4 and #22 produced with the laser intensity of 4GW/cm^2 was found to be 1.23±0.2eV and 1.01±0.2eV, respectively. Therefore, an increase of the optical gap of approximately 0.4eV was observed when the laser intensity at the target was decreased from 10GW/cm^2 to 4GW/cm^2. The samples made by the B-field guiding PLD technique were not measured because they did not have a uniform film thickness over the measurement area of 10mm diameter. The step in the Tauc plot around 4 to 6 eV was caused by the instrumental error as the instrument changes lamps. These results are within the range of the typical values for the optical gap which usually lie in the range from 0.4 to 1.5eV for MSIB [42]. The highest reported optical gap for non-hydrogenated DLC is 3.5eV, which was reported by McKenzie et al by using the cathodic arc apparatus shown in Fig. 12.

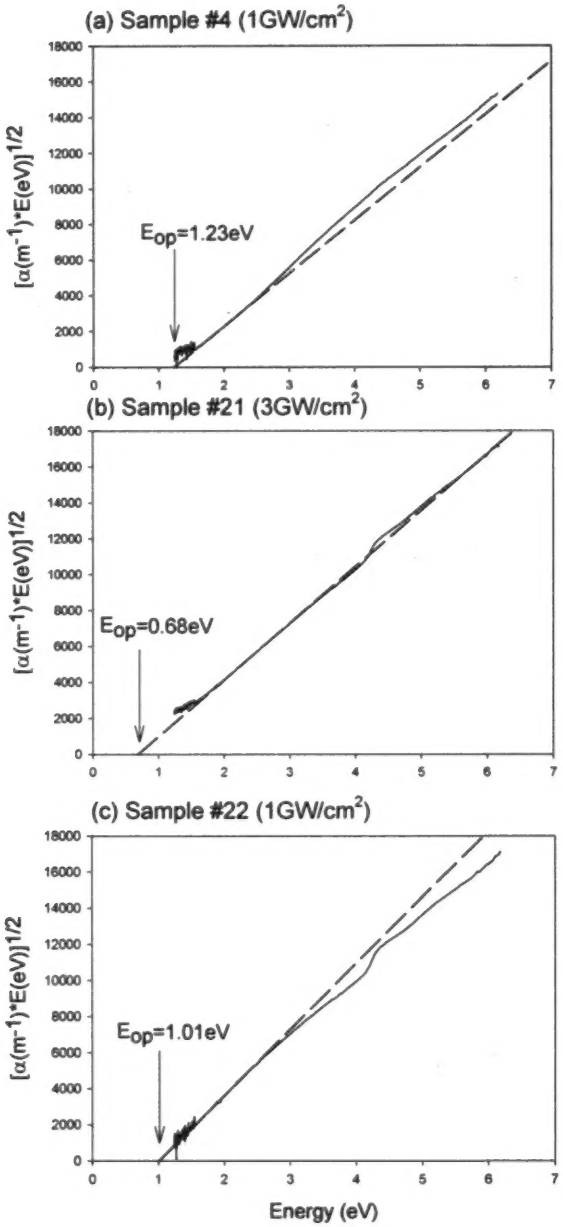

Fig. 69 Tauc plot for the DLC films deposited with the different laser energy flux of 4GW/cm^2 (sample #4-(c) and 22-(e)) and 10GW/cm^2 (sample # 21-(e)). The best linear fit for each plot is shown with a dashed line. An increase in the optical gap was observed for the lower laser intensity. The accuracy of the optical gap shown in the figure is ±0.2eV. The increased noise level below 1.5eV is due to the change to a less sensitive infrared detector.

V.6 Stress measurement

Stress was measured for samples made with the normal pulsed laser deposition technique at intensities of 10GW/cm^2 and 4GW/cm^2. The deflection of the quartz strip was measured after the deposition by taking profilometer measurements in the middle of the strip over the length of 1 to 2 mm. The thickness was also measured by the profilomter. Compressive stress of around 0.3 to 0.4 GPa was observed for both samples as shown in Table 8. Comparing to previous reports in the literature in most case stress is compressive and varies from –1 GPa (tensile) to 5 Gpa. It seems that ion sources with higher kinetic energies give a lower stress [42,50]. The highest stress of 8GPa was reported by McKenzie et al [41].

Table 8 The result of the stress measurements taken for the films produced by normal PLD with different laser intensities.

Laser intensity (GW/cm^2)	Deflection (nm)	Scanned length (μm)	Stress (GPa)	Type of stress
3 (sample # 21-(e))	36±4	2000	0.38±0.14	Compressive
1 (sample # 22 (e))	35±5	2000	0.31±0.10	Compressive

V.7 Resistivity measurement

A resistivity measurement was conducted for a 30±10nm thick DLC film coated on a copper substrate (sample #7-(e)) by simply measuring the resistance along the depth direction as explained in II.3.1. By using the measured resistance of 5~15Ω and thickness and approximate contact area of 1±0.5mm^2, the resistivity was found to be on the order of 10^3 to 10^4 Ωm. This value is rather low since usually at least 10^6 Ωm is required for a carbon film to be regarded as a DLC. However, this low resistivity may be attributed to tunneling current, leakage current through voids, or extra holes or electrons given by contaminants. DLC films thicker than 100nm with strong adherence to the metal substrate should be made for more accurate measurements.

V.8 SAW Measurement

Detection of SAW signal from the DLC samples turned out to be a difficult task. First of all, it was difficult to generate reasonable signal amplitude without damaging the film. The laser intensity for the damage threshold for the 70±5nm thick carbon film fabricated with the laser intensity of ~4GW/cm^2 (sample #4) was less than 0.5MW/cm^2, which is significantly smaller than with other materials (e.g. more than 10MW/cm^2 for Si). In order to obtain reasonable signal amplitudes the ablation excitation regime was required with the current setup. With ablative excitation, one could obtain on the order of 10~50 times bigger signals than those generated by thermal expansion. However, multiple ablative shots eventually causes significant damage of the irradiated region altering the signal observed. Fig. 70 shows the SAW signals generated by ablation of the film and Fig. 71 shows their spectrum. For measuring signals shown in Fig. 70, less than half the maximum possible input energy was chosen in order to obtain reasonably similar waveforms for a few tens of shots which is necessary for determining spectral phase shifts. The spectral content of the signal ranged up to 170 MHz. However, strong attenuation at the frequency regions below 20MHz, in the range of 40~60MHz, and above 170MHz deteriorated the phase information in these regions leading to discontinuities in the phase information. Also a noise peak at around 8MHz which came from electromagnetic pickup of laser discharge noise made the determination of the velocity in the lower frequency region almost impossible. Nevertheless, the generally observed positive slope of the dispersion curve as shown in Fig. 72 indicates that the velocity of Rayleigh wave in the carbon film examined is significantly greater than that of substrate

material Si. The shear velocity in the film must be greater than that in the substrate (i.e., $v_t > V_t$). Substituting the equation (18) to the left side of the condition, one could calculate the minimum value of the Young's modulus of the film to have a positive dispersion curve. For the DLC film deposited on Si (100) substrate, it was found that the Young's modulus of the film should be more than 170 GPa. Due to the poor quality of the data no more accurate analysis was attempted for this measurement.

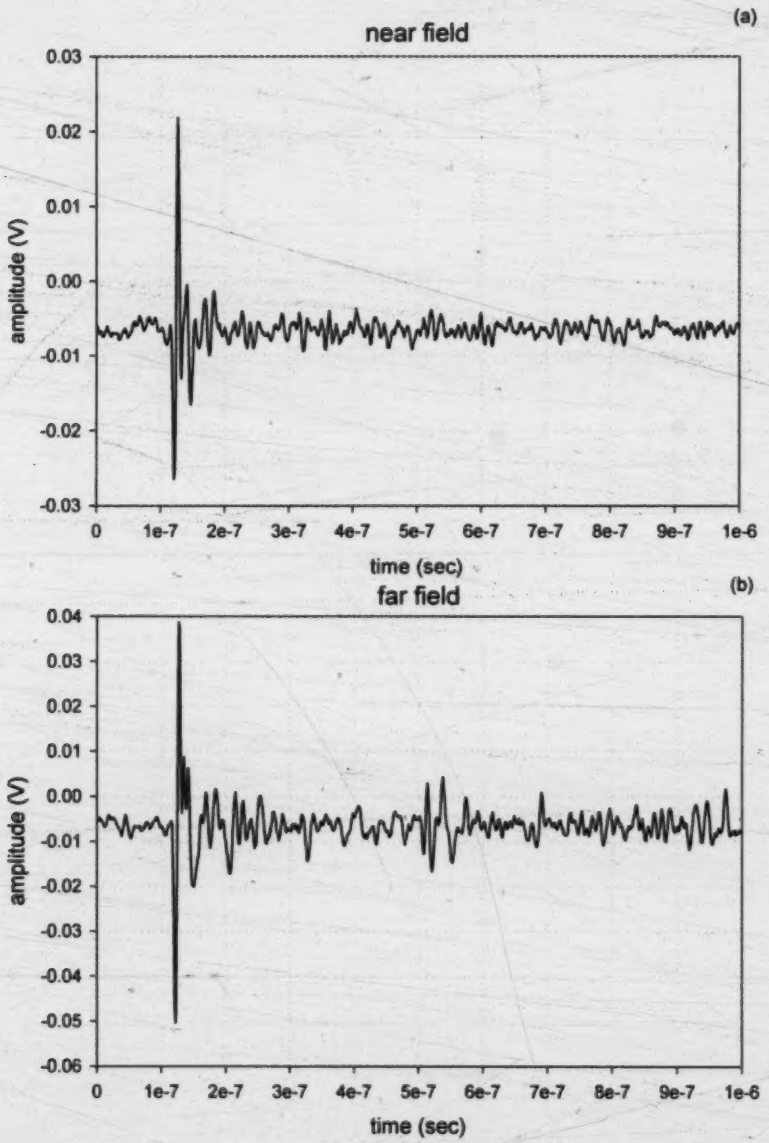

Fig. 70 SAW signals detected on a 70±5nm thick DLC film on a (001) silicon substrate. The approximate distance from the line source to detector for signal (a) was 3±0.5mm. The signal at (b) was detected at a distance of 762±10μm further than that of signal (a). A part of the laser beam was clipped by the metal housing of the SAW transducer when the near field signal was detected, resulted in the smaller peak amplitude compared with that of far field. For the near field signal 32 shots were averaged while for the far field signal 16 shots were averaged. A 15ns KrF laser pulse was used to excite the signals.

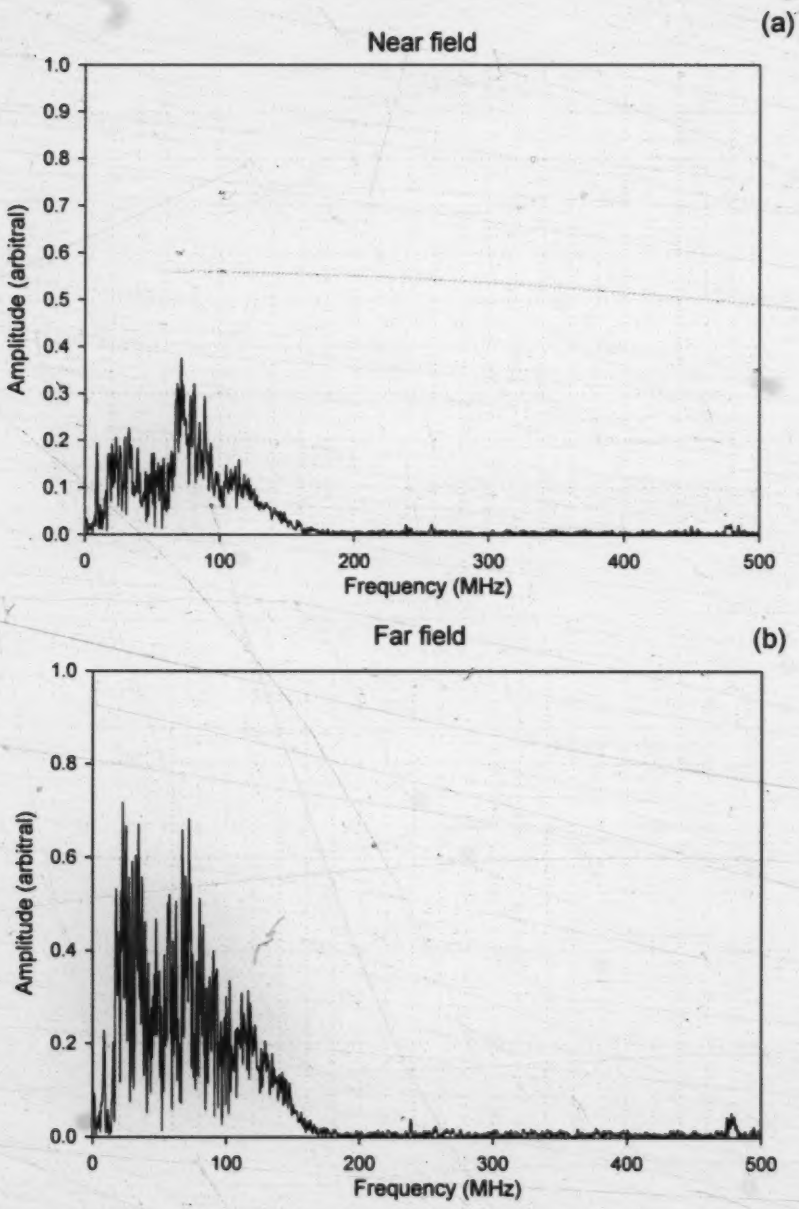

Fig. 71 Frequency spectrum of the signals shown in Fig. 70.

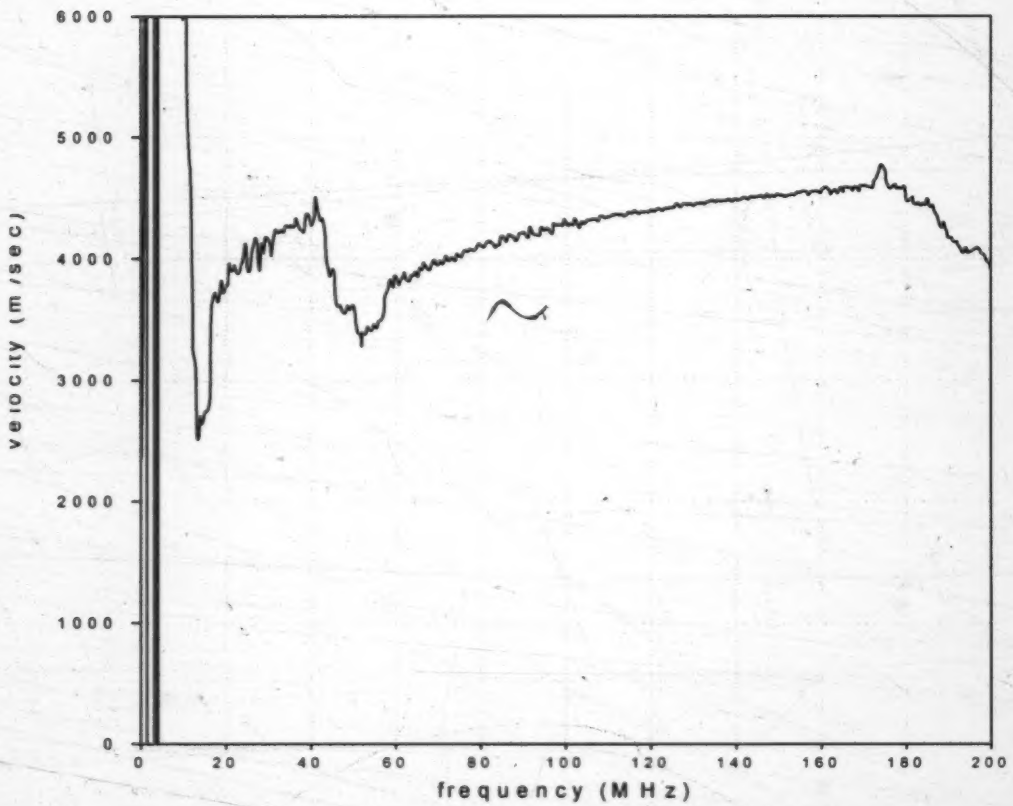

Fig. 72 Dispersion Curve Obtained for the 70±5nm thick DLC deposited on (001) Si substrate from the signal shown in Fig. 71. The generated positive slope of the dispersion curve indicates that the velocity of Rayleigh wave in the carbon film examined is greater than that of substrate material Si. Large vertical steps in velocity in several frequency regions appeared due to the poor phase information in the frequency regions where S/N ratio is low.

V.9 Measurement of sp^3/sp^2 Ratio

PLD carbon films fabricated with different laser intensities were examined by EELS (Electron Energy Loss Spectroscopy) with the help of Marek Malac using the facilities of Dr. Egerton in the Department of Physics, University of Alberta. Fig. 73 and Fig. 74 show some examples of the electron energy loss spectra due to the 1s to L shell transition for carbon. Since the uncertainty of the energy scale was on the order of 5 eV, we fixed the energy scale after the measurement by using the fact that the π absorption peak is located at 285 eV. In order to find the peak position a Gaussian curve for the π-peak was fit to the spectrum. From the figures it can be seen that there is a reduction in sp^2 peak amplitude for the lower laser intensity and with the use of the magnetic guiding field. The sp^2 fraction of a material can be determined using the following procedure [76]. First of all, we assume the whole spectrum is composed of a π-spectrum with a peak at 285eV and a σ-spectrum consisting of a steep rise around 289eV. Secondly, we assume the π-spectrum is Gaussian and the σ-spectrum is the reminder of the whole spectrum minus the π-spectrum. These functions are used to find the best fit visually to the data spectrum. Thirdly, we determine the ratio of the area under the π-spectrum to the area of the whole spectrum and we assume that this number is proportional to the sp^2 fraction of the sample. Applying the above procedure to a DLC data spectrum and a graphite reference spectrum which has 100% sp^2 fraction, the sp^2 fraction of the DLC spectrum can be determined using the relation below

$$f_{sp^2} = \frac{A_\pi(DLC)/A_{\pi+\sigma}(DLC)}{A_\pi(graphite)/A_{\pi+\sigma}(graphite)} \qquad (39)$$

In the above relation, A_π *(DLC)* represents area under the π-spectrum of the DLC sample. Once the sp^2 fraction of the DLC sample is found the sp^3 fraction can be obtained by subtracting it from unity. Ideally we should obtain a reference graphite spectrum using the same TEM that we used to obtain the other data. However, due to the difficulty in making an amorphous graphite sample with a thickness of a few tenths of nanometers placed on a copper grid, reference graphite spectra from the literature were employed instead. The three graphite spectra from Zaluzec [77], Pregliasco [76] and Fallon [44] are shown in Fig. 75 as examples of the variation in the literature data. The significant difference in the shape of the spectra is mainly caused by the different energy dispersion for each measurement which usually was indicated by the FHWM of the Zero loss spectra. The energy dispersion of Fallon's spectrum is 0.7eV while those for our spectrum is 1.45±0.1eV. The energy dispersions for Zaluzec and Pregliasco are not specified in the literature, however, should be more than 0.7eV. For quantitative analysis, the K-edge spectra can be deconvolved as shown in Fig. 76 into its Gaussian π-spectrum and remaining σ-spectrum. An example of such a deconvolution carried out by Pregliasco [76] for an amorphous carbon spectrum is shown in Fig. 76(b). In similar fashion we have deconvolved spectra for the $0.7GW/cm^2$, $4GW/cm^2$, $10GW/cm^2$ irradiation intensities and magnetic guiding case and the results are shown in

Fig. 77 (a)-(d). The calculation of sp^3 fraction depends on the reference graphite spectrum chosen. We used Pregliasco's graphite spectrum for the reference since the shape of the σ-spectrum as shown in Fig. 76 matches reasonably well with those obtained for our spectra shown in Fig. 77 and it falls in the middle of the three published graphite

spectra. In this case $A_{\pi}(graphite)/A_{\pi+\sigma}(graphite)$=0.068 was obtained with the integration range of 280 to 315eV. It should be noted our spectrum is not corrected for the secondary scattering. The resultant sp^3 fractions of each case are summarized in Table 9.

The energy loss peaks due to the π plasmon and $\pi+\sigma$ plasmon were also observed in the low energy regions. Fig. 78 and Fig. 79 show some examples of the electron energy loss spectra due to the plasmon absorption. In these figures the zero loss peak was subtracted by using the curve fit program which is built in the software for the EELS system. For carbon films, the peak position of the $\pi+\sigma$ plasmon peak can be used to estimate the fraction of sp^3 bonding as shown in Fig. 80 [44]. Unlike the K-edge absorption peak, there was no significant energy calibration error since the zero loss peak is always in the same measurement. Therefore the peak position can be determined within a few hundredths of an eV. Examination of the peak position gives an estimation of the sp^3 fraction for each sample. However generally the plasmon peak position is not considered a reliable indicator and the K-edge method is preferred [78].

Results are summarized in Table 9. The deposition angle refers to the angle between the substrate normal and the direction of incidence of the coating species. The sp^3 fraction ranges from 27~40% as estimated from K-edge spectra for the various samples whereas the sp^3 fraction ranges from 1~23% from the plasmon peak shifts. Although there are 10 to 20% discrepancies between the sp^3 fraction obtained with K-edge spectra and plasmon peaks, higher values for the samples with the lower laser intensities and with the use of magnetic guiding field were observed. These values should be confirmed by using a graphite calibration spectrum obtained from the same EELS system used for the present measurements. The typical sp^3 fractions of 27 to 40%

would indicate that the films produced are still not close to the optimum values which can be obtained using PLD where sp^3 fraction of up to 85 % have been reported [82].

Overall the discrepancies in sp^3 fractions will need further measurements to resolve.

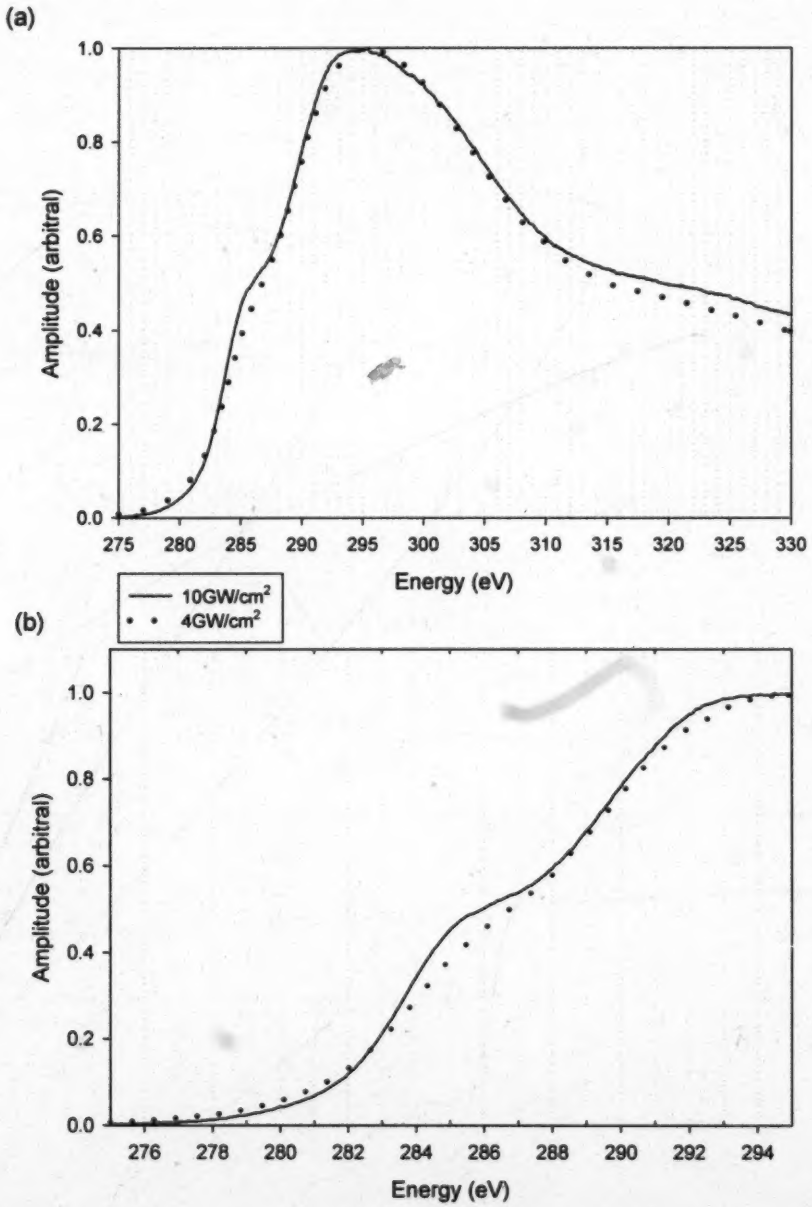

Fig. 73 K-edge absorption peak for the carbon films produced with conventional PLD technique with different laser intensities (4.0 and 10.0 GW/cm^2 (sample # 7-(f) and 21-(c), respectively). Reduction of the π-peak was observed for the lower laser intensity. (a) full energy range (b) magnified plot in region of the π-peak.

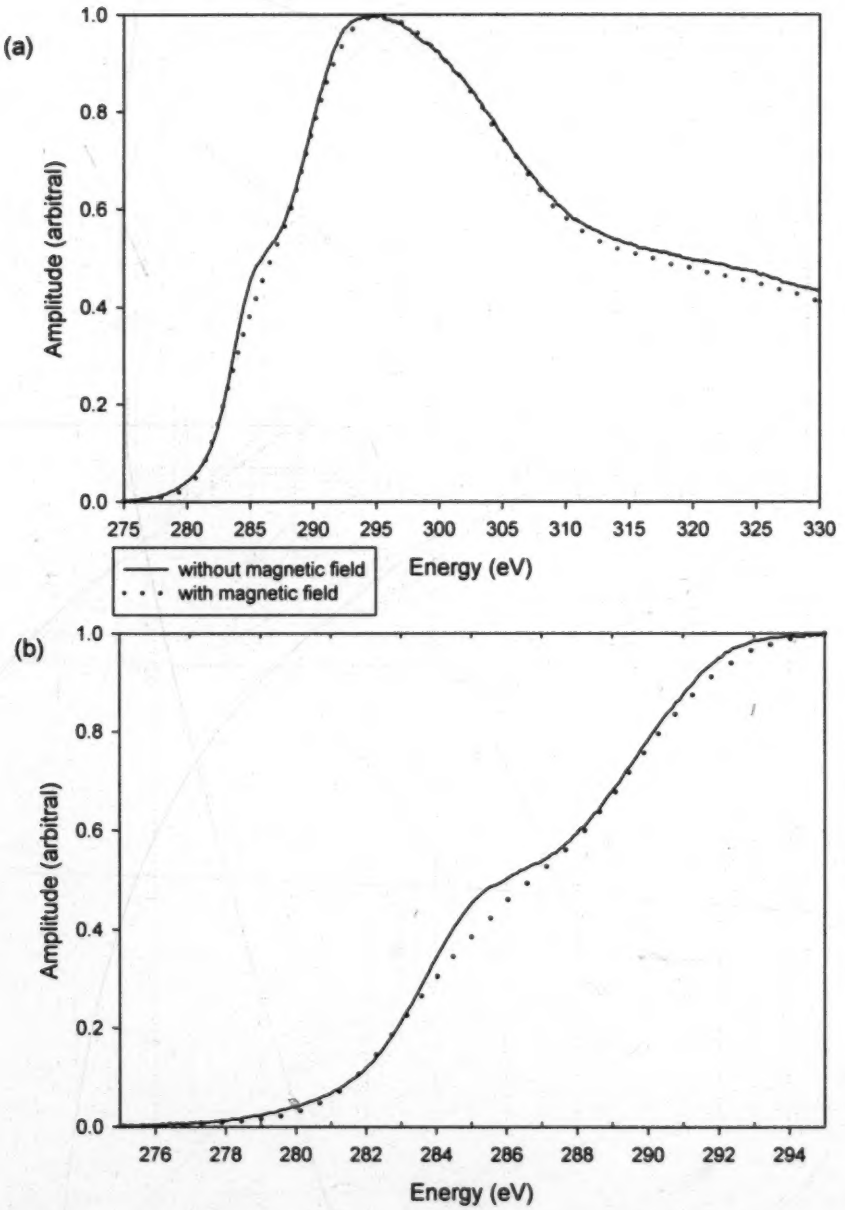

Fig. 74 K-edge absorption peak observed from the sample made with conventional PLD technique (sample #21-(c)) and PLD with magnetic guiding system (sample #18-(a)) at an intensity of 10GW/cm^2. Reduction of the π-peak amplitude was observed for the latter sample. (a) full energy range (b) magnified plot in the region of the π-peak.

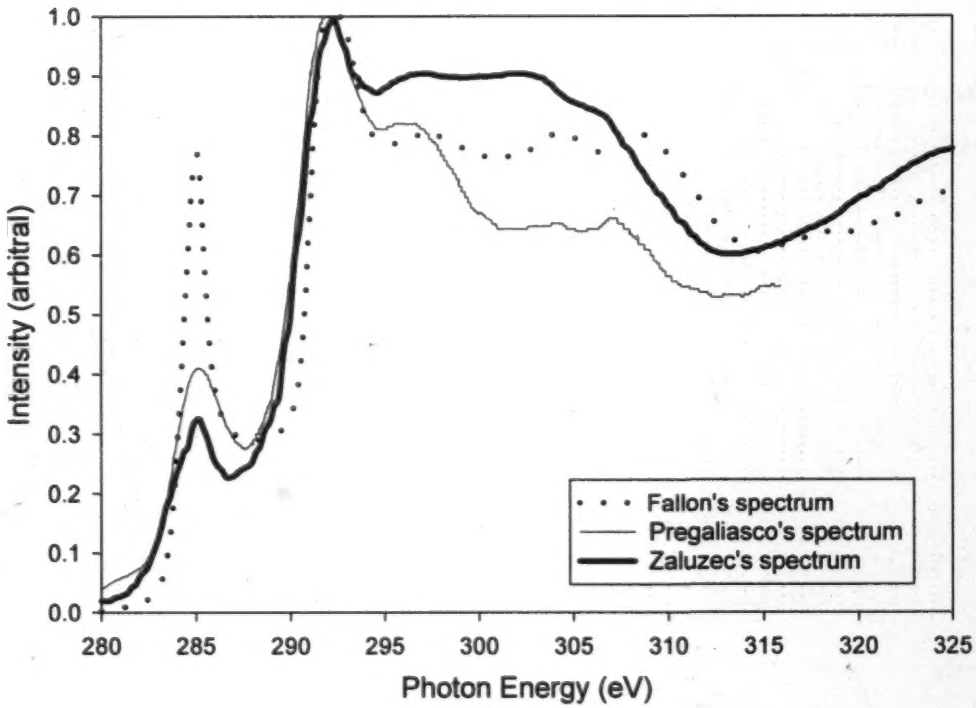

Fig. 75 The graphite spectrum regenerated from the literture published by Fallon [44], Pregliasco [76], and Zaluzec[77]. Pregliasco's spectrum was employed for the quantitative estimation of sp^3 fraction.

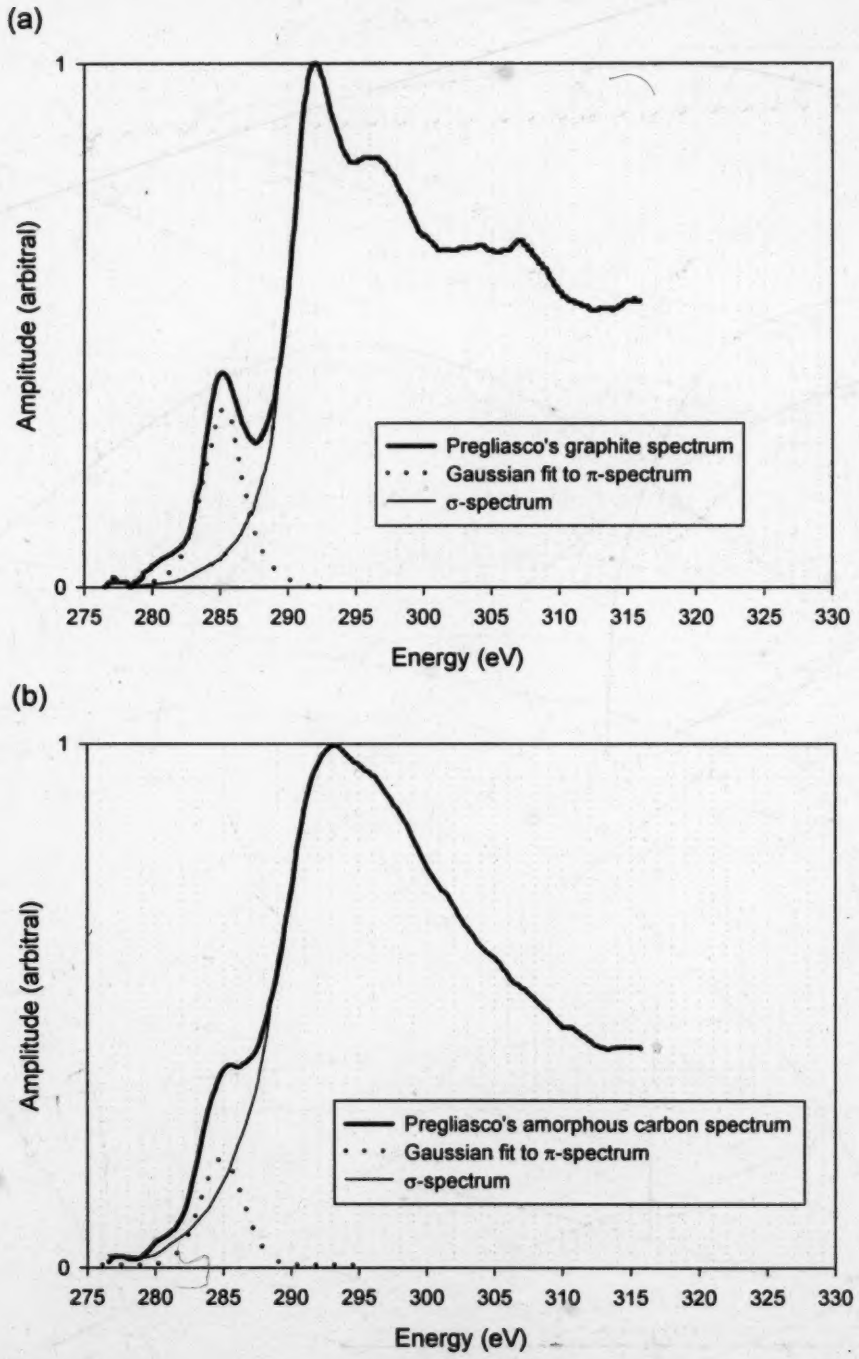

Fig. 76 Graphite and non-hydrogeneted amorphous carbon spectrum taken by Pregliasco [76]. Data were deconvoluted for the quantitative analysis.

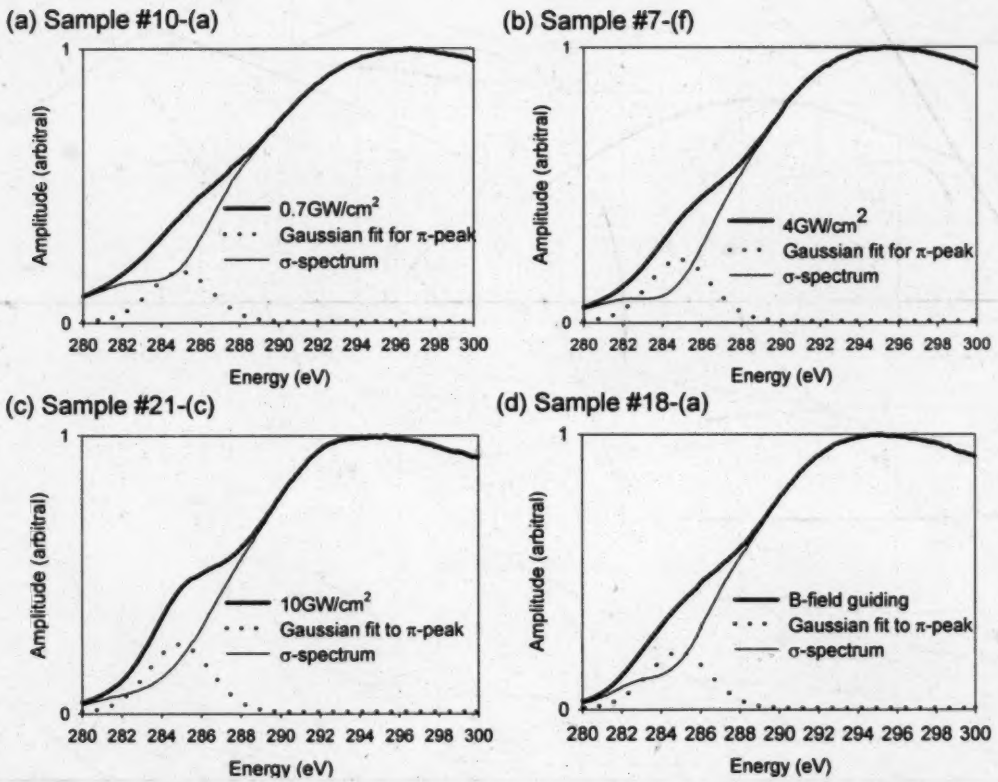

Fig. 77 π-peak fits obtained from the various carbon samples fabricated with different deposition conditions.

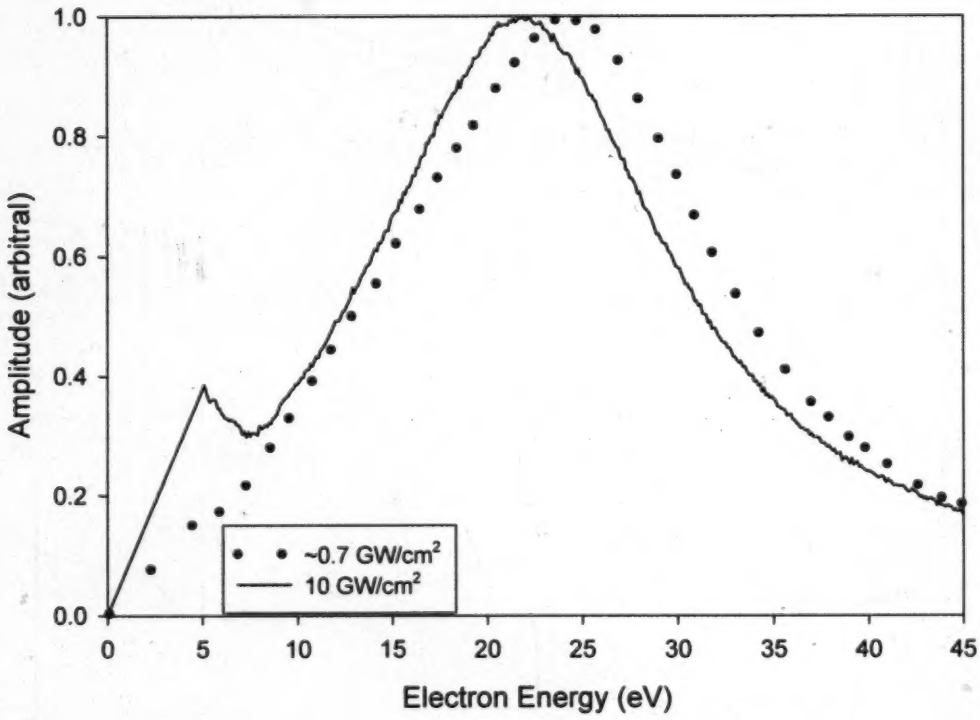

Fig. 78 π–plasmon peak (5~10eV) and π+σ–plasmon(20~30 eV) peak observed from the carbon films made by PLD with different laser intensities (10 GW/cm^2 (sample #21-(c)) and ~0.7GW/cm^2 (sample #6-(e))).

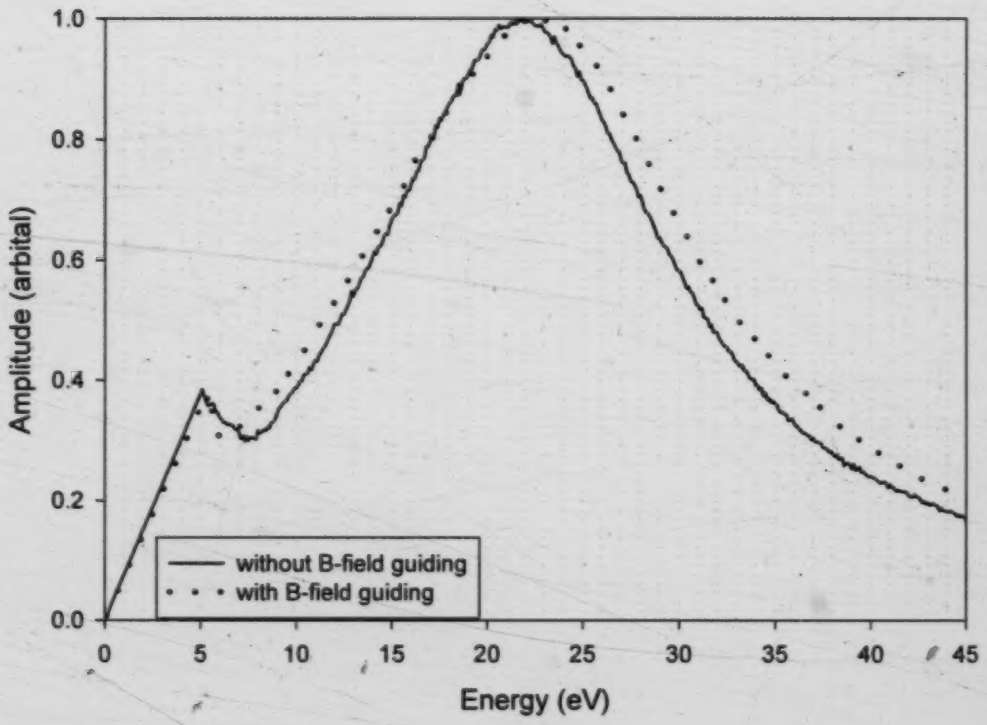

Fig. 79 π–plasmon peak (5~10eV) and π+σ–plasmon(20~30 eV) peak observed from the carbon films made by PLD with magnetic guiding (sample #18-(a)) and without magnetic guiding (sample #21-(c))with the laser intensity of 10GW/cm^2.

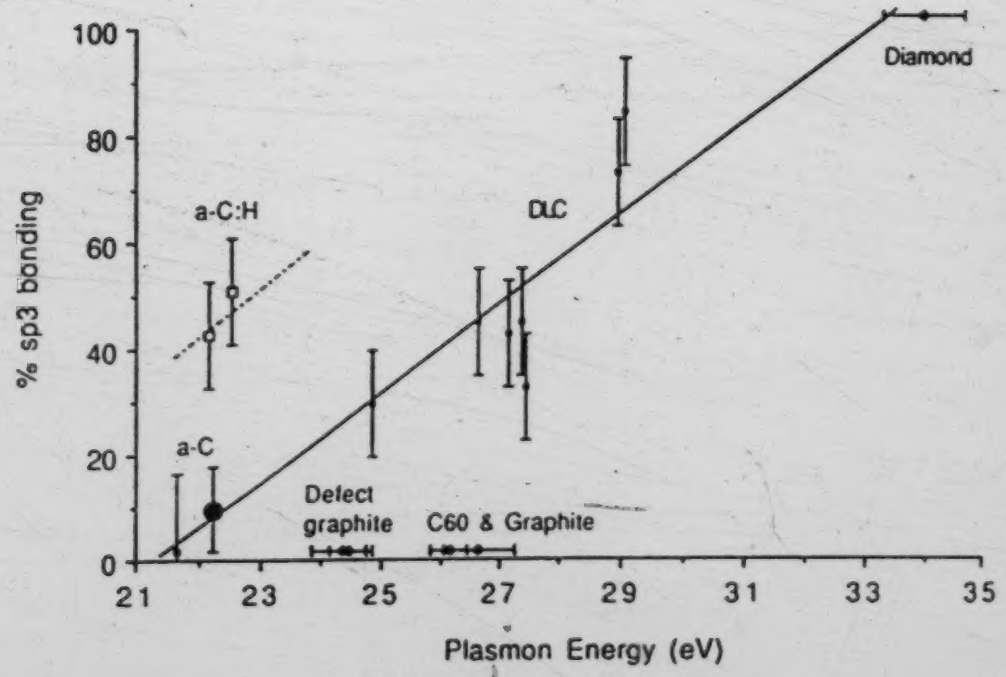

Fig. 80 Percentage of sp^3 bonding(measured from the C-K 1sp* transition) as a function of plasmon energy (position of the π peak from the energy loss spectrum) for different forms of carbon The solid line indicates the general trend for nonhydrogenated carbon films. The presence of hydrogen lowers the film density and plasmon energy (dotted line). The large filled circle at the bottom left represents grain-boundary amorphous carbon [44].

Table 9 Fraction of sp^3 for the samples deposited with different deposition conditions estimated from the plasmon peak position and K-edge absorption peak.

Sample & Substrate #	Laser intensity & presence of the magnetic field	Deposition angle (degree)	Distance (cm)	Plasmon peak position (eV)	sp^3 fraction measured by plasmon peak	sp^3 fraction measured by K-edge peak	comment
3-(b)	4GW/cm^2	NA	NA	22	9±9%	NA(sp^2 fraction of 189%)	Too large energy dispersion (~3eV)
6-(e)	~0.7GW/cm^2	30	6	24	23±10%	38±30%	
7-(f)	4GW/cm^2	30	6	22	9±9%	32±30%	
8-(b)	4GW/cm^2	0	15	22	9±9%	31±30%	
10-(a)	0.7GW/cm^2	0	15	23	15±10%	40±30%	
18-(a)	10GW/cm^2 (B-field)	-	46	23	15±10%	38±30%	Center of plasma
18-(b)	10GW/cm^2 (B-field)	-	46	19.5	1+10% -1%	27±30%	Edge of plasma
21-(c)	10GW/cm^2	30	6	22	9±9%	27±30%	

VI Results and Discussion

VI.1 Film properties

The properties measured for the films produced in the present study indicate that the quality of the films is not as high as has been reported in previous studies of PLD of diamond like films. In the present study the sp^3 fraction observed from the samples produced with conventional PLD (27±30~40±30%) was smaller than the results from other research groups (Fig. 27). The film densities observed ranged form 1.3 g/cm^3 to 2.3 g/cm^3 without magnetic guiding as compared to typical optimum values of 2.8 g/cm^3 reported in previous references [50]. The optical gap observed for our lower quality films ranged from 0.68 eV to 1.23 eV which is considerably lower than optimum value of 1.5 eV reported in [79] for MSIB of diamondlike films. This indicates that experimental conditions still needed to be optimized. However, improvements in the quality of the film were observed by decreasing the laser intensity and by guiding the plasma with curved magnetic coil.

The effect of the laser intensity was observed for the density estimated from the plasmon peak, energy gap estimated from the Tauc plot, and fraction of the sp^3 estimated from the K-edge absorption peak. All film properties are improved for the lower laser intensity. However, this doesn't agree with the intensity scaling reported by Davanloo et al [80,81] when Nd:YAG laser (1.06μm wavelength) deposition is employed. Davanloo claims the fraction of sp^3 ratio should increase when the laser intensity is increased from 10^{10}W/cm^2 to 10^{12}W/cm^2 when a YAG laser is employed. However, in previous work

using a KrF laser Pappas claims this threshold for good DLC coatings can be reduced down to $10^8 W/cm^2$ when with the fluence of 3.1 J/cm^2 as determined from the size of the craters [82]. In the present results, it is found that, for the conventional PLD a greater fraction of the sp^3 bonding is obtained when the laser intensities are reduced to $\sim 10^9 W/cm^2$, which should lower the kinetic energy of ions in the plasma. However, our intensities may still be somewhat higher than those used by Pappas et al.

When magnetic guiding was employed, we found a better optical quality and higher density in the central region coated with higher plasma density. However, no significant difference in ion energies is expected between the central and outer regions. This implies higher plasma density may be a key factor in the coating quality. At the same time without the magnetic guide field, lower intensities are expected to produce a larger density of neutral plasma plume particles which may be a factor in producing better coatings. These results may indicate that the total energy flux incident on the surface with each laser shot may be an important parameter perhaps leading to scrubbing of non sp^3 bonded species.

The present study has lead to the development of number of characterization techniques for diamond like carbon coatings. The initial results presented in this thesis indicate some improvements in film properties with magnetic guiding as compare to the traditional PLD produced films. This is encouraging in that the film properties with magnetic guiding when optimized could potentially be as good as or better than those produced by conventional PLD. Further work will be required to fully optimize and characterize such coatings.

Table 10. Summary of the properties for each sample

(a) without magnetic field guiding

Laser Intensity (GW/cm^2)	Density (g/cm^3) from the plasmon peak	Fraction of sp^3 (from Fig. 80)	Fraction of sp^3 (from K-edge)	Extinction Coefficient at λ=632.8nm	Optical gap (eV)	Stress (GPa)
10	1.6±0.3	9±9%	27±30%	0.3±0.1	0.68±0.2	0.38±0.14
4	1.6±0.3	9±9%	32±20%	0.12±0.1	1.23±0.2	0.31±0.10
0.7	1.7±0.3	15±10%	40±30%			
~0.7	2.0±0.3	23±10%	38±30%			

(b) with magnetic field guiding

Laser Intensity (GW/cm^2)	Density (g/cm^3) from the plasmon peak	Fraction of sp^3 (from Fig. 80)	Fraction of sp^3 (from K-edge)
10 (center of the plasma)	1.7±0.3	15±10%	38±30%
10 (edge of the plasma)	>1.3 (porous?)	1+10% -1%	27±30%

VI.2 Performance of broadband SAW transducer

Part of the present investigation was the development of a surface acoustic wave diagnostic technique for the measurement of Young's Modulus of the thin films. While initial tests appeared promising a number of problems arose when trying to measure the diamond-like carbon films. In order to achieve better performance of the SAW transducer one must identify the key issues limiting the detection of the important phase information.

First of all, the wavelength we are currently using for the thermal excitation is perhaps not appropriate for the carbon film. Unlike CVD polycrystalline diamond, amorphous carbon film in general has a very large absorption coefficient in the UV region. If a KrF laser pulse is irradiated onto the surface of the film, the entire energy will be absorbed into a very thin surface region of the film due to its very short penetration depth at such a wavelength leading to ablation and damage at low fluxes. A Nd:YAG laser, which emits infrared wavelength (1060nm) radiation is available in our laboratory. Since the penetration depth at 1060nm is much longer than that of 248nm for amorphous carbon, more gentle absorption of the photon energy into the film will be obtained and thus higher fluxes can be used in the relatively low thermal excitation regions. However, this wavelength may create the opposite problem of too deep an absorption depth. The second harmonic or third harmonic wavelength of Nd:YAG may be optimum for this measurement.

A second issue would be the reduction of the effect of the electromagnetic noise coming from the discharge excitation of from the KrF laser cavity. This noise makes the phase information of the lower frequency (i.e. below 10MHz) difficult to obtain. This is

especially the case when ablation is carried out in order to obtain reasonable signal amplitude such as the case for our DLC film. This is because the number of the waveforms which can be taken at one point is limited, due to cumulative damage to the substrate. Employing a Nd:YAG laser will solve this problem to some extent as well because the Nd:YAG laser is excited by flashlamps and the flashlamp discharge voltage is only several kilovolts instead of the 40 kilovolts for the excimer laser discharge.

Another option is to simply let the signal propagate to a later time period where the effect of the discharge noise is almost gone. However, when the wave is far from the source the attenuation of the both high frequencies and low frequencies become an issue. There is no easy solution to solve high frequency attenuation because it depends on the materials. However, one can solve the problem for the lower frequency range. As mentioned in II-1.3, one of the reasons for the attenuation in the lower frequency range in the far field is due to the poor directionality of the line source radiator. However, this problem can be solved by making the line source longer. At the present moment, a linewidth of 12mm is employed for the operation. This width could be expanded to about 2-3 cm, which would allow us to detect the low frequency component of the signal at further distances. However, the sample size would have to be large enough to accommodate such a long line focus which is not the case in our present experiments. An optical detection system might also helpful in reducing the electromagnetic pick up and allowing improvements in high frequency response. Ideally this requires highly reflective films, however for the carbon film, one may have difficulty due to the low reflectance of the film.

Ringing noise in the detector has also been an issue at around 40 MHz. This may be related to mechanical vibrations in the film wrapped around the probe tip. We should try another material PVDF-TrFE, which has excellent pliability and ferroelectric properties that are superior to PVDF in order to address this problem. A thinner film (~6μm) made of this material is also available commercially. Once the detection system generates better signals, the analysis code should also be improved to avoid anomalous phase jumps of 2π which occur for rapidly varying data. Overall, the acoustic probe system with further improvement shows great promise as a diagnostic for measuring Young's modulus, a difficult to measure property of thin coating films.

VII Conclusion

Removal of particulates is a long sought after goal for pulsed laser deposition of thin films. A magnetic plasma guide developed at the University of Alberta Laser Thin Film Deposition Facility successfully reduces the population of the macro particles on the film. This result may expand the industrial applicability of the PLD technique for the fabrication of defect free thin films, although complete separation of the standard laser ablation plume into pure plasma and pure neutral particles still remains difficult. A study has been carried out to characterize diamond like carbon films produced using standard pulsed laser deposition with a KrF laser source and preliminary characterization of similar films made with a magnetic guide field has been carried out.

A laser induced surface acoustic wave (LISAW) diagnostic technique was also developed as part of this work and will be useful in the study of film parameters including Young's modulus, which is one of the important properties for DLC film. However a number of technical issues remain to be improved before the LISAW diagnostic can be used to give quantitative measurements for DLC film. These include optimization of absorption wavelength, reduction of background noise and the use of longer propagation distances. It is expected that such improvements will lead to a valuable diagnostic technique for characterization of DLC's.

The measured sp^3 fraction for our current films produced by a conventional PLD technique is in the range of 30 to 50% based on EELS diagnostics which is lower than optimized results reported in the literature. Similarly, results for optical gap in the range of 0.84 to 1.23eV and density measurement with range of 1.3 to 2.3 g/cm^3 are poorer than

results reported by other groups. These measured properties of the DLC films produced in the present study indicate that the current laser focal spot intensities and deposition conditions are less than optimum, and thus further improvement in the measured film properties could be expected with further optimization. However preliminary results from DLC produced with magnetic guiding indicates that the film properties are somewhat improved to those under similar conditions without magnetic guiding. Thus, magnetic guiding may prove to be a valuable technique for the deposition of high quality debris free films.

VIII References

1. J. Robertson, "Hard Amorphous (Diamond-like) Carbons", Prog. Solid St. Chem. **21**, 199 (1991).
2. Robertson, J., Advances in Physics **35**, 317 (1986).
3. Pierson, H.O., Handbook of Chemical Vapor Deposition (CVD), Noyes Publications, Park Ridge, NJ, 1992.
4. Bonetti, R. S. and Tobler, M., Amorphous Diamond-Like Coatings on an Industrial Scale, Roport of Bernex, Olten, Switzerland, 1989.
5. Hugh O. Pierson, "Handbook of Carbon, Graphite, Diamond and Fullerenes", Noyes Publications, 1993, p.337-355.
6. Aisenberg, S. and Chabot, R., J. Appl. Phys. **42**, 2953 (1971).
7. Aisenberg, S. and Kimock, R.M., Materials Science Forum **52&53**, Transtech Publications, Switzland, 1989, p.1-40.
8. Lasertalk, The Laser Institute, The University of Alberta (August, 1993).
9. Lasertalk, The Laser Institute, The University of Alberta (Aplil, 1995).
10. Collins, C.B., F. Davanloo, E.M. Juengerman, W.R. Osborn, and D.R. jander, Appl. Phys. Lett. **54**, 216 (1989).
11. Michael W. Geis and Michael A. Tamor, Diamond and Diamondlike Carbon, Encyclopedia of Applied Physics, Vol. **5**, VCH publishers, Inc. (1993).
12. Lettington, A.H., Applications of Diamond Rilms and Related Materials, (Y. Tzeng, et al., eds.), Elsevier Science Publishers, 1991, p.703-710.
13. Grill, A., Patel, V., and Meyerson, B. S., Applicatons of Diamond Films and Related Materials, (Y. Tzeng, et al., eds.), Elsevier Science Publishers, 1991, p.683-689
14. Tsai, H. and Bogy, D. B., J. Vac. Sci. Technol. A **5**, 3287 (1987)
15. Kurosawa, H., Nakaue, H., Mitari, T., and Yonesawa, T., Applications of Diamond Films and Related Materials, (Y. Tzeng, et al., eds.), Elsevier Science Publishers, 1991, p.319-326
16. Mirtich, M., Swec, D., and Angus, J., Thin Solid Films **131**, 248 (1985)
17. Cooper, Photonic Spectra, 149 (1988)
18. Joseph T. Verdeyen, Laser Electronics; Third Edition, Prentice Hall, Inc., 1995.
19. S.B. Ogale, A.P. Malshe, and S.M. Kanetkar, Deposition of Diamond-Like and Other Special Coatings by Pulsed Laser Ablation and Their Post-Synthesis Processing, Materials & Manufacturing Processes **8**, 19-58 (1993).
20. Singh, R.K., and J. Narayan, Physical Review B **41**, 8843 (1990).
21. Auciello, O., A.R. Krauss, A.I. Kingon, and M.S. Ameen, Scanning Microscopy **4**, 203 (1990).
22. Fujimori, S., T. Kasai, and T. Inamura, Thin Solid Films **92**, 71 (1982).
23. Wagal, S.S., E.M. Juengerman, and C.B. Collins, Appl. Phys. Lett. **53**, 187 (1989).
24. Krishnaswamy, J., A. Rengan, J. Narayan, K. Vedam, and C.J. McHarge, Appl. Phys. Lett., **54** 2455 (1989).
25. K.L Saenger, pulsed laser deposition Part 1 A review of process characteristics and capabilities, Processing of Advanced Materials **2**, 1-24 (1993)

26. S. V. Gaponov, A. A. Gudkov, B. M. Luskin, V. I. Luchin and N. N. Salaschchenko. Formation of semiconductor films from a laser erosion plasma scattered by a heated screen. Soviet Physics-Technical Physics **26**, 598-600 (1981)
27. R. N. Steftal and I. V. Cherbakov. Mechanism of condensation of heteroepitaxial A^3B^5 layers deposited by a laser pulse of moderate power. Crystal Research and Technology **16**, 887 (1981).
28. S. V. Gaponov, B. M. Luskin and N. N. Salashchenko. Homoepitaxial superlattices with nonoriented barrier layers. Solid State Communications **39**, 301-302 (1981).
29. H. Tabata, T. Kawai, M. Kanai, O. Murata and S. Kawai. Tailored thin films of superconducting Bi-Sr-Ca-Cu oxide prepared by excimer laser ablation technique. Japanese Journal of Applied Physics **28**, L823-826 (1989).
30. Marquardt, C.L., R.T. Williams, and D.J. Nagel, materials Research Society Symposium Proceedings **38**, 325 (1989).
31. Collins, C.B., F. Davanloo, E.M. Juengerman, W.R. Osborn, and D.R. Jander, Appl. Phys. Lett. **54**, 216 (1989)
32. Weissmantel, C., K. Bevilogua, D. Dietrich, H.J. Erler, H.J. Hinnenberg, S. Klose, W. Nowich, and G. Reisse, Thin Solid Film **72**, 19 (1980).
33. Spencer, E.G., P.H. Schmidt, D.C. Joy, and F.J. Sansalone, Appl. Phys. Lett..**29** 118 (1985).
34. Sato. T., S. Furuno, S. Iguchi, and Mm Hanamura, Japanese Journal of Applied Physics **26**, L1487 (1987)
35. Martin, J.A., L. Vazquez, P. Bernard, F. Comin, and S. Ferrer, Appl. Phys. Lett. **57**, 1742 (1990)
36. R. Fedosejevs, Presentation at the Annual Conference of the Canadian Association of Physicists, Calgary, June 8-11, 1997
37. Y.Y. Tsui, private communication
38. Homepage of Grafoil Products is available at http://www.ucar.com/ucarcarb/Grafoil/Grafoil.htm
39. I.I. Aksenov, V.A. Belous, V.G. Padalka and V.M. Khoroshikh, Sov. J. Plasma Phys **4**, 428 (1978)
40. I.I. Aksenov, V.A. Belous, V.G. Padalka , R.E. Strelnitskii and V.M. Khoroshikh, Sov. Phys. Tech. Phys **25**, 1164 (1980)
41. D.R. McKenzie et al, Diamond and Related Materials **1**, 51-59 (1991)
42. J. Robertson, Properties of diamond-like carbon, Surface and Coating Technology **50**, 185-203 (1992)
43. R.F. Egerton, Electron Energy-Loss Spectroscopy in the Electron Microscope, Second edition, Plenum Press, 1996, p.384
44. Paul Joseph Fallon, Microscopy and Spectroscopy of CVD Diamond, Diamond-like Carbon and Similar Materials, 1992 PhD Thesis at the University of Cambridge
45. B.A. Banks and S.K.Rutledge, J. Vac.Sci.Technol. **21**,807(1982)
46. A.Antilla, J.Koskinen, M.Bister, and J.Hirvonen, Thin Solid Films **136**, 129(1986)